Navatek, Ltd.

841 Bishop St., Suite 1110
Honolulu, Hawaii 96813

Test-bed and Full-Scale Demonstration of Plasma Flow Control for Wind Turbines
Phase I Final Report

By
Neal E. Fine, Ph.D.
Christopher Szlatenyi
Benjamin Rosenthal

Prepared for:
Office of Naval Research

REPORT DOCUMENTATION PAGE				*Form Approved* *OMB No. 0704-0188*
Public reporting burden for this collection of information is estimated to average 1 hour per response, including the time for reviewing instructions, searching existing data sources, gathering and maintaining the data needed, and completing and reviewing this collection of information. Send comments regarding this burden estimate or any other aspect of this collection of information, including suggestions for reducing this burden to Department of Defense, Washington Headquarters Services, Directorate for Information Operations and Reports (0704-0188), 1215 Jefferson Davis Highway, Suite 1204, Arlington, VA 22202-4302. Respondents should be aware that notwithstanding any other provision of law, no person shall be subject to any penalty for failing to comply with a collection of information if it does not display a currently valid OMB control number. **PLEASE DO NOT RETURN YOUR FORM TO THE ABOVE ADDRESS.**				

1. REPORT DATE *(DD-MM-YYYY)* 15-07-2013	2. REPORT TYPE Final		3. DATES COVERED *(From - To)* 07 Feb 2012 – 31 May 2013
4. TITLE AND SUBTITLE Test-bed and Full-Scale Demonstration of Plasma Flow Control for Wind Turbines Phase 1 Final Report			**5a. CONTRACT NUMBER** N00014-12-C-0199
			5b. GRANT NUMBER
			5c. PROGRAM ELEMENT NUMBER
6. AUTHOR(S) Neal E. Fine, Ph.D. Christopher Szlatenyi Benjamin Rosenthal			**5d. PROJECT NUMBER**
			5e. TASK NUMBER
			5f. WORK UNIT NUMBER
7. PERFORMING ORGANIZATION NAME(S) AND ADDRESS(ES) Navatek, Ltd. 841 Bishop St., Suite 1110 Honolulu, HI 96813			**8. PERFORMING ORGANIZATION REPORT NUMBER** ISRN NAVATEK TR--2013/2
9. SPONSORING / MONITORING AGENCY NAME(S) AND ADDRESS(ES) Office of Naval Research (ONR 331) One Liberty Center 875 N. Randolph Street Arlington, VA 22203-1995			**10. SPONSOR/MONITOR'S ACRONYM(S)** ONR 331
			11. SPONSOR/MONITOR'S REPORT NUMBER(S)

12. DISTRIBUTION / AVAILABILITY STATEMENT
DISTRIBUTION STATEMENT A – Unlimited Distribution.

13. SUPPLEMENTARY NOTES
CDRL Data Item A002 Submittal No. 2. This submittal contains a number of corrections and revisions to improve clarity and is intended to replace Submittal No. 1 in its entirety.

14. ABSTRACT

This project concerns the development of a plasma flow control system for wind turbines. This document describes the technical progress made towards this goal during the 12-month Phase I effort that began in February, 2012. The Phase I project had four distinct objectives: (1) preliminary design of a plasma flow control system with manual control for wind turbines, (2) design and construction of laboratory facilities to permit component test and evaluation, (3) development and validation of simulation tools, and (4) field demonstration of a prototype system. Significant progress was made towards each of these goals, culminating in the field demonstration of a manually-controlled plasma flow control system on a 20 kW test turbine.

15. SUBJECT TERMS
Wind energy, active flow control, plasma actuation

16. SECURITY CLASSIFICATION OF:			17. LIMITATION OF ABSTRACT	18. NUMBER OF PAGES	19a. NAME OF RESPONSIBLE PERSON Neal E. Fine, Ph.D.
a. REPORT U	**b. ABSTRACT** U	**c. THIS PAGE** U	UU	118	**19b. TELEPHONE NUMBER** *(include area code)* (401) 595-7379

Standard Form 298 (Rev. 8-98)
Prescribed by ANSI Std. Z39.18

Plasma Flow Control for Wind Turbines – Final Report   Navatek, Ltd.

NAVATEK TR--2013/2

This page intentionally left blank.

Figures

Plasma Flow Control for Wind Turbines – Final Report   Navatek, Ltd.

NAVATEK TR--2013/2

Tables

Plasma Flow Control for Wind Turbines – Final Report   Navatek, Ltd.

NAVATEK TR--2013/2

This page intentionally left blank.

1. Executive Summary

The goal of this three-phase program is to develop and test a plasma flow control system for wind turbines. The system will use flush-mounted plasma actuators on the blades of wind turbines to control the boundary layer behavior in order to achieve higher power coefficients and to mitigate unsteady loads. In general terms, the three consecutive phases of the development program represent increasing complexity of the control system. In Phase I, the system was to be implemented and tested with manual on-off control. The second phase of the program will then introduce a feedback control system, to take some of the load off the pitch control system to maintain steady rotational speed while optimizing performance. In the third phase, we intend to introduce feed-forward control, where a forward-looking wind sensor will enable the flow control system to better react to incoming gusts.

This document describes the technical progress made towards this goal during the twelve month Phase I effort that began in February, 2012. The Phase I project had four distinct objectives: (1) preliminary design of a plasma flow control system with manual control for wind turbines, (2) design and construction of laboratory facilities to permit component test and evaluation, (3) development and validation of simulation tools, and (4) field demonstration of a prototype system. Questions that we attempted to address in the process included the following:

1. What wind turbines are available for a field demonstration?

2. How much of an increase in power coefficient can we expect to gain from a manually-controlled plasma flow control system on our chosen test turbines?

3. What actuator geometry and materials should we use for the field demonstration?

4. What power supply and power distribution components are required for the field demonstration?

5. What are the gaseous by-products of plasma actuators, and how will the source levels scale with wind turbine size?

6. How can a plasma flow control system be used to reduce the cost of wind energy, and what are the likely limits on the cost reduction?

To answer these questions, we performed six discrete tasks: 1) wind turbine test bed selection and baseline performance predictions, 2) laboratory facilities development and testing, 3) simulation tool development and testing, 4) environmental testing, 5) field demonstration, and 6) cost of energy analysis.

Key accomplishments of the Phase I program included the following:

1. A Renewegy VP20 20-kW wind turbine was selected as our test-bed for the field demonstration. Two identical turbines were purchased under a separate grant funding and were mounted on the wing walls of a dry dock in Navatek's Honolulu shipyard.

2. A low-velocity, open-circuit wind tunnel was designed and built for component development and testing.

3. A series of laboratory experiments was performed to measure the forces generated by plasma actuators for a variety of dielectric materials.

4. Wind tunnel testing showed that a thin surface-mounted actuator consisting of a 20-mil thick sheet of Cirlex could increase the lift coefficient by 10-13% over a range of angles of attack between the zero-lift angle and stall. In contrast, an embedded actuator consisting of a 180-mil thick Macor® dielectric was shown to increase the lift coefficient by up to 37% over a range of angles of attack between the zero-lift angle and stall.

5. A numerical simulation approach was developed to model plasma flow control on 2D wing sections. The approach uses a Reynolds Averaged Navier-Stokes solution with an imposed body-force to represent the actuator. The body force can be determined numerically, through an electrostatic model, empirically through laboratory measurements, or semi-empirically (e.g., computing the force distribution through the electrostatic model, but renormalizing the force to match the measured net force).

6. A separate set of experiments was performed to quantify the rate at which ozone and NO_x gases are produced by a typical plasma actuator. The measurements were then used to determine conservative estimates of the concentration of ozone and NOx downstream of a wind turbine. These conservative estimates support the conclusion that the concentrations can be expected to be below natural background concentrations of these gases. The measurements also showed a marked reduction in ozone production when an in-plasma catalyst was applied on the surface of the dielectric, a potentially important result that might be used to support a hypothesis regarding certain synergistic plasma-catalytic effects.

7. A plasma flow-control system without feedback control was implemented and tested on one of the two Renewegy wind turbines purchased under the MARAD grant. Thin surface-mounted actuators were used for the study. The power generated by the turbine was measured to increase by 5-13% with the plasma on, compared to the power generated by the same turbine with the plasma off. Since the plasma system was implemented in this phase without feedback control, and not optimized to minimize power consumption, only the gross increase in power generated was quantified.

2. Introduction

2.1 Background

Motivation: Reducing the Cost of Wind Energy

In 2010, the Chief of Naval Operations established a new Energy Vision for the U.S. Navy, as described in the publication "A Navy Energy Vision for the 21st Century." The introduction to the report provided a succinct motivation:

> Every day, the Navy consumes approximately 80,000 barrels of oil afloat and 20,000 megawatt hours of electricity ashore. These rates of consumption represent strategic and operational vulnerabilities. The Navy has a long history of leading energy transformations—from sail to coal to oil to nuclear power. Today, through a long-term vision for energy security, the Navy will once again transform energy vulnerabilities into mission advantages.

The Navy's Energy Vision addresses this vulnerability with a multi-pronged approach, including an aggressive and rapid transition to alternative energy sources for shore-based activities. Specifically, the Navy projects that half of its energy consumption ashore will come from alternative sources by the year 2020. By that year, half of the Navy's shore-based operations will be "net-zero energy consumers, using solar, wind, ocean, and geothermal power generated on base."

While the Navy has an undeniable history of leadership in promoting and adopting new energy technologies, as outlined in the 2010 Energy Vision report, it's clear that meeting these aggressive energy goals will be extremely challenging. For example, to meet 50% shore-based energy demand with alternative energy, commercial suppliers must be available. Since new Federal energy policies are unlikely to be put in place solely to ensure the viability of wind and solar energy providers, those providers must succeed in the marketplace largely on the basis of price. For that reason, it is important to look at the cost of alternative energy in comparison to the cost of conventional energy sources, and to invest in technologies that will help to ensure that alternative sources are competitive.

To examine the cost of different forms of energy, analysts use a metric known as the "levelized cost of energy" or LCOE. The LCOE represents the per-kilowatt-hour cost of building and operating a generating plant over an assumed time period. The individual cost components include initial capital costs, fuel costs, fixed and variable operations and maintenance (O&M) costs, financing costs, and utilization rate for each plant type. For alternative energy sources, such as wind and solar, the fuel is free and the levelized cost is heavily influenced by the initial capital costs.

Figure 1 shows a comparison of LCOE for a broad range of energy sources, including alternative sources such as wind, solar, geothermal and hydro power. The data, which was published in the Energy Information Administration's 2012 Annual Energy Outlook, represents levelized costs projected to 2017 in 2010 dollars. Reflected in this data is the projected drop in the cost of energy from natural gas-fired turbines due at least in part to the increased production from shale

Plasma Flow Control for Wind Turbines – Final Report   Navatek, Ltd.

NAVATEK TR--2013/2

reserves in the United States. Even with the non-mandated addition of carbon capture sequestration (CCS) technology, which increases the LCOE for natural gas plants by roughly 40%, the cost is still marginally lower than that of on-shore wind energy and significantly lower than wind energy produced by off-shore wind farms.
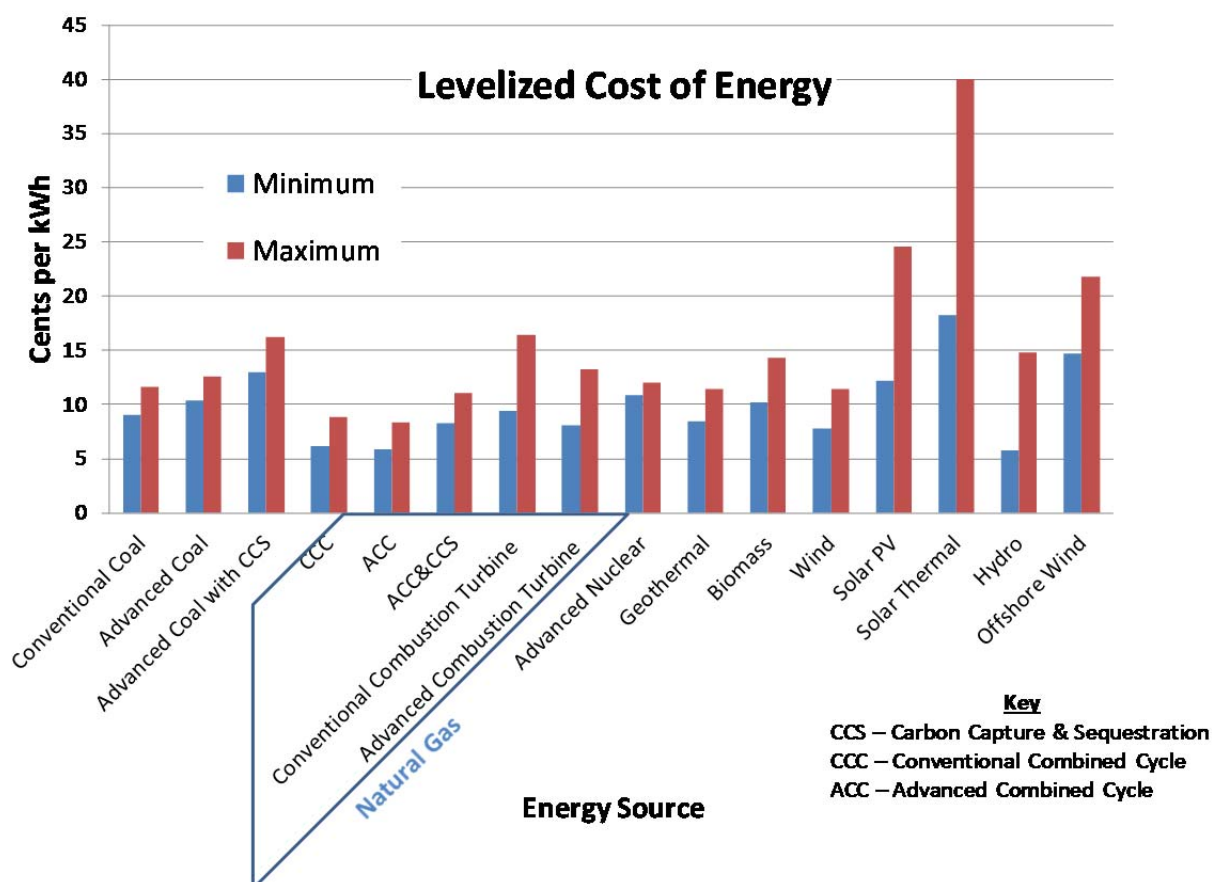
Figure 1. Levelized Cost of Energy (LCOE) for a variety of plant types.

In discussing the viability of wind energy in particular, it's worth noting that, in the U.S., there are often impediments to locating on-shore wind farms in regions of high demand, and there's a growing consensus that further meaningful penetration of wind energy in the U.S. market awaits the development of off-shore wind. Clearly, with the LCOE for off-shore wind estimated (based on European data) to be more than 50% greater than that for natural gas with CCS, a significant reduction in the cost of wind-generated energy is a strong requirement for growth in the industry. And without growth in the domestic wind energy industry, it will be difficult for the Navy to meet its Energy Vision goals.

At Navatek, we are focused on developing a technology that we believe will help to reduce the cost of wind energy. The underlying assumption is that many of the challenges associated with reducing the LCOE for wind can be addressed by implementing active control of the blade aerodynamics. Active flow control on the blades could enable lighter, more flexible blade design and could provide new opportunities for advanced rotor configurations such as two-bladed

downwind rotors. The ability to build lighter, more flexible blades could lead to lower capital costs and increased feasible diameters which in turn lead to increased energy output per dollar spent on capital and maintenance costs.

Active Flow Control

Aeroelastic instabilities that lead to structural fatigue are driven by unsteady aerodynamic loads on the rotor in response to changes in the incident flow due to gusts, free-stream turbulence, induced flow due to the tower, and upstream wakes from other turbines. Turbine manufacturers must settle for designs that are robust over a range of operating conditions, often sacrificing aerodynamic performance or overdesigning the structure to withstand extreme gusts and fatigue loads. As manufacturers have pushed their industrial-scale turbine designs to greater and greater rotor diameters and hub heights in an effort to generate more power per turbine, the industry has come ever closer to the point of diminishing returns—the point at which an increase in power generated is offset by the additional capital costs demanded by the structural requirements.

There is a growing consensus in the industry that the point of diminishing returns can be extended further through so-called "smart-blade" technology. A smart blade uses a combination of sensing and actuation to actively control the boundary layer on the surface of a rotor blade. In fact, active flow control has been shown over the past twenty years to be a powerful tool to suppress boundary layer separation in a wide variety of applications, including airfoils, bluff-body flows, and wide-angle diffusers (such as jet engine intakes). Controlled flow on wings, for example, exhibits dramatically improved aerodynamic performance through increased lift and reduced drag.

Various actuators have been proposed for active flow control on wind turbine rotor blades. Steady actuation by means of blowing and suction is effective, but would require extensive ductwork beneath the blade skin as well as a steady supply of high-pressure (or vacuum)—something that is both difficult to reliably manufacture and energetically costly to operate. Oscillatory actuators using so-called "synthetic jets" or "zero-net-mass-flux actuators" were developed in the mid-1980s, and have been demonstrated to be effective in aerodynamic applications, including wind turbines. However, these devices are mechanical and subject to structural or mechanical failure through fatigue, particularly in the harsh environments often experienced by rotating blades on a wind turbine.

Plasma Actuators

Plasma actuators hold significant promise for a robust, efficient, and effective means of blade control. Plasma actuators consist of an asymmetric arrangement of two electrodes separated by dielectric material (see Figure 2). The electrodes are powered by a high voltage source (~5-15 kV) with high-frequency, generally sinusoidal, alternating current (~1-3 kHz). The plasma that forms on the surface of the dielectric results in a volumetric force that controls the flow in the boundary layer. The force results from collisions between the energetic ions and the neutral air molecules. A detailed description can be found in the literature, most notably in (Enloe C. , et al., 2004), (Enloe C. L., et al., 2004), and (Corke, Enloe, & Wilkinson, 2010).
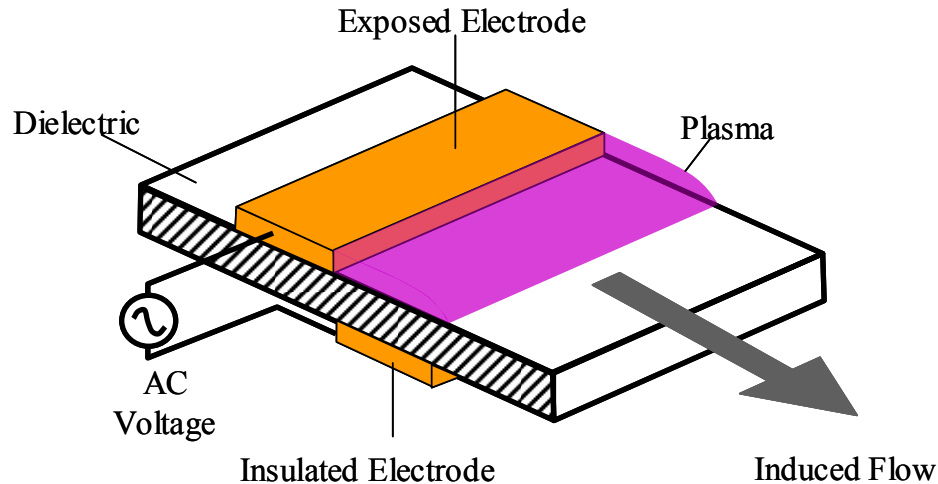
Figure 2. Schematic of a plasma actuator. *The plasma actuator induces a wall jet and a suction force that draws air in from beyond the boundary layer.*

Plasma actuators have a number of distinct advantages over other active flow-control devices. Since the actuators are fully electronic with no moving parts, they can be used in place of mechanical flaps to control the lift-curve slope of the blade section by modifying the trailing edge flow. Further, since the actuators are low-mass and low-volume, they add very little weight to the blades and can withstand high centrifugal loading. Also, because of their low form-factor, they can be mounted flush with the blade surface, resulting in virtually no parasitic drag. Unlike other flow-control devices, no complex slots, cavities, or internal structures in the blades are required. Plasma actuators have high bandwidth and no observed hysteresis, making them extremely favorable for use in closed-loop control algorithms. Because they create a pressure gradient that draws fluid into the boundary layer that forms a wall jet, they are very effective at maintaining attached flow in an otherwise adverse pressure gradient. Finally, plasma actuators consume little power, requiring as few as 10 W per meter in unsteady (e.g., pulsed) mode.

2.2   Project Goals

There were four principal goals of this project: (1) preliminary design of a plasma flow control system for wind turbines, (2) design and construction of laboratory facilities to permit component test and evaluation, (3) development and validation of simulation tools, and (4) field demonstration of a prototype system. These four objectives are described in detail below.

Design of a Plasma Flow Control System for Wind Turbines

The first objective was to design a plasma flow control system for wind turbines. Many questions had to be answered in order to complete the design process. What metric (or metrics) should be used to design the plasma actuators? What type of material should be used for the dielectric layer, and of what thickness? What operating voltage and frequency would be appropriate for the application? Where should the actuators be placed on the surface and how should they be attached? What power supply should be used, and how could the power be delivered to the rotating blades? Some information was available from previous research, particularly regarding the relative thrust generated by different materials and different

thicknesses, but very little data was available that would allow us to design a plasma flow control system for a particular wind turbine. A combination of scale-model testing and simulation would be required to complete the system design.

Design and Construction of Laboratory Facilities

The second objective was to develop laboratory facilities to build and test components and to validate simulation tools. The facilities include a low-speed wind tunnel, a system for fabricating wings, a workstation for building and testing actuators, and an apparatus for performing various environmental tests. With regards to the wind tunnel, the intent was to design and build a low-cost, medium-fidelity tunnel for testing model scale wing sections. The tunnel was to be housed in a warehouse in North Kingstown, RI, with open floor space of roughly 35 ft by 55 ft and 25 ft ceiling height. To augment this facility, and to move ahead with the research while our wind tunnel was under construction, we subcontracted to Professor Kenny Breuer and his group at Brown University. The Breuer Lab includes a low-speed wind tunnel similar to the Navatek design, but with higher fidelity and proven characteristics.

Regarding environmental testing, the original objective was to examine the behavior of plasma actuators in a variety of environmental conditions (mainly temperature and humidity). Of particular interest was (and is) the response of the actuators to rain and ice. For reasons that are described in Section 8, the objective of the environmental testing was shifted to measurement of the gaseous by-products of plasma actuators.

Development of Simulation Tools

The third objective was to begin the development and compilation of a set of numerical tools useful for predicting the performance of wind turbines with plasma flow control. The central pillar of the toolset is a Reynolds Averaged Navier-Stokes (RANS) CFD solver, called FINE™, marketed by Numeca, which uses the ISIS RANS solver. The first goal was to work with Numeca to create a User Defined Function tool that would allow us to enforce a body force on the fluid to simulate the effect of a plasma actuator. A related goal was then to develop a model of the actuator that would allow us to compute the force generated by a particular actuator design. The combination of those two tools would then allow us to compute the sectional lift and drag on a wing section as a function of angle of attack, with and without plasma flow control. The resulting forces could then be used in a blade-element model of a wind turbine.

Field Demonstration

The fourth objective of the project was to perform a field demonstration of a plasma flow control system on an operating wind turbine. A key task at the start of the project was to identify a turbine on which we could install our system and perform some limited demonstrations. Fortunately, around the time we started this project, we won a grant from the Department of Transportation's Maritime Administration (MARAD) to support the purchase and installation of a pair of Renewegy VP20 20 kW wind turbines at our shipyard in Honolulu. This provided the ideal test bed for the plasma flow control technology.

Plasma Flow Control for Wind Turbines – Final Report   Navatek, Ltd.

NAVATEK TR--2013/2

2.3   Accomplishments

Key accomplishments are highlighted below, and described in detail in the remainder of this document.

- A separate MARAD grant allowed us to purchase two Renewegy VP20 20-kW wind turbines. The twin turbines were mounted on the wing walls of a dry dock in Navatek's shipyard at Pier 41 in Honolulu, HI. This provides an ideal test-bed for our plasma flow control technology.

- A low-velocity wind tunnel was designed and built for component development and testing.

- A series of laboratory experiments was performed to measure the forces generated by plasma actuators for a variety of dielectric materials.

- The Navatek wind tunnel was used to measure the lift generated by a wing section that matches the section of the Renewegy VP20 turbine at the seven-tenths radius position. The thin "paste-on" actuators were shown to increase the lift coefficient by 10-13% of a range of angles of attack between the zero-lift angle and stall.

- The low-velocity wind tunnel at Brown University was used to test plasma actuation on an identical wing section constructed with an actuator embedded in the section and made with a thick dielectric. This actuator, which has greater control authority then the thin "paste-on" actuators, was used to increase the lift coefficient by up to 37% over a range of angles of attack between the zero-lift angle and stall.

- A numerical simulation approach was developed to model plasma flow control on 2D wing sections. The approach uses a Reynolds Averaged Navier-Stokes solution with an imposed body-force to represent the actuator. The body force can be determined numerically, through an electrostatic model, empirically through laboratory measurements, or semi-empirically (e.g., computing the force distribution through the electrostatic model, but normalizing the force to match the measured net force).

- A separate set of experiments was performed to quantify the rate at which ozone and NO_x gases are produced by a typical plasma actuator. The measurements were then used to determine conservative estimates of the concentration of ozone and NOx downstream of a wind turbine.   These conservative estimates support the conclusion that the concentrations can be expected to be below natural background concentrations of these gases.

- The ozone measurements showed a marked decrease in ozone production when a heterogenous in-plasma catalyst was applied to the actuator. While this result is of interest for the reduction in the toxic byproduct gas, it also supports a conjectured mechanism for the increased thrust found when the catalyst is applied. Namely, it has been hypothesized that the increase thrust is due to an increase in the rate at which certain oxygen ions are created in the plasma, resulting from the chemistry promoted by the

catalytic layer. Since the increased number of oxygen ions can be expected to come at the expense of ozone production, the lower rate at which ozone was measured when the catalyst was used can be seen as support for this hypothesis.

- A plasma flow-control system without feedback control was implemented and tested on one of the two Renewegy wind turbines purchased under the MARAD grant. Thin "paste-on" actuators were used for the study. The power generated by the turbine was measured to increase by 5-13% with the plasma on, compared to the power generated by the same turbine with the plasma off. To make the comparison, the plasma actuators were turned on and off for 10-minute cycles and the average power recorded by the two datasets were compared as a function of wind speed. Since the plasma system was implemented in this phase without feedback control, and not optimized to minimize power consumption, only the gross increase in power generated was measured.

Plasma Flow Control for Wind Turbines – Final Report   Navatek, Ltd.

NAVATEK TR--2013/2

3.   Facilities

3.1   Navatek Wind Tunnel

Wind Tunnel Design and Construction

The Navatek wind tunnel is an open-circuit, closed section tunnel incorporating an upstream blower, followed by an exit diffuser, settling chamber, contraction, test section and exit diffuser. Elements of the design and construction are described in detail in Appendix A. Figure 3 shows a solid model of the design, and Table 1 below summarizes the main characteristics of the tunnel. Pictures of the tunnel after completion are shown in Figure 97 on page 109.
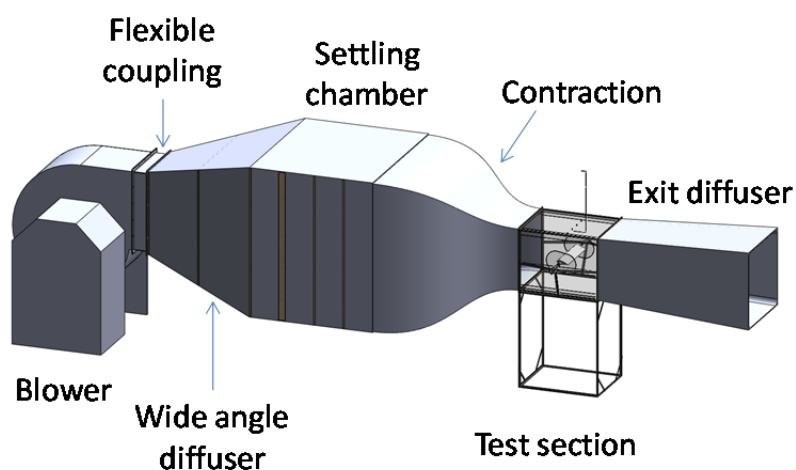
Figure 3. 3D CAD model of the Navatek wind tunnel. *The open-circuit wind tunnel is a low-cost, medium fidelity tunnel ideal for component development and testing.*

Table 1. Wind tunnel characteristics.

Characteristic	Description
Wind Tunnel Type	Open circuit, closed test section
Fan type	Centrifugal blower at inlet
Fan power	18.2 hp
Test Section Dimensions	3 ft x 3 ft cross section, 4 ft length
Test Section Max Speed	56 ft/s (17 m/s, 38 mph, 33 knots)
Contraction ratio	6:1
Flow control	4-in honeycomb, ½ in cells, 4 wire cloth screens
Instrumentation	2-axis load cells for lift and drag measurements, shaft rotary position sensor, Pitot tube

Velocity Profile

The velocity characteristics in the test section of the wind tunnel were measured using a Pitot tube – mounted on a CNC linear actuator – and a differential pressure transducer. The Pitot tube was inserted in five holes in the roof of the test section spaced equidistant along a line that spanned the width of the section at its midpoint. Velocity variations along the width of the tunnel were found to be small compared to vertical variations, so only the middle hole was used for subsequent tests.

Velocities were recorded at ~5 Hz data rate and averaged over ~30 s at 1 in intervals along the height of the test section at the wind tunnel's maximum speed. Velocity sweeps were measured with the overhead door open and closed. With the door open, the average tunnel speed increased by ~0.3 m/s (~2%) over the speed with the door closed. However, the open-door flow to be appeared more turbulent. The velocity variance increased ~40% in both space and time with the door open. For that reason, subsequent tests were performed with the door closed. Figure 4shows three trials of profiles with the door closed.
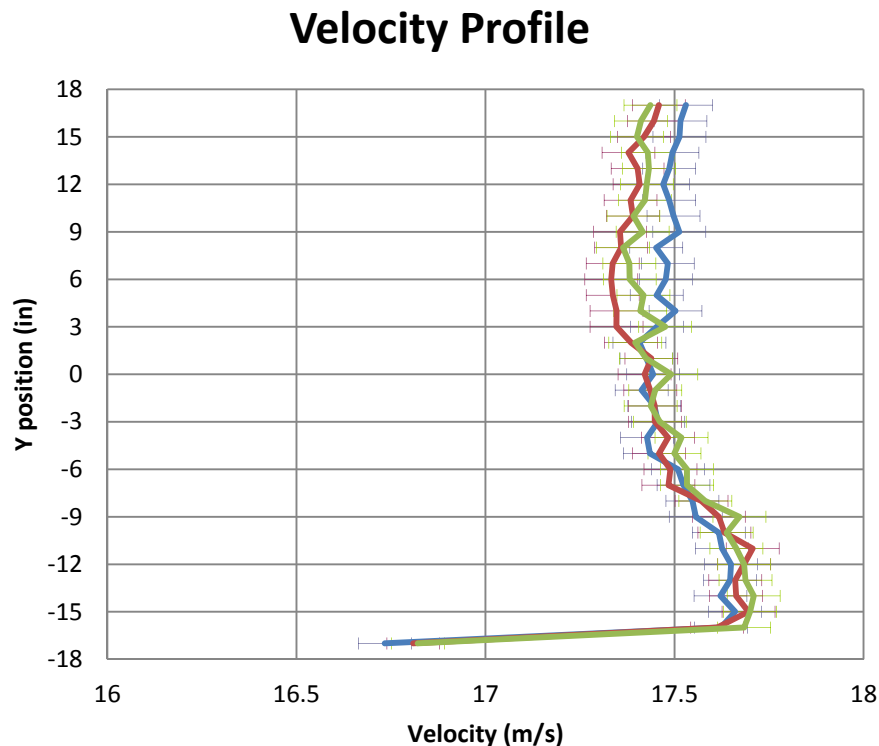
Velocity Profile

Figure 4. Vertical velocity profiles. *This plot shows velocity profiles measured at the horizontal center of the test section.*

In Figure 1, the top and bottom of the tunnel are located at ±18 in, respectively. The error bars account for the uncertainty associated with the pressure transducer, Pitot tube, and data acquisition system. With roughly 2% variation the mean velocity over the vertical span of the tunnel, the velocity profile is quite uniform. However, the boundary layer on the bottom is noticeably thicker than that on the top.

The boundary layers were further investigated using higher resolution measurements near the boundaries. The radius of the bend in the Pitot tube prohibited measurements within ¾ in of the ceiling. Below ¾ in, no boundary layer was detected. Results of this test and a combined profile including the boundary layer and the average previous profiles are shown in Figure 5. From this figure, it's clear that there is top-bottom asymmetry in the tunnel. That asymmetry is likely due to asymmetry in the tunnel inlet, also referred to as the blower outlet. The outlet of the blower includes a triangular plate (see Figure 92 in Appendix A) that covers part of the opening. The purpose of the plate, which was installed by the manufacturer, is to prevent backflow in that corner. Despite our concerns that it would lead to asymmetric flow in the tunnel, we decided to leave the plate attached.

It's also possible that asymmetries are associated with the internal structure of the tunnel. In particular, the screen frames in the settling chamber had a tendency to bow inwards when installed. In an attempt to eliminate the bowing, we used screws at two points on each side of the interior of the frames to draw the sides into their slots, so that the frame would be close to flush on the interior. We did this only for the two screens downstream of the honeycomb. It's possible that bowing in the screens upstream of the honeycomb could lead to some asymmetry in the test section velocity profiles.

Although the asymmetry is undesirable, it's sufficiently small to be ignored for now. We may return to this subject in the future, when we will consider removing or re-designing the "backflow" plate at the blower outlet, and we can consider other tunnel modifications.
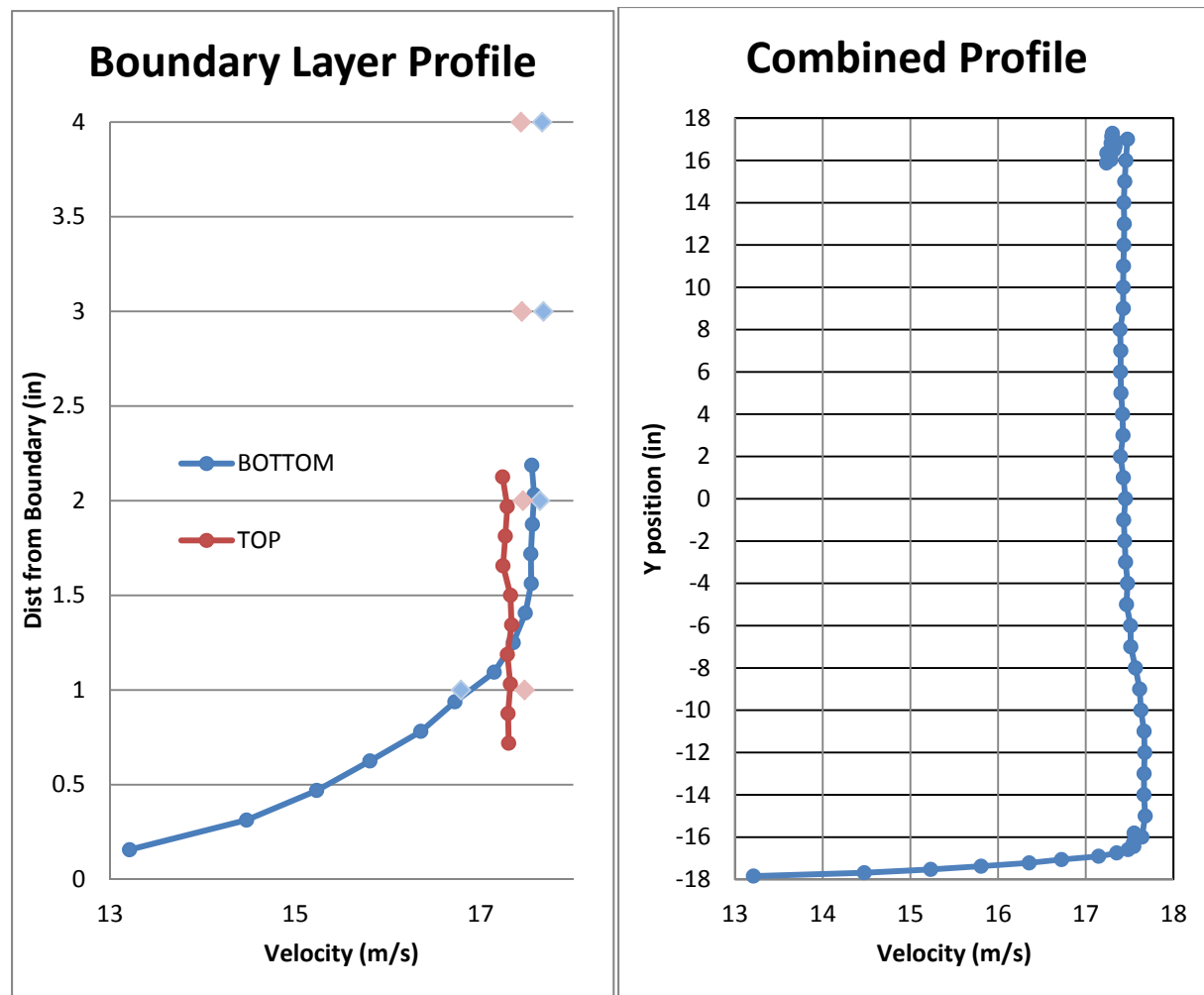
Figure 5. Boundary layer velocity profiles. *These velocity profiles show an top-bottom asymmetry in the tunnel velocity. However, they also show that the boundary layer displacement thicknesses are only about 2% of the tunnel height.*

Turbulence Intensity

An important characteristic of any wind tunnel is the turbulence intensity, usually measured with a hot-wire anemometer. The turbulence intensity of the Navatek wind tunnel will be measured during the planned Phase II program, which is slated to begin in June, 2013.

3.2   Brown University Wind Tunnel

The Brown University Wind tunnel is a closed-circuit, closed test section tunnel located in Brown University's School of Engineering in Providence, RI. The lab is run by Professor Kenny Breuer, an expert in Flow Physics, including active flow control. We issued a subcontract to Brown University to perform wind tunnel testing in support of the project. In particular, we wanted to take advantage of the Breuer Lab's experience with generating harmonically time varying inflow angles using an upstream flapping wing. Although we completed development of the apparatus for producing unsteady gusts, those experiments will be performed in a subsequent

Phase of the program. Experiments performed during this Phase of the program are described in Section 5.

Figure 6 shows the test wing mounted in the Brown University wind tunnel, along with close-ups of the mounting apparatus.
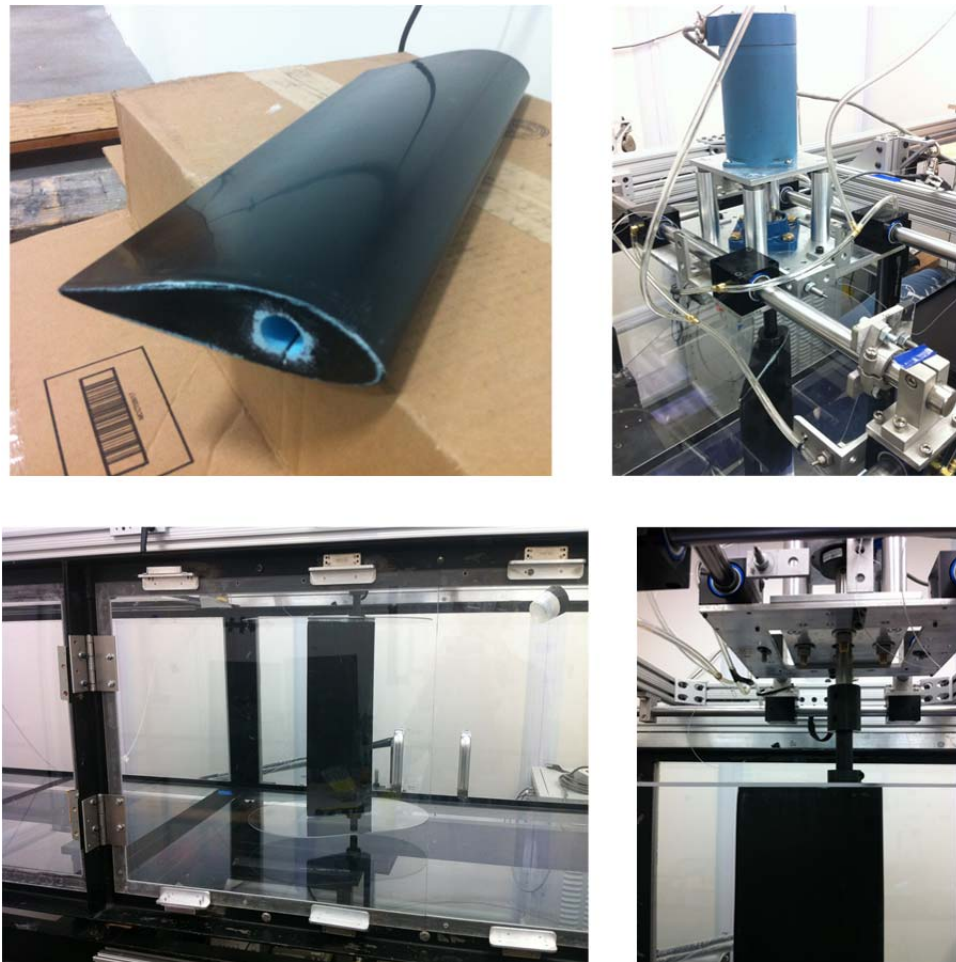
Figure 6. Brown University tunnel pictures. *These pictures show the test wing (upper left) and mounting apparatus in the Brown University wind tunnel.*

3.3   Plasma Power Supply and Thrust Measurements

Plasma actuators work by imparting a volumetric force on the air above the covered electrode. They can be constructed of a variety of dielectric materials and thicknesses, and differing designs can be compared by measuring the force that they generate. Since the actuators create a thin jet of air along the surface of the actuator, the force is often referred to as a thrust. To measure the thrust, the actuator can be placed on a scale so that the wall jet is directed vertically up (or down). The thrust then can be measured as an increase (or decrease) in the weight of the apparatus.

We constructed a thrust measurement system consisting of an OHAUS A812 precision scale capable of measuring forces up to 812 g with a precision of 0.01 g (see Figure 7). The metal

scale tray is grounded by a 36 AWG magnet wire. The scale was calibrated using a 500 g calibration weight. To show that the electric field generated by the plasma is not affecting the force measurements, we weighed a calibration weight with the plasma off and again with the plasma on. The weight changed by 0.01 g, which is the precision of the scale, indicating that the scale measurement is not corrupted by the strong electric field generated by the plasma actuator.
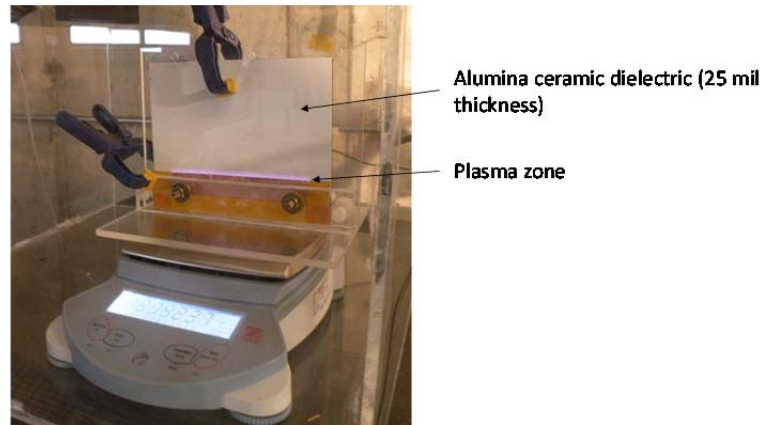
Figure 7. Actuator thrust measurement arrangement. *To measure the thrust generated by a plasma actuator, the actuator is held by a Plexiglas stand and placed on an OHAUS A812 digital scale.*

The power supply consists of a Titan MAC-02 mainframe amplifier with a Titan MOS-01 oscillator (Figure 8) coupled to a pair of high voltage transformers (Figure 9). With no load, the power supply delivers the a/c voltage shown in Figure 10.
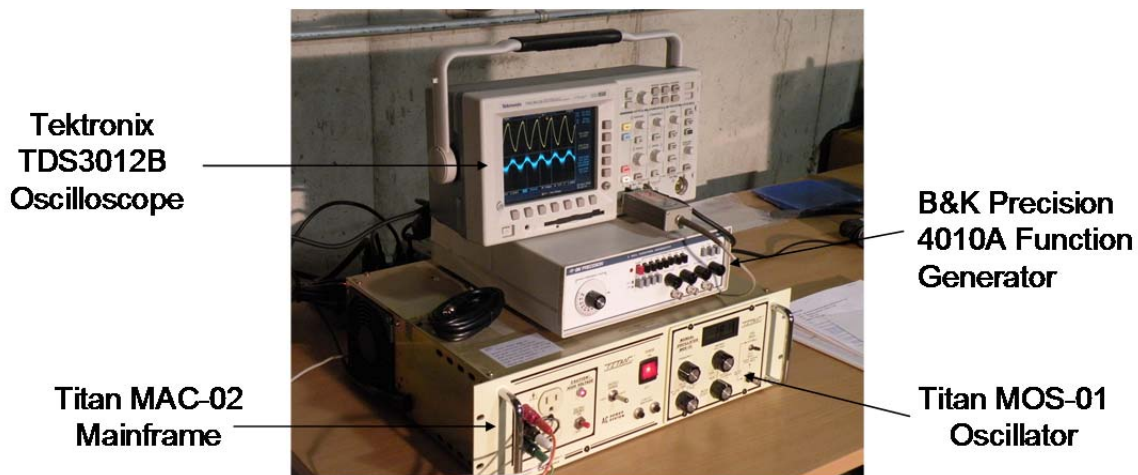
Figure 8. Mainframe power supply, function generator and oscilloscope. *This picture shows the power supply and measurement set up for testing plasma actuators.*

Plasma Flow Control for Wind Turbines – Final Report   Navatek, Ltd.

NAVATEK TR--2013/2
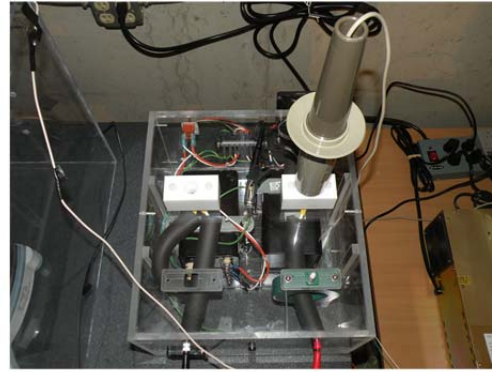
PTI High Voltage Transformer   Modified Power Supply Transformer Box

Figure 9. PTI transformers. *These pictures show PTI high voltage transformers used by the power supply to step up the voltage provided by the Titan mainframe.*
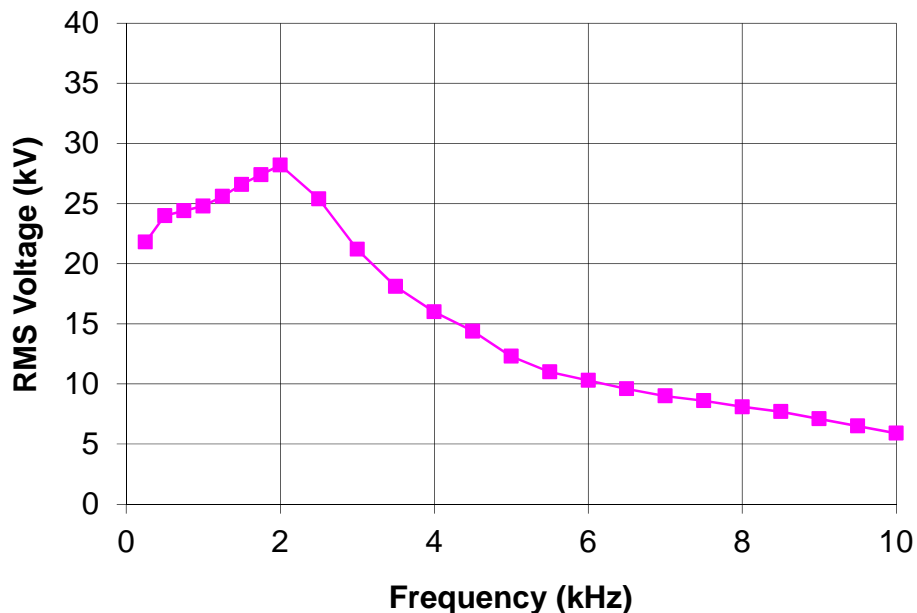
Figure 10. Power supply voltage output. *RMS voltage provided by the power supply, including the pair of step-up PTI transformers.*

Plasma Technics, Inc., (PTI) is a manufacturer of high quality, high voltage transformer products for a variety of applications such as ozone generation, NOx conversion, Excimer lamps, and others. In addition to the transformers shown in Figure 9, PTI makes a microcontroller that automatically finds the optimum system operating frequency. The DAT210 microcontroller, shown in Figure 11, is used to power the actuators mounted on the Renewegy turbine (see Section 9 for further description of the field test components).

Figure 11. PTI's DAT210 microcontroller. *The picture on the left is taken from PTI's website, and the picture on the right is the inverter installed and used in Navatek's laboratory.*

3.4   Test Wing Fabrication

Our airfoil models are foam-cored and shaped with a computer-controlled four-axis hot-wire foam cutter (Figure 12). The foam cutter is controlled by software on the PC. FoamWorks is a graphical software tool that can be used to generate the codes for a CNC controller. We use a software tool called Mach3 to control the four linear actuators. We use Dow StyroFoam™ intended for use as a buoyancy billet and purchased from a local marine supply store (Defender, Waterford, CT), which we cover with epoxy resin (e.g., West System 105 epoxy resin and 205 hardener). The wing sections can be cut with an indent sized to fit a plasma actuator.
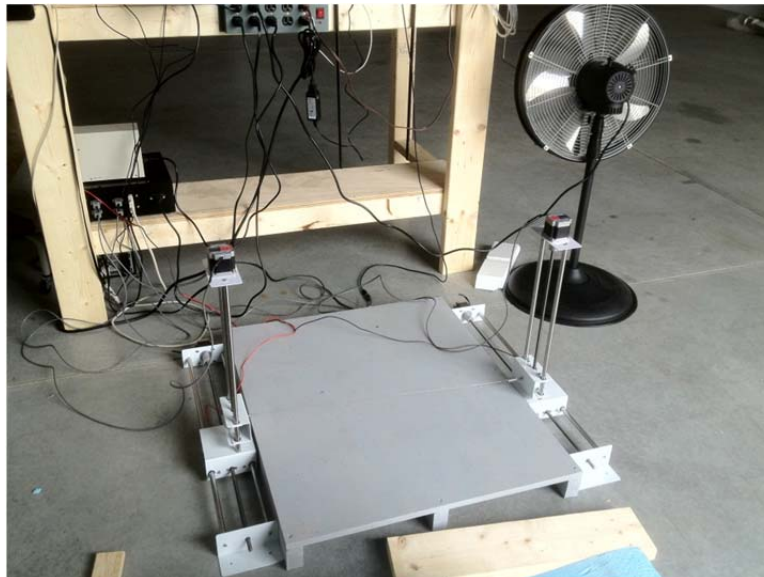
Figure 12. Hot wire foam cutter. *This picture shows the four-axis hot-wire foam cutter used to fabricate test wings.*

Plasma Flow Control for Wind Turbines – Final Report   Navatek, Ltd.

NAVATEK TR--2013/2
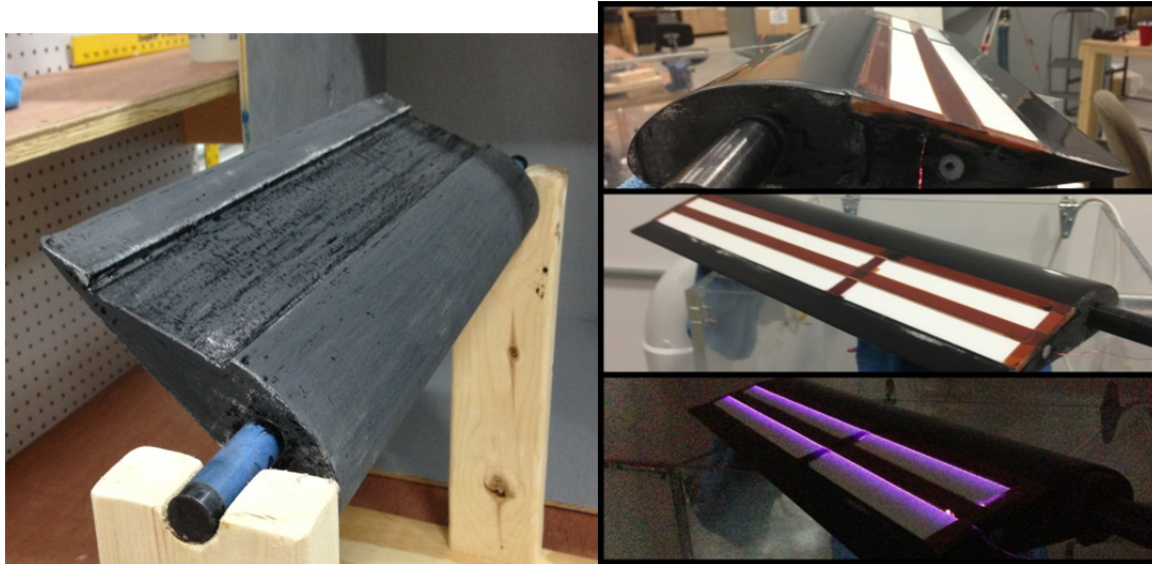
Figure 13. Sample wing with embedded actuator. *The wing's foam core was cut using the four-axis hot-wire foam cutter shown in Figure 12.*

3.5   Ozone and NO$_x$ Measurements

Our facilities include a system for measuring the gaseous byproducts of plasma actuators, including a pair of rented gas analyzers. A full description of the apparatus is provided in Section 8, beginning on page 64.

3.6   Twin 20kW Turbines

A pair of identical commercial scale wind turbines was purchased from Renewegy, Inc. and installed on the wing walls of the company's dry dock in Honolulu. The nameplate power rating of each turbine is 20 kW. The twin turbines, which were purchased with funding from a Department of Transportation MARAD grant, are shown in Figure 14.

Figure 14. Navatek's Twin turbine test-bed. *These two Renewegy 20 kW turbines are mounted on the wing walls of the Pier 41 Dry Dock in Honolulu. The one on the right is outfitted with our plasma flow control system.*

The cut-in speed of the VP20 is 3.5 m/s and the nameplate power rating of 20 kW is reached at the rated speed of 15.8 m/s. The rotor speed is 100 – 110 rpm. The diameter is 9.6 m. Power is optimized through a variable pitch control system. One of the big advantages of these turbines is that they have a hydraulic tip-down tower system that provides easy access to the nacelle for modification and maintenance. With the use of the hydraulic rise kit, the complete tower and turbine can pivot at its base to be raised and lowered in less than ten minutes. The turbines are positioned such that when tilted down, the nacelle is accessible from the opposite wing wall. Another advantage is the VP-20's advanced data logging capabilities. It is capable of capturing 15 channels of data at 10 Hz. It is equipped with an ultrasonic anemometer and 3-axis accelerometer, along with other sensors.

4.   Lift and Drag Measurements in the Navatek Wind Tunnel

This section describes the lift and drag measurements made using the Navatek wind tunnel and the test wings developed for this program. In it, we detail the setup and debugging of the lift and drag measurement system, the comparison between measured and computed lift for the VP20 test wing, and the evaluation of the effect of plasma actuation on the wing's lift characteristics. We conclude with an estimate of the effects of actuation on the performance of the VP20 wind turbine.

4.1   Setup

The wing is mounted horizontally in the test section, as shown in Figure 1. Lift and drag are measured by a pair of strain gauge load cells (Futek MBA400 Bi-Axial Load Arm: 50 lb capacity), one on each end of the wing. The wing is mounted at each end on two pins fixed to a plate which is welded to the end of the cylindrical shaft. Each shaft is connected to a u-joint by a threaded stud and a small coupling held in the u-joint bore hole with a set-screw[1]. The other end of the u-joint connects to another small coupling shaft which connects to the load cell. The apparatus is shown in Figure 1. Plexiglas endplates rest on the pins that support the wing and provide wall boundaries outside of the test-section boundary layers to minimize the effects of three-dimensional flow.

The two forces measured by the load cell are not necessarily aligned with the vertical and horizontal directions and, in fact, the orientation will change with every change in angle of attack because they are rigidly attached to the shaft. Further, no attempt is made to align the left and right strain gauge coordinate systems with each other. For that reason, we must perform coordinate transformations at each load cell to derive lift and drag forces from the four-axis load cell data.

4.2   Problems Identified during Initial Testing

Prior to performing any lift and drag measurements, we noticed two inconsistencies with the load cells. First, the factory-supplied calibration data did not yield the correct force when we used calibration weights to validate the load cells. In fact, the measured forces differed by as much as a factor of two. For that reason, we calibrated the load cells ourselves by hanging calibration weights from each shaft and used our calibration curve when making lift and drag measurements. After conferring with the manufacturer, we determined that the discrepancy between our measurements and the factory calibration was caused by a lateral offset in the forces that we were applying, resulting in a moment applied to the strain gauges. To compensate for this, we recalibrated the load cells using certified calibration weights mounted at the correct distance from the strain gauges. However, since we measured lift and drag using the faulty calibration, we will present the results as measured here prior to recalibration. This will provide a complete history of the development.

---

[1] Initially, the apparatus did not include u-joints. The need for u-joints is discussed in the next section.

The second issue we encountered was a variable static load which changed with angle of attack. In other words, when the wing was loaded with a 10-lb weight, and the strain gauge force was evaluated for several angles of attack, the vector sum of the two orthogonal forces was not constant, even after calibrating the cells to give us 10-lb (plus the weight of the wing) at zero angle of attack. When this test was run for each load cell independently (e.g., without the wing attached), the problem went away. We concluded that the problem was caused by a small misalignment of the shafts on either side of the wing, and we solved the problem by modifying the shafts to include universal joints on either side where the shafts connect to the load cells. The u-joints correct for any misalignment, and the measured force is now consistent. However, the u-joints resulted in a small amount of "slack" in the angle of attack. A new pair of u-joints, built to higher tolerance, was purchased to remove the slack. Again, since this fix came after our initial lift and drag measurements, the results in the section titled "Preliminary Measurements without Actuation" will include the negative effects of the u-joint slack. Subsequent measurements, beginning with those plotted in Figure 20, were made with the upgraded u-joints. We include the preliminary measurements to record a thorough history of the development.

4.3   Coordinate Transformation

Zero angle of attack is defined by aligning the leading and trailing edges of the wing with the aid of a laser level. The rotary sensor is zeroed at that angle. The gravitational load of the wing and the shaft is then used to determine the zero-angle-of-attack rotation between the strain gauge axes and the inertial frame of the wind tunnel (hereon referred to as the inertial frame). The angle, θ_0, is shown in Figure 15.
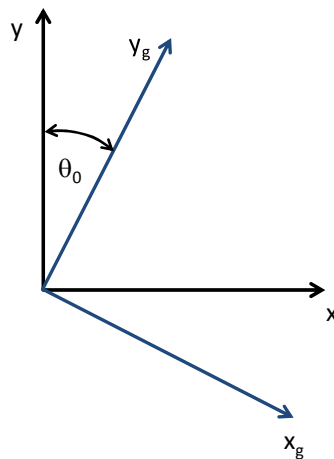
Figure 15. Tunnel coordinate system and definition of the angle θ_0. *The coordinate system (x_g, y_g), defined by the orthogonal strain gauge forces, is rotated an angle θ_0 with respect to the inertial frame. θ_0 must be determined for each of the two strain gauges each time the angle of attack is zeroed.*

The wing coordinate system (x_w, y_w) is rotated by the angle of attack, α, with respect to the inertial frame, as shown in Figure 16.
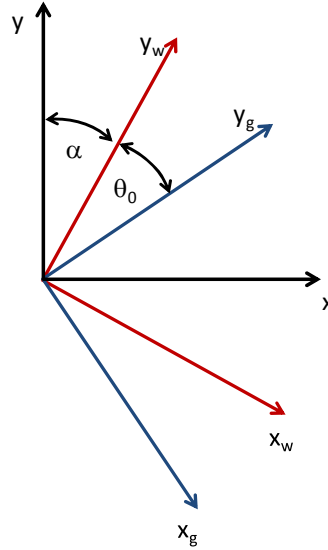
Figure 16. Inertial, wing and strain gauge coordinate systems. *The coordinate system (x_w, y_w) is rotated by the angle of attack, a, with respect to the inertial frame.*

If (F_{gx}, F_{gy}) are the two components of force measured in the (x_g, y_g) reference frame, then the lift, L, and drag, D, are determined as follows:

$$L = F_{gy} \cos(\theta_0 + \alpha) - F_{gx} \sin(\theta_0 + \alpha) \tag{4-1}$$

$$D = F_{gx} \cos(\theta_0 + \alpha) + F_{gy} \sin(\theta_0 + \alpha) \tag{4-2}$$

4.4   Preliminary Measurements without Actuation

Preliminary measurements of the lift of the VP20 wing are shown in Figure 17. The wing has a chord length of 0.175 m and span of 0.732m, for an aspect ratio of about 4.2. Acrylic endplates are used to minimize 3D effects. The endplates are approximately oval in shape with maximum height of 0.305 m and maximum length of 0.406 m. The figure shows an initial comparison to 2D CFD results using the previously validated FINE™ code. Since blockage effects for this geometry are minimal (as is evident by comparing the two CFD results, with and without the tunnel ceiling and floor), we are led to conclude that the difference in measured lift is due to other neglected physical effects. One possibility is that the endplates do not do enough to reduce 3D effects, including induced drag. To test that hypothesis, we ran our potential flow tool, Aegir, for two geometries – one a quasi-2D solution (e.g., a very high aspect ratio wing) and the other with the correct span and a representation of the side walls with the correct gap (but without modeling the endplates). The results show that the 3D lift slope comes closer to matching the measured lift slope than either 2D result, indicating that 3D effects may play a large role in the discrepancy between the measured and computed lift.

To test this hypothesis further, we measured the lift and drag in the tunnel without the end plates. We then compared the measured lift to the computed 2D lift, using a finite aspect ratio correction to the computed 2D lift:

$$\frac{\partial C_{L_{3D}}}{\partial \alpha} = \frac{\partial C_{L_{2D}}}{\partial \alpha} \frac{1}{1 + 2/A} \qquad (4\text{-}3)$$

where A is the aspect ratio of the wing (the ratio of span to chord, equal to 4.19 for our test wing). We then numerically integrated this expression using two-point backwards finite difference representation of the lift-slopes Figure 18 shows the resulting comparison. While the comparison is favorable for positive angles of attack, the curves diverge for negative angles of attack.

In addition to this discrepancy, still to be explained are differences in the zero-lift angle of attack (-4 deg measured, -3 deg computed) and the stall angles (-9.5 and 4.5 deg measured, -11 and 7 deg computed). We note that the "slack" in the u-joints, present at the time of these measurements, could account for some of these differences. Calibration issues, addressed in the next section, offered another possible explanation. The differing stall angles could also be explained in part by 3D effects in the tunnel (that is, non-negligible vertical or crossflow in the tunnel test section), tunnel turbulence intensity and length scales, and differences in computed and actual turbulent transition on the wing.

The measured and computed drag forces are shown in Figure 19. The measured drag includes parasitic drag due to flow over the shaft and endplates. The parasitic drag was not quantified.
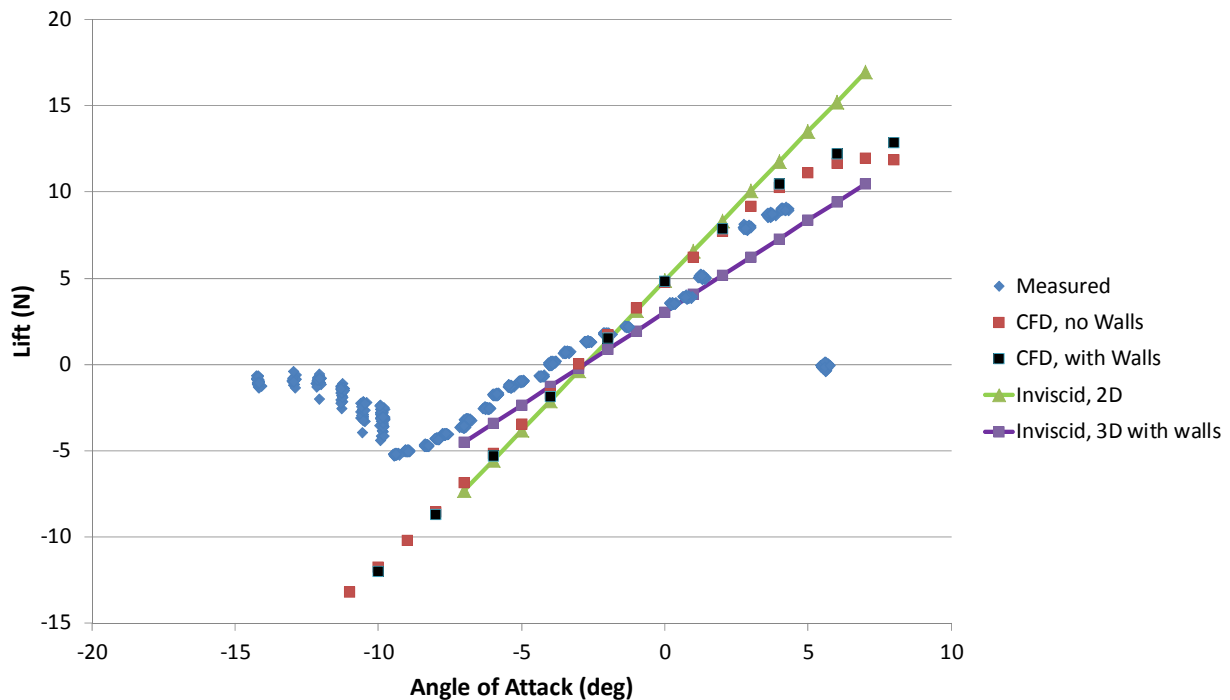
Figure 17. Initial measured and computed lift forces. *The lift vs angle of attack is plotted for the VP20 wing section, with comparison to computations.*
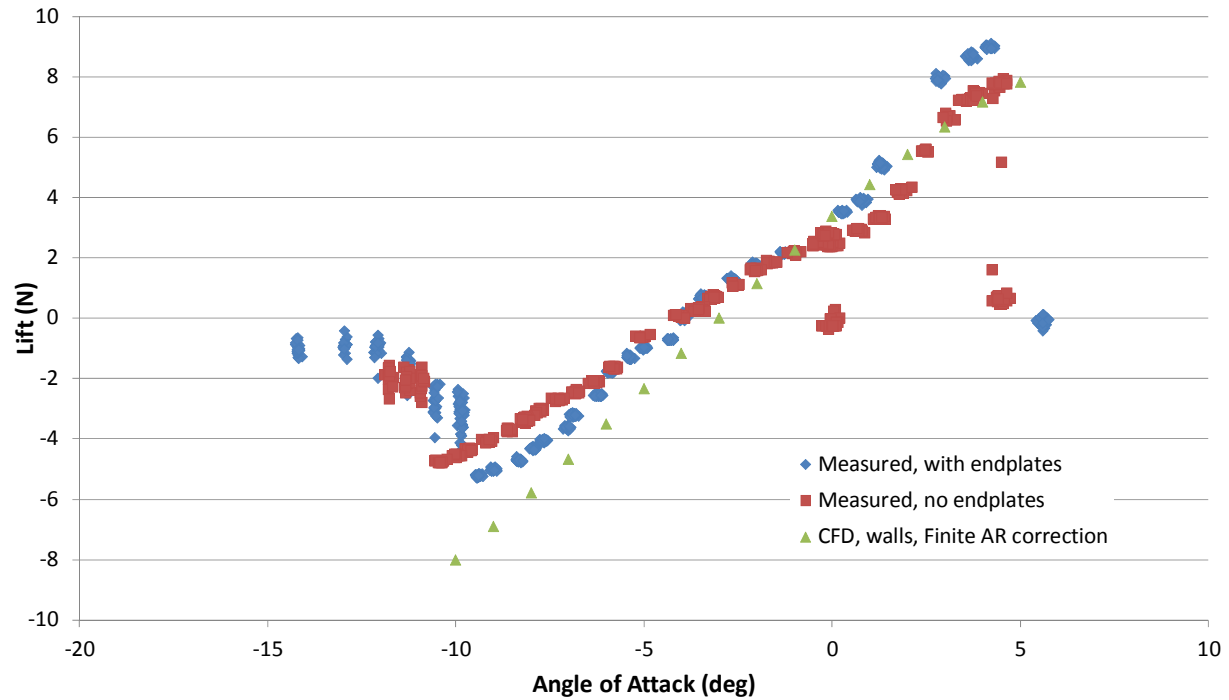
Figure 18. Measured and computed lift forces, with corrections. *The lift vs angle of attack is plotted for the VP20 wing section, with and without end plates and compared to 2D CFD with a finite aspect ratio correction.*
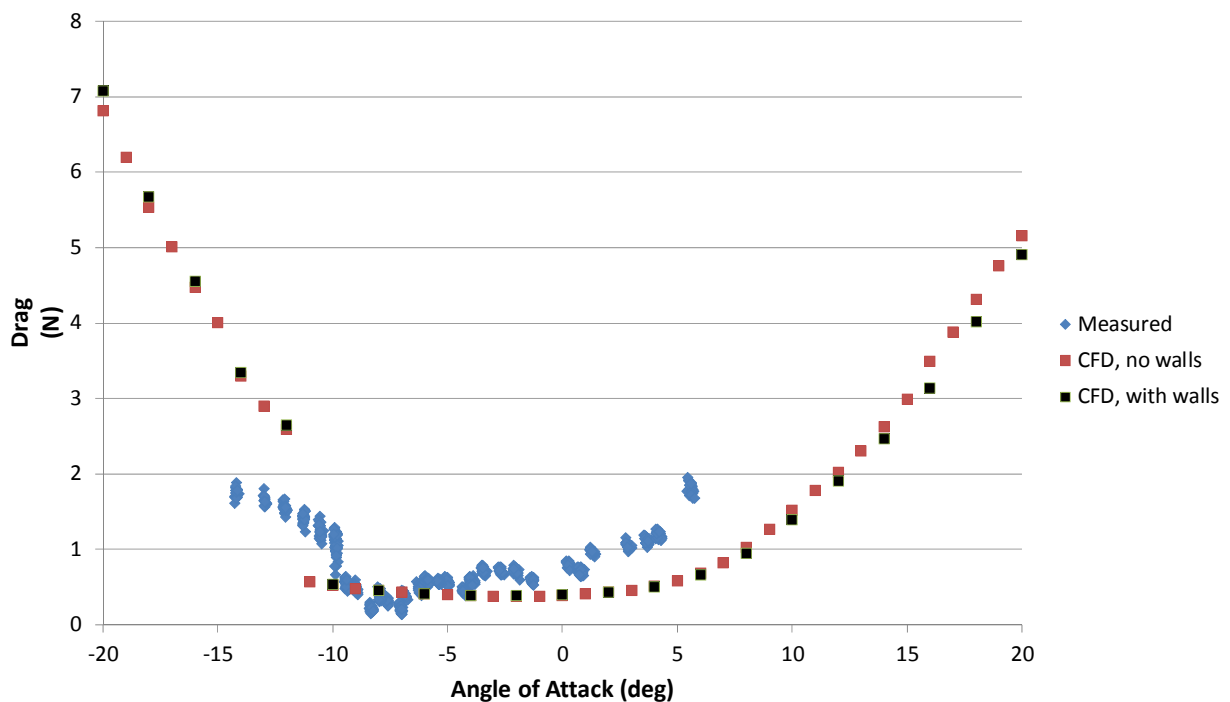
Figure 19. Measured and computed drag forces. *The drag vs angle of attack for the VP20 wing section, with comparison to computations.*

4.5   Recalibration and Updated Measurements without Actuation

As mentioned above, the load cell manufacturer recommended recalibrating the load cells using calibration weights hung from the location where the force is transmitted through the u-joint. Prior to recalibration, we replaced the u-joints with a new pair built to tighter tolerance to remove the rotational slack.

Following recalibration of the load cells, we again compared measured and computed lift. Still seeing a discrepancy in the lift-curve slope, we hypothesized that the simulation was not capturing the turbulent transition accurately and so we re-ran both experiment and simulation with forced transition at 5% of the chord length downstream of the leading edge on the suction side. For the measurement, this was accomplished by taping a trip wire to the wing using Kapton tape. The resulting comparison is shown in Figure 20. The lift-curve slope and zero-lift angle now compare very well. However, the measured lift enjoys an increased slope beginning at about 2 degrees which is not captured by the simulation. This may be due to a separation bubble that is not resolved by the CFD computations. Increasing the mesh density did not improve the comparison. We intend to return to this problem at a later date. See Section 4.7 for further discussion.
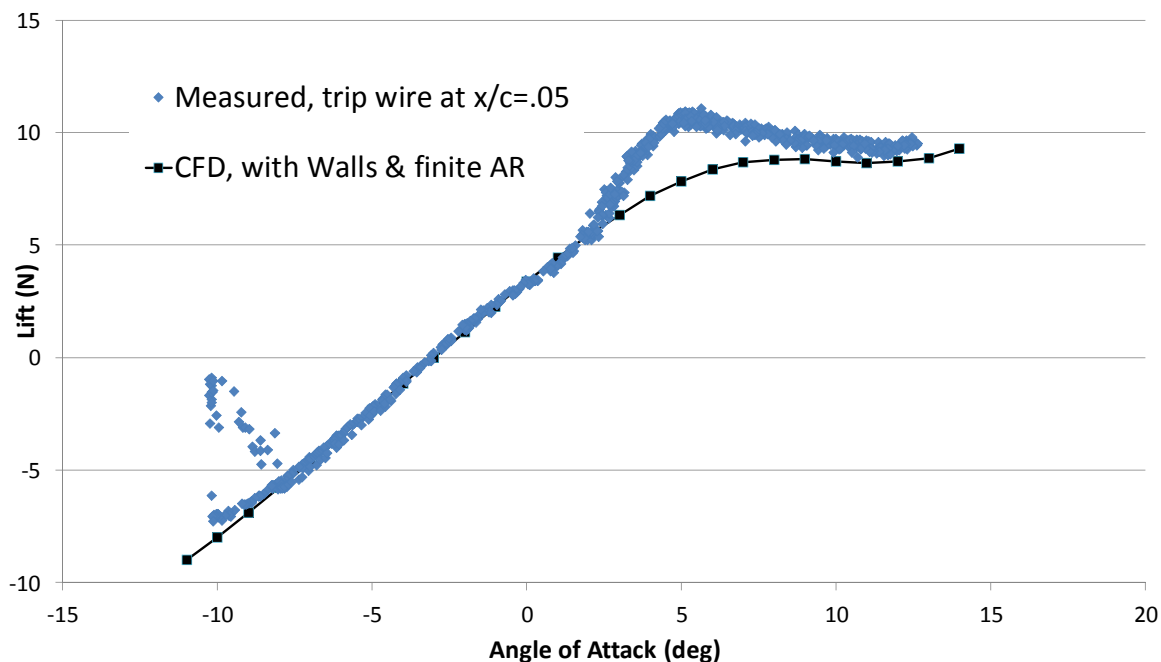
Figure 20. Measured and computed lift, with turbulence trips. *This plot shows measured and computed lift for the VP20 seven-tenths radius section with turbulence trips installed near the leading edge on the suction side.*

4.6   Lift and Drag Measurements with Actuation

For the field demonstration, the VP20 blades will be outfitted with thin, surface-mounted actuators. To determine the best choice of actuator thickness, material and RMS voltage, we performed a series of experiments in the Navatek wind tunnel. We began by measuring lift and drag as a function of angle of attack for the VP20 wing (with the trip wire at 5% chord) with a 20 mil thick Cirlex plasma actuator. This "double actuator" consisted of two parallel strips

Plasma Flow Control for Wind Turbines – Final Report   Navatek, Ltd.

NAVATEK TR--2013/2

spanning the width of the wing (see Figure 21). The actuator was placed so that the downstream edge of the upstream exposed electrode was located at 20% chord, mid-chord, and at 80% chord. For each case, we measured the lift with the actuator attached, but powered off, and again with the actuator powered on. In all cases, the actuator was operated with a constant RMS voltage of 6 kV. No attempt was made to increase actuator control authority, for example by using a serrated exposed electrode, a plasma catalyst, or a modified waveform shape.

Figure 21. The mid-chord mounted double actuator. *This picture shows the double 20 mil Cirlex actuator mounted at the mid-chord position.*

We found that the forward-mounted actuator modified the flow around the wing significantly, resulting in much lower lift (with the actuator turned off) than the bare wing. Therefore, we focused more on the results with the actuator at mid-chord and aft locations. Based on these measurements, we made the following observations:

1. The mid-chord mounted actuator resulted in marginally higher lift than the aft-mounted actuator.

2. The lift is increased over a wide range of angles of attack, from about 2 degrees up to about 20 degrees.

3. The drag coefficients do not appear to be measurably changed by the plasma actuation. In the remainder of this work, we will be focusing on the effect of actuation on lift.

4. It does not look like we are significantly delaying stall with the plasma actuation. Previously, before we added the trip wire, we had seen some differences in stall angle.

The lift as a function of angle of attack for the mid-chord mounted actuator is shown in Figure 22. The measured lift with the actuator off is shown in blue and the data with the actuator on is shown in red. Only the angle-of-attack range over which the actuation made a noticeable difference is shown in the plots.

We are interested in quantifying the percent-gain in lift obtained in our wind-tunnel measurements with the plasma on. At the same time, we want to quantify the uncertainty in the calculation associated with the variability in the data. To accomplish this, we first fit the data with sixth-order polynomials over the region shown on the left of Figure 22. An approximate envelope was then formed for each curve by adding and subtracting a constant offset to each polynomial. Ratios were then taken of the mean curve-fits to form a curve that represents the expected percent-increase in lift (the black curve in each plot on the right of Figure 22). To obtain the upper limit of the expected increase, we took the ratio of the upper-envelope of the plasma-on curve to the lower envelope of the plasma-off curve. This is plotted in green in each plot on the right. Likewise, to find the lower limit of the expected increase, we took the ratio of the curve defining the lower-envelope of the plasma-on curve to the upper limit of the plasma-off curve (shown in blue). In this way, we can estimate the region of expected percent-increase in lift caused by the plasma actuators. This region can be seen in each of the curves on the right side of the figure.

As is evident in the plots on the right-hand-side of Figure 22, there is significant uncertainty in the lift benefit associated with the plasma actuation. As described above, this uncertainty is a direct result of the variability in the lift polars which are shown on the left-hand-side of the figure. That variability could be caused by a combination of inflow turbulence, boundary layer turbulence, flow separation, and measurement error. Also, dynamic effects associated with the changing angle of attack could contribute to the variability.

The average expected increases are shown again as a function of angle of attack in Figure 23. As can be seen in the plot, the maximum increase in lift over the plotted range in angle of attack varied from 13% to 18%, depending on the tunnel speed. Here, we are considering the ratio of the mean trend lines shown in Figure 22.

Similar measurements were made using the triple actuator arrangement shown in Figure 24. The lift curves are shown in Figure 25, along with the polynomial trend lines and their ratios. Figure 26 shows the ratios of the mean trend lines for each tunnel speed. For the triple actuator, the maximum increase in lift over the angle of attack range 2–20 degrees can be seen to vary from 19% to 23%.
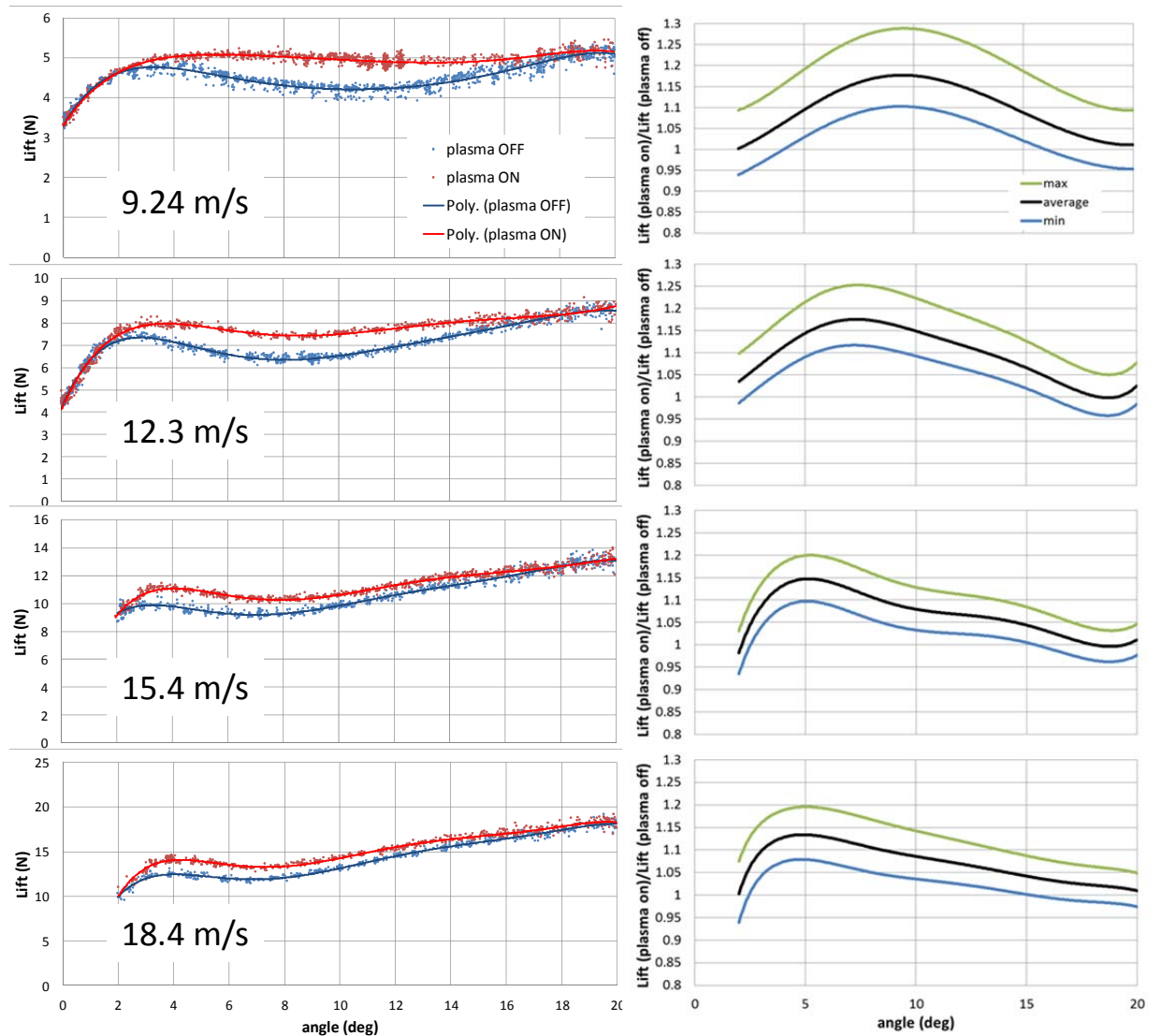
Figure 22. Lift enhancement for the 20-mil Cirlex double actuator. *These plots show measured lift vs. angle of attack for the mid-chord mounted 20 mil Cirlex double actuator, operated at 6 kVrms and 2 kHz. The plots on the right show the ratios of the mean trend lines for the plasma-on and plasma off, along with estimates of the upper (green) and lower (blue) limits of the expected increase.*
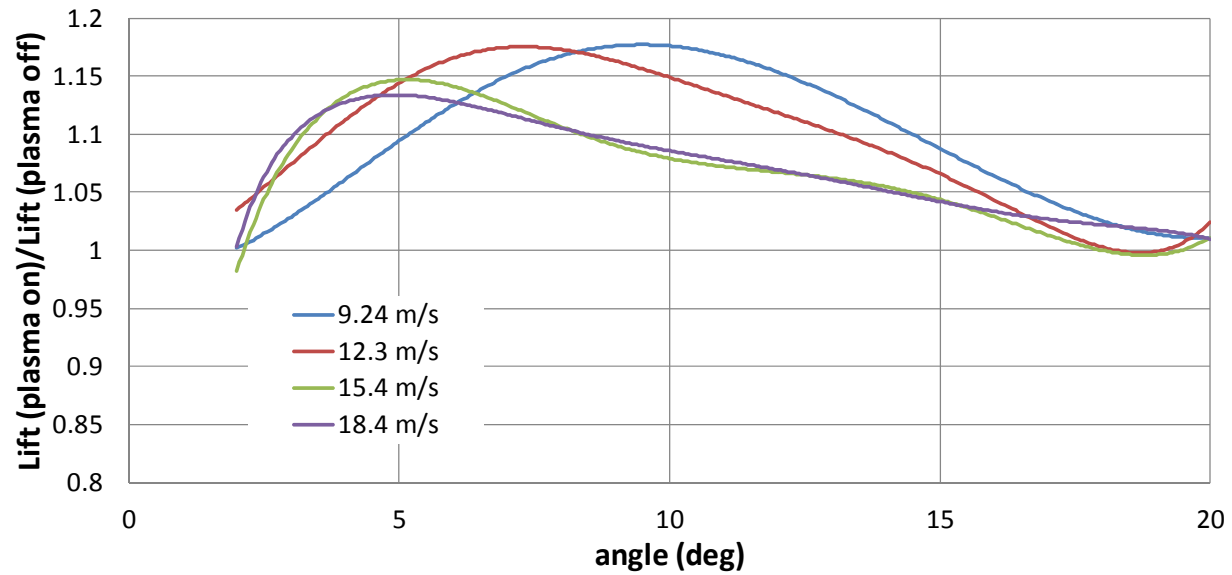
Figure 23. Quantification of plasma-enhanced lift, double actuator. *This plot shows the ratio of lift with plasma on to lift with plasma off for the 20 mil Cirlex double actuator, derived from the trend lines plotted in Figure 22.*

Figure 24. The mid-chord mounted triple actuator. *This picture shows the triple 20 mil Cirlex actuator mounted at the mid-chord position.*

Plasma Flow Control for Wind Turbines – Final Report   Navatek, Ltd.

NAVATEK TR--2013/2
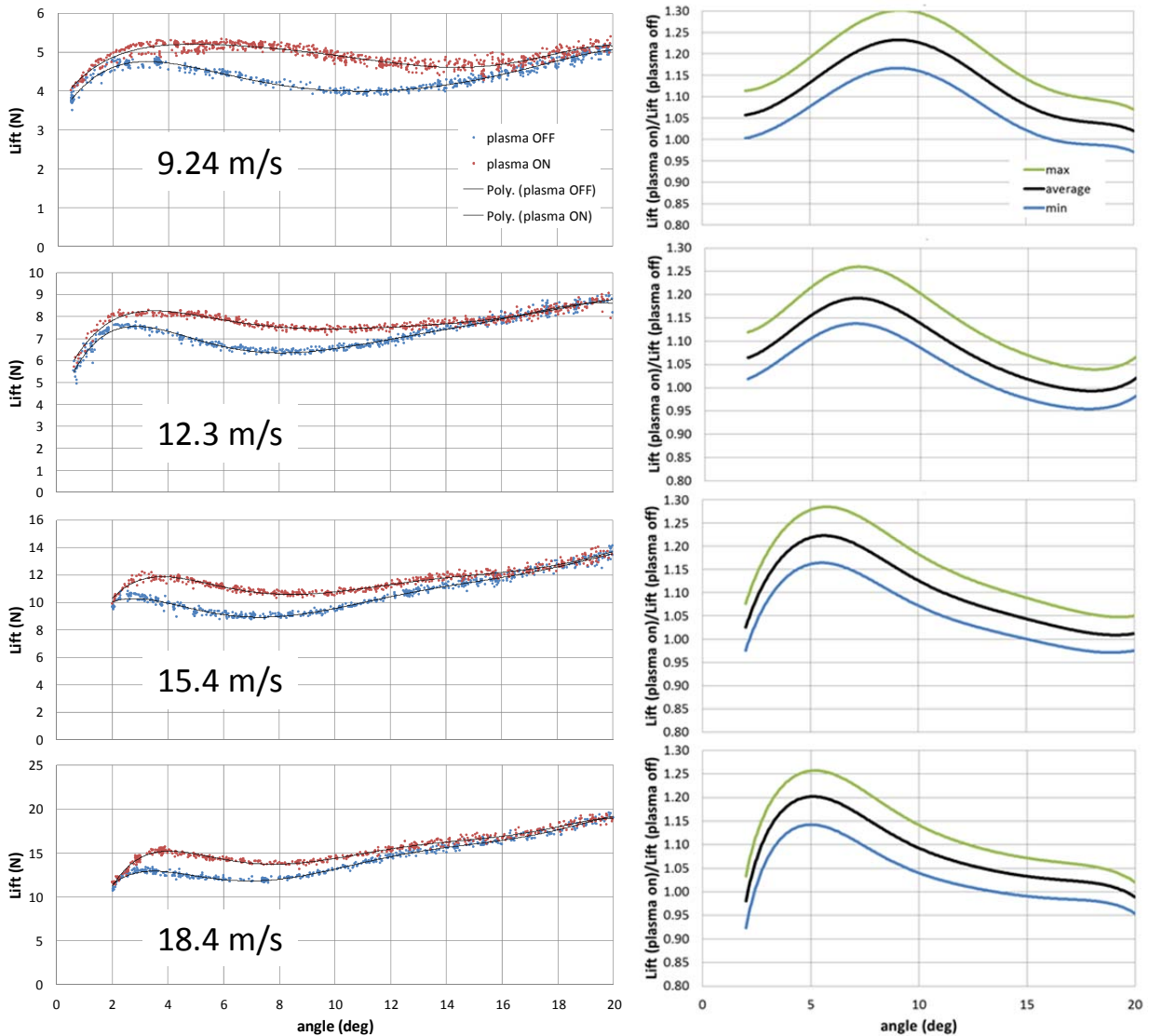
Figure 25. Lift enhancement for the 20-mil Cirlex triple actuator. *These plots show measured lift vs. angle of attack for the mid-chord mounted 20 mil Cirlex triple actuator, operated at 6 kVrms and 2 kHz. The plots on the right show the ratios of the mean trend lines for the plasma-on and plasma off, along with estimates of the upper (green) and lower (blue) limits of the expected increase.*
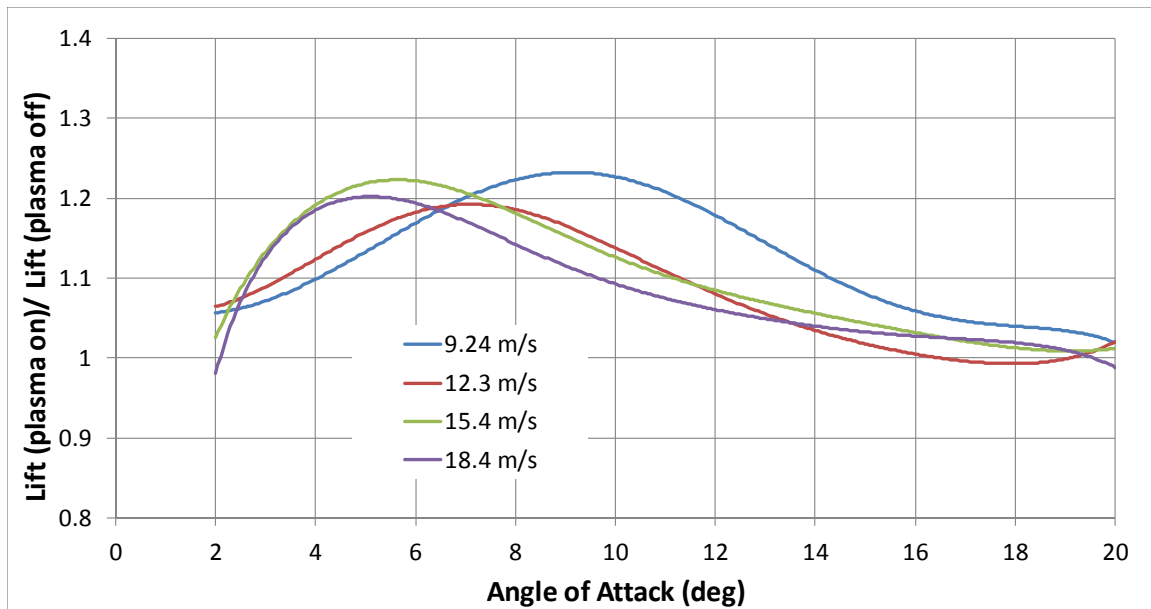
Figure 26. Quantification of plasma-enhanced lift, triple actuator. Ratio of lift with plasma on to lift with plasma off for the 20 mil Cirlex triple actuator, derived from the trendlines plotted in Figure 25.

We also tested two chordwise arrangements of actuators using the 20-mil Cirlex dielectric. The first chordwise arrangement is shown in Figure 27, and the second is shown in Figure 28. The goal of using actuators in this way is to delay or prevent trailing edge separation and stall by producing pairs of counter-rotating vortices that have the effect of bringing high-momentum air into the boundary layer over significant fractions of the chord. Resulting lift curves are shown in Figure 29 for tunnel test section speed of 18.3 m/s. Clearly, the presence of the actuators had the opposite of the intended effect because the lift with the actuator was significantly lower at mid-to-high angle of attack than the bare-wing. Furthermore, for both chordwise arrangements, the lift with the actuators on did not show any appreciable improvement in comparison the lift with the plasma off.

It is likely that the two chordwise arrangements studied here were far from the optimal spanwise spacing. However, since so little effect was measured, we are abandoning this approach for the time being and going with the conventional spanwise actuator arrangement for the current full scale test design. We intend to return to this topic in future research.
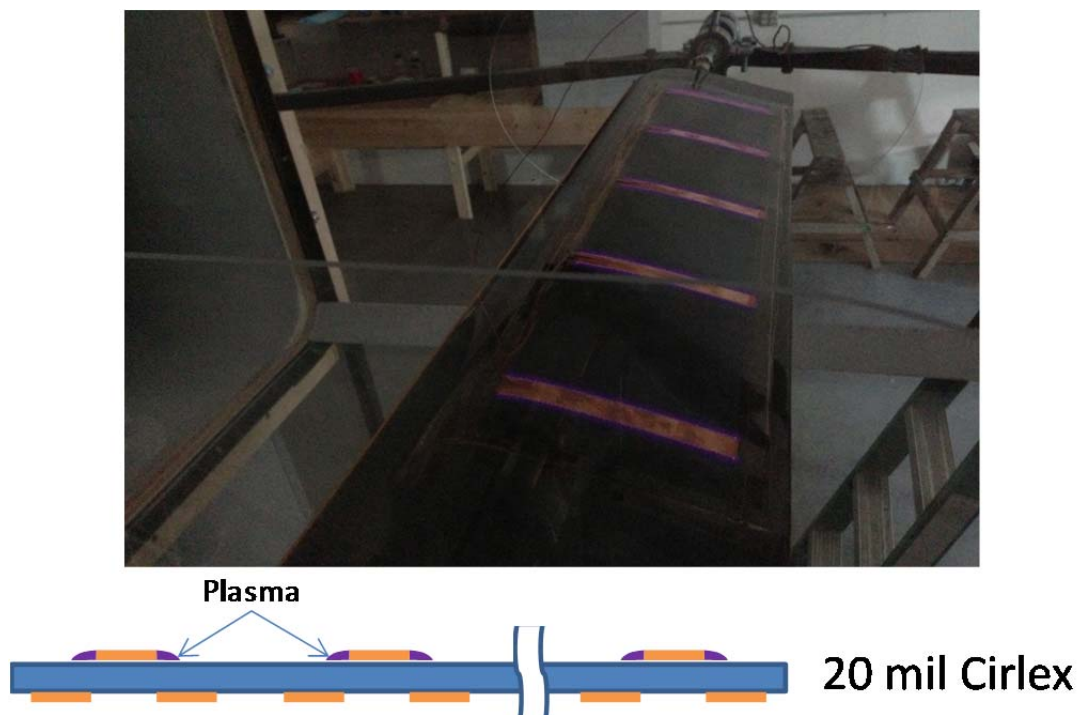
Figure 27. First chordwise actuator configuration. *The schematic below the picture shows the arrangement of the electrodes.*
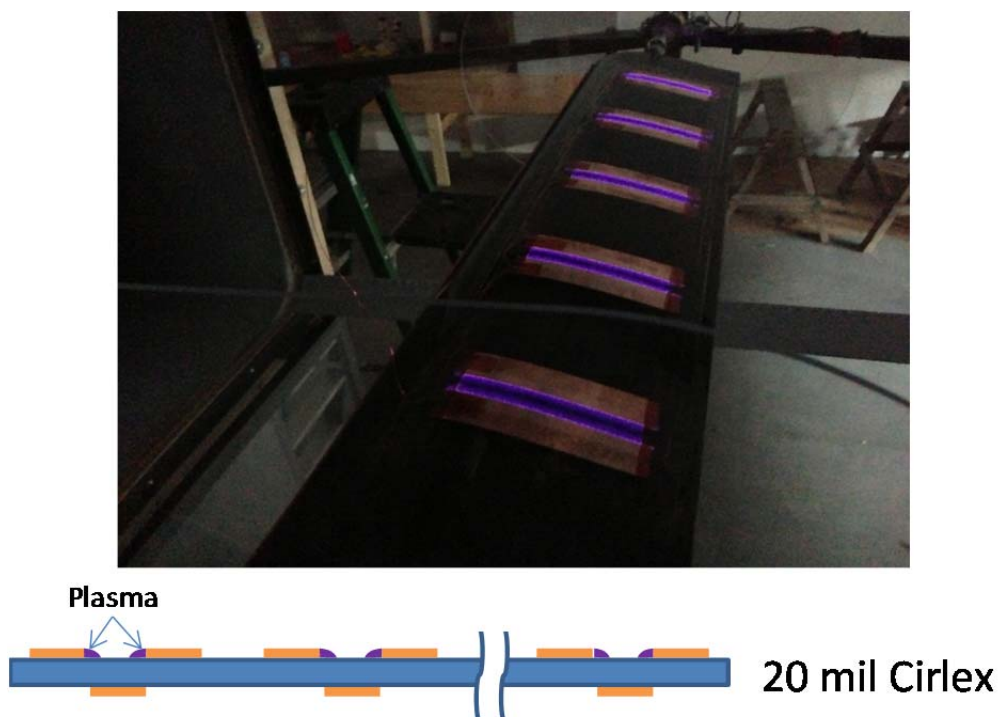
Figure 28. Second chordwise actuator configuration. *The schematic below the picture shows the arrangement of the electrodes.*
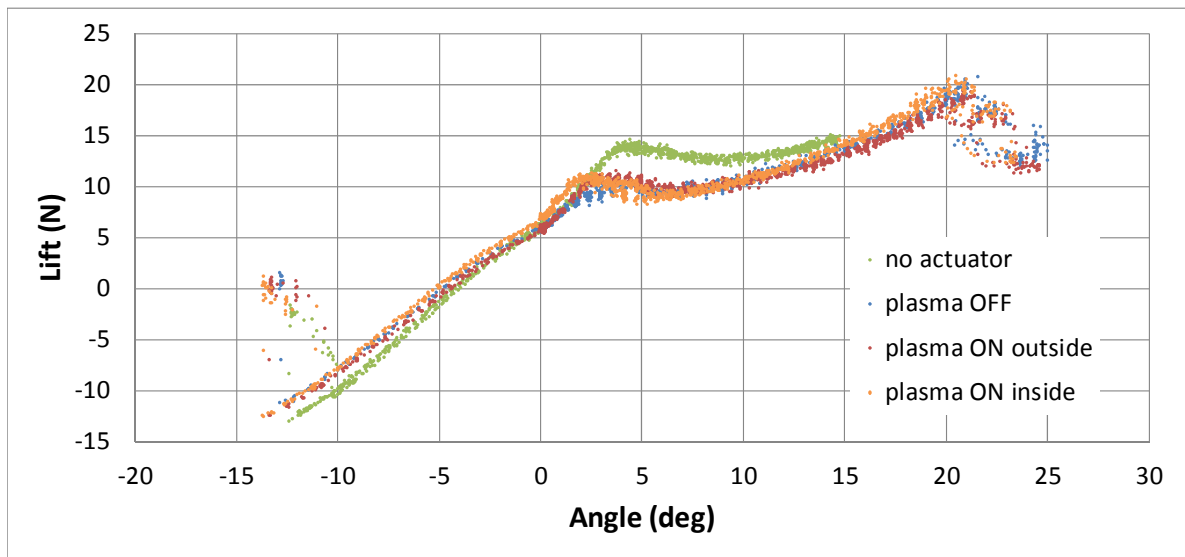
Figure 29. Measured lift with chordwise-mounted actuators. *This plot shows lift with and without plasma actuation in the chordwise orientation shown in Figure 27 and Figure 28. The curve labeled "plasma ON outside" refers to the arrangement pictured in Figure 27, while the curve labeled "plasma ON inside" refers to the arrangement pictured in Figure 28.*

4.7   Conclusions

The intent of the tasking reported in this Section was to collect data to guide our selection of actuator material, thickness and blade positioning for the field demonstration on the VP20 wind turbines. Because the 40-mil thick actuators degraded the performance of the wing significantly, we selected a thinner actuator (roughly 20 mils thick). Since the forward-mounted thin actuator also degraded the performance relative to mid-chord and aft-mounted actuators, we chose to mount the actuators closer to the trailing edge to prevent the protuberance of the actuator from inducing boundary layer separation. Although the triple-actuator provided a proportional increase in lift, space limitations near the tip of the blade, along with actuator construction considerations led us to select a double-actuator throughout the span of the blade.

The lift data was also used to estimate the increase in power generation that could be expected from the wind turbines with the plasma actuators powered on. That is the subject of Section 7.

5. Lift Measurements in the Brown University Wind Tunnel

Additional wind tunnel testing was conducted at Brown University's low speed wind tunnel. Brown's tunnel is high fidelity with known measured turbulence values which makes it is useful for validating results from the Navatek tunnel. It also has some advanced capabilities that the Navatek tunnel does not. The test section is equipped with a 2-axis air bearing system that is cable of directly measuring lift and drag. The wing in this tunnel must be mounted vertically. The test section measures only 23.6 in high (compared to 36 in for the Navatek tunnel) so new full-scale wings were fabricated with a smaller aspect ratio to maintain a span equal to 80% of the test section height. Endplates of the same size and shape were used. Angle of attack was automatically controlled with a stepper motor and encoder. A diagram, CAD model, and photo of the experimental setup are shown in Figure 30.
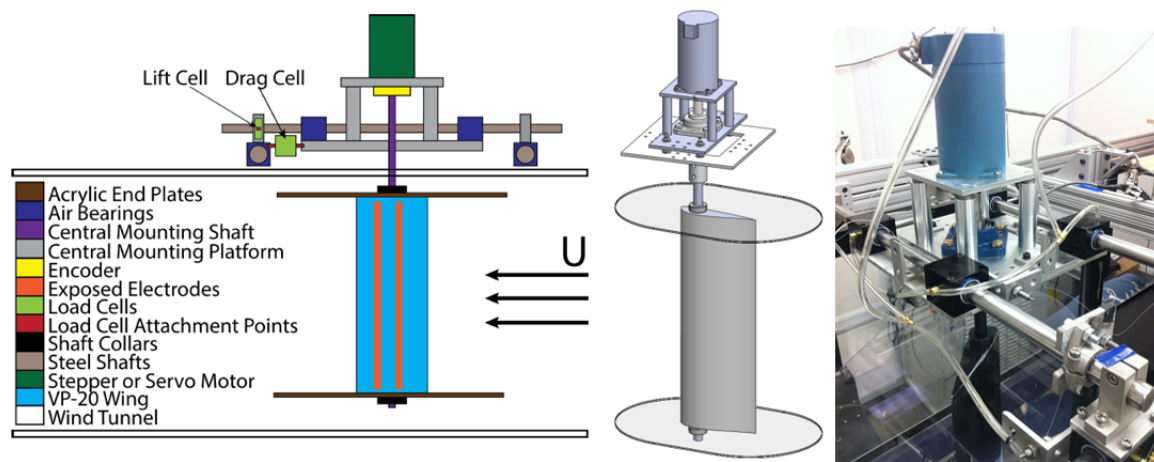
Figure 30. Experimental setup at Brown University. *The schematic on the left depicts an elevation view of the side of the tunnel, showing the arrangement of the wing, mounting apparatus and force measurement device. The 3D CAD model (middle) was used to design the mounting system. A picture of the final product is shown on the right.*

A first test wing was cut from polystyrene buoyancy billet with the CNC hotwire foam cutter and finished with epoxy resin. It is shown in Figure 31. The finished wing compares very closely in shape and size with the actual airfoil profile.

Figure 31. Test wing for use in Brown's wind tunnel. *A preliminary test wing was fabricated without an actuator using a foam core and epoxy resin.*

This wing was used to work out bugs in the test rig at Brown and results were compared to the lift results for the bare wing in our tunnel. A second wing was created in a similar way with a notch cut out to mount a 3/16" thick Macor® double actuator flush with the surface of the wing. Macor® is a machinable ceramic made by Corning, Inc. that has proven to be a robust actuator dielectric material. This thick embedded actuator configuration is predicted to provide a large increase in the coefficient of lift with minimal impact on the baseline aerodynamics of the wing. The geometry of the embedded actuator is shown in Figure 32.
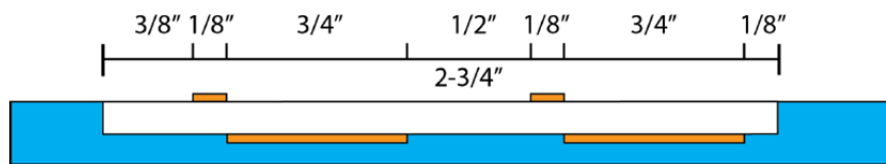
Figure 32. Embedded Macor® double actuator geometry. *This side view schematic shows the arrangements of the electrodes on the actuators. The thickness of the Macor® dielectric is188 mils. The blue substrate represents the foam core of the wing.*

The wing and Macor® actuator were finished together to create a continuous smooth surface. Figure 33 shows the finished wing with and without the plasma ignited. Later, a boundary layer trip strip was added to the suction side of this wing at 5% chord downstream of the leading edge.

Figure 33. Test wing with embedded actuator. *The picture on the left shows the purple glow of the plasma with the actuator energized.*

Results of the testing at Brown successfully validated the data we had been using from our tunnel. Lift curves showed similar shape and behavior. The addition of a trip strip had the same effect of delaying stall and creating a relatively flat region of high lift at the expense of a lower maximum lift. There were small differences that could be explained by different background turbulence levels, aspect ratios, and blockage effects. Figure 34 shows lift coefficient with and without plasma for the wing with embedded actuator at the Brown facility and the most similar experiment in our lab. Both wings had identical trip strips at 5% chord.
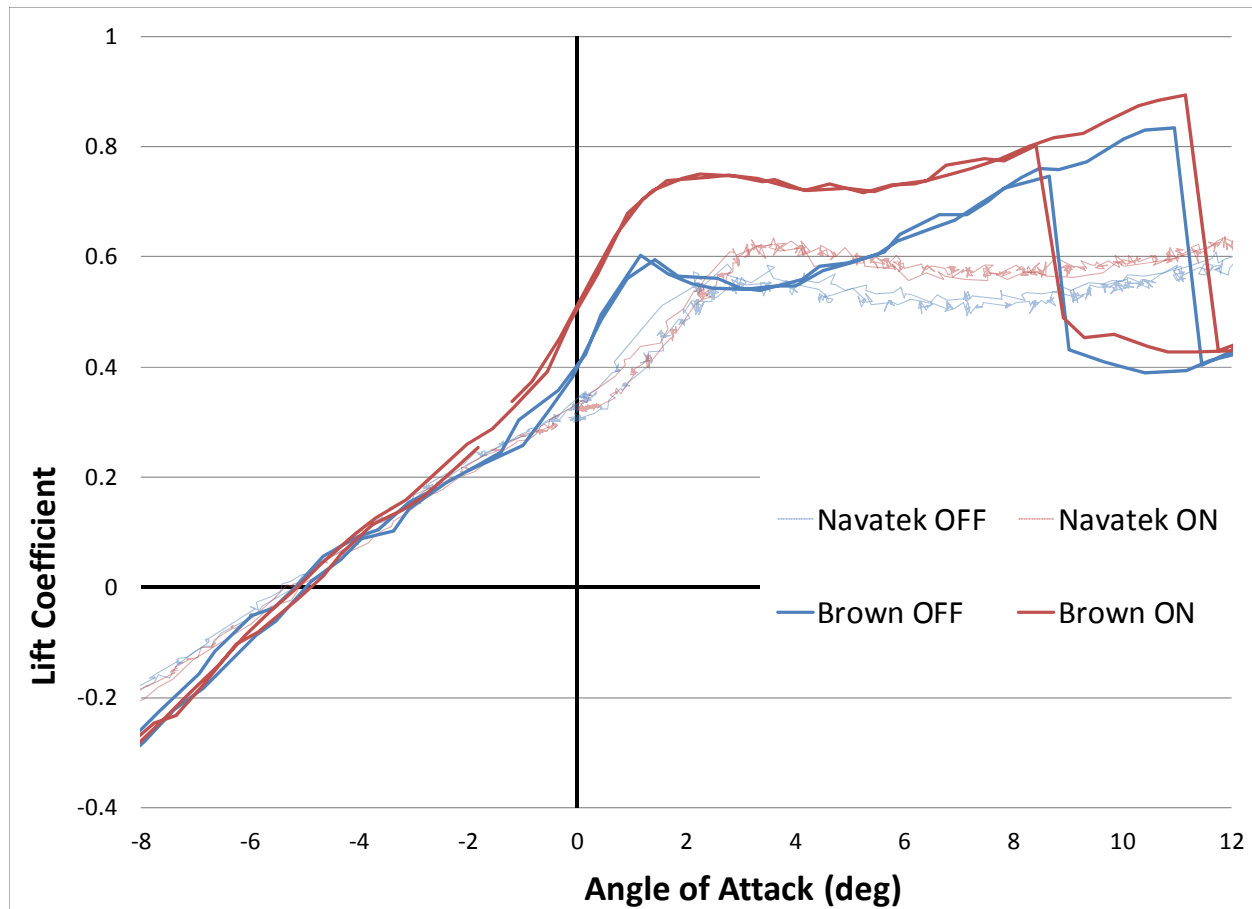
Figure 34. Lift polar comparison between Brown and Navatek tests. *This plot shows the lift coefficient as a function of angle of attack for the VP20 wing in the two wind tunnels. This is intended to be a qualitative comparison only, as described in the text.*

The test at Brown used a 188 mil embedded Macor® double actuator at 12kV and a wind speed of 14.5 m/s. The test at Navatek used a 20 mil surface mounted Cirlex actuator at 6.5 kV and a wind speed of 15.4 m/s. Both actuators contained two lines of actuation at approximately 50% and 70% chord. Angle of attack for the Brown test should be considered relative as a zero angle of attack could only be approximated to within a few degrees. While there are many differences between these tests, comparing them is still useful. With the plasma off, the Brown test shows a higher coefficient of lift as there is no boundary layer disturbance from a surface mounted actuator. Both show an increase in coefficient of lift with plasma on in the same range of angles of attack. As expected, the higher voltage embedded actuator has a more pronounced effect. The surface mounted actuator provided a maximum increase in lift of about 15% while the embedded actuator had a maximum increase of about 37%. This clearly demonstrates the advantages of embedding actuators.

The Brown facility also had a smoke-wire flow visualization system. It creates many fine trails of smoke that follow the streamlines of the flow. Figure 35 shows two frames from a video recorded in the Brown wind tunnel.
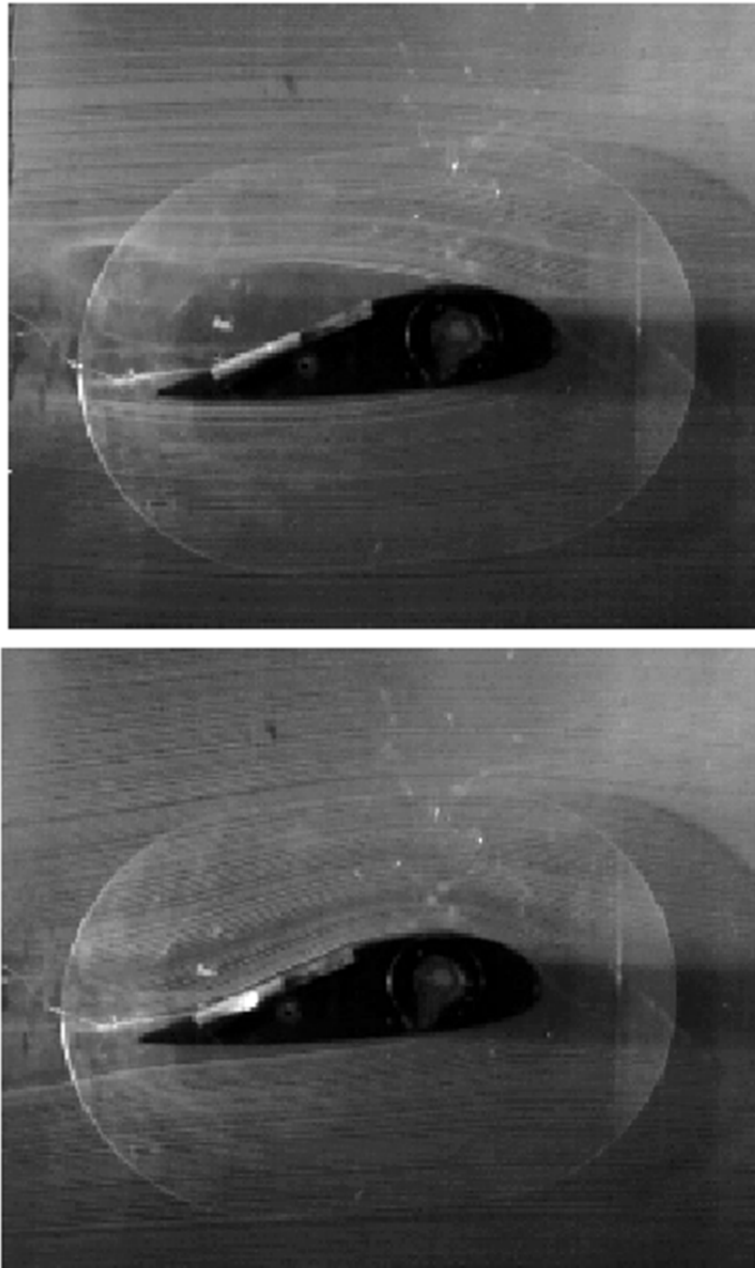
Figure 35. Flow visualization with and without plasma. *These two pictures show plasma induced boundary layer reattachment of a stalled airfoil.*

The frame on the top shows the wing stalled with plasma off at an angle of attack of about 10 degrees in 2 m/s flow. Boundary layer separation is clearly visible. The frame on the bottom shows the wing moments later at the same angle of attack but after the plasma has been turned on (at 6 kV). The flow has become cleanly reattached and the streamlines at the trailing edge are diverted downward.

6.   Simulations

6.1   Wind Turbine Performance Modeling

Wind turbine performance is simulated using the classic Blade Element Method, which we will review in this Section. The Blade Element Method is essentially a spanwise discretization of ideal blade theory (sometimes called infinite blade theory or actuator disk theory) wherein the 3D blade characteristics are accounted for in a strip-wise sense. Each radial section of the blade is treated as a 2D flow with local corrections accounting for the influence of the trailing wake. The strength of this approach is the relative speed of computation (compared to fully 3D approaches such as inviscid integral equation approaches and Reynolds-Averaged Navier-Stokes solutions). The main weakness is the neglect of cross-flow effects and the inviscid and viscous "communication" between spanwise strips.

We follow the classic blade element formulation, as described originally by Glauert (Glauert, 1935). The derivation assumes that there are an infinite number of blades, so that the thrust and torque developed at each section is spread over an annulus of area *2πrdr* (see Figure 36). The rotor diameter is R.
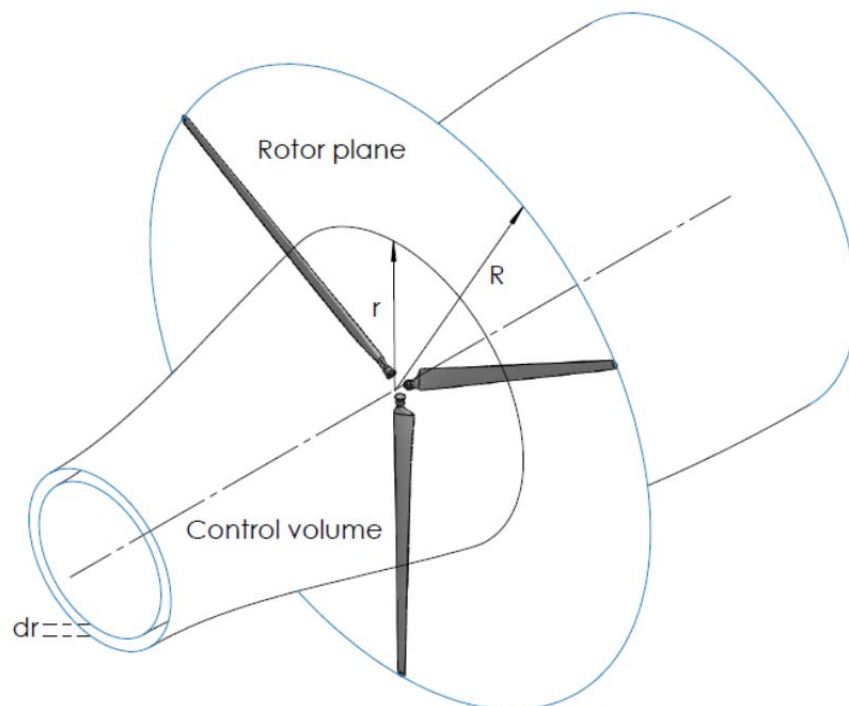
Figure 36. Control volume used in BEM analysis. *This illustration shows the annular control volume used to define the differential thrust and moment defined in Equations 6-1 and 6-2.*

From actuator disk theory, we know that the annular element of radius r and width dr experiences a differential thrust *dT* given by

$$dT = 4\pi r \rho V_0^2 a (1-a) dr \qquad (6-1)$$

and differential moment dM given by

$$dM = 4\pi r^2 \rho V_0 \omega (1-a)a'dr .$$
(6-2)

The relative velocity V_{rel} as seen by a section of the blade is a combination of the axial velocity $(1 - a)V_o$ and the tangential velocity $(1 + a')\omega r$ at the rotor plane (see Figure 37), where V_0 is the wind speed, a and a' are the local axial and rotational induction factors, and ω is the turbine's rotational speed in radians/sec. The twist angle is given by θ.
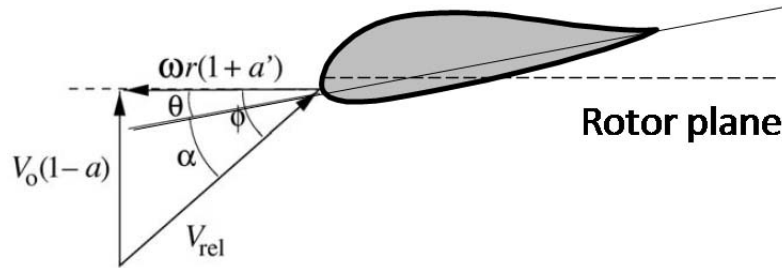
Figure 37. Velocities in the rotor plane. *The classic Blade Element Method uses this velocity decomposition in the plane of the rotor.*

From Figure 37, it is clear that the local 2D angle of attack is

$$\alpha = \phi - \theta$$
(6-3)

It is also evident that

$$\phi = \tan^{-1}\left[\frac{(1-a)V_0}{(1+a')\omega r}\right].$$
(6-4)

The lift and drag are by definition the forces felt by the blade section in the direction perpendicular to and parallel to, respectively, the relative velocity, V_{rel}. In this analysis we will assume that the lift and drag coefficients (C_L and C_D) are known as a function of the angle of attack, α. L and D are the lift and drag, respectively, per unit length (because they are planar forces), defined in terms of the coefficients as follows:

$$L = \frac{1}{2}\rho V_{rel}^2 cC_L$$
(6-5)

$$D = \frac{1}{2}\rho V_{rel}^2 cC_D .$$
(6-6)

Since we are interested only in the force normal to (F_n) and tangential to (F_t) the rotor plane, the lift and drag are projected into these directions (see Figure 38):

Plasma Flow Control for Wind Turbines – Final Report   Navatek, Ltd.

NAVATEK TR--2013/2

$$F_n = L\cos\phi + D\sin\phi \qquad\qquad (6\text{-}7)$$

$$F_t = L\sin\phi - D\cos\phi . \qquad\qquad (6\text{-}8)$$
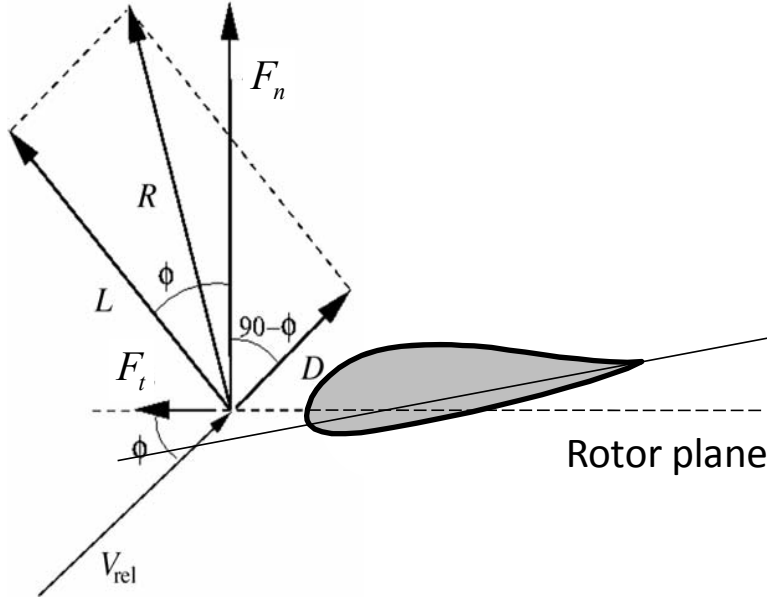
Figure 38. Local forces on the blade. *R is the vector sum of the lift L and the drag D; F_n and F_t are the normal and tangential components of R, respectively.*

Defining the normal and tangential force coefficients then yields

$$C_n = \frac{F_n}{\frac{1}{2}\rho V_{rel}^2 c} = C_L\cos\phi + C_D\sin\phi \qquad\qquad (6\text{-}9)$$

$$C_t = \frac{F_t}{\frac{1}{2}\rho V_{rel}^2 c} = C_L\sin\phi - C_D\cos\phi . \qquad\qquad (6\text{-}10)$$

The shaft power is then computed by summing the incremental contributions to the torque (tangential force multiplied by the radius of each element) and multiplying by the number of blades, *B*, and the shaft rotation rate, ω.

Recall that the induction factors *a* and *a'* are unknown. We therefore seek expressions that will allow us to compute those quantities. To do that, we first express the differential thrust and moment in terms of C_n and C_t as follows:

$$dT = BF_n dr = \frac{1}{2}\rho B V_{rel}^2 c C_n dr = \frac{1}{2}\rho B \frac{V_0^2(1-a)^2}{\sin^2\phi} c C_n dr \qquad\qquad (6\text{-}11)$$

$$dM = rBF_t dr = \frac{1}{2}\rho B V_{rel}^2 cC_t rdr = \frac{1}{2}\rho B \frac{V_0(1-a)\omega r(1-a')}{\sin\phi\cos\phi}cC_t rdr \qquad (6\text{-}12)$$

Referring again to Figure 37, we have used two ways of expressing V_{rel} in terms of V_0, a, a' and ϕ. B is the number of rotor blades. We now derive the two required expressions by equating the right hand sides of Equations (6-1) and (6-11) and those of (6-2) and (6-12).

$$\frac{1}{2}\rho B \frac{V_0^2(1-a)^2}{\sin^2\phi}cC_n dr = 4\pi\rho V_0^2 a(1-a)rdr \qquad (6\text{-}13)$$

$$\frac{1}{2}\rho B \frac{V_0(1-a)\omega r(1-a')}{\sin\phi\cos\phi}cC_t rdr = 4\pi\rho V_0\omega(1-a)a'r^2 dr \qquad (6\text{-}14)$$

By introducing the solidity factor, σ:

$$\sigma(r) = \frac{c(r)B}{2\pi r} \qquad (6\text{-}15)$$

Equation (6-13) can be reduced to

$$a = \frac{1}{\dfrac{4\sin^2\phi}{\sigma C_n}+1} \qquad (6\text{-}16)$$

and Equation (6-14) reduces to

$$a' = \frac{1}{\dfrac{4\sin\phi\cos\phi}{\sigma C_t}-1} \qquad (6\text{-}17)$$

The BEM procedure is implemented through the following algorithm:

1. Define the blade geometry as a function of radius (typically chord length and twist angle, although one could generalize to include sweep and rake angles).

2. Initialize a and a' (typically to zero).

3. Compute the local flow angle, $\phi(r)$, using Equation (6-4).

4. Compute the local 2D angle of attack, $\alpha(r)$, using Equation (6-3).

5. Interpolate $C_L(\alpha)$ and $C_D(\alpha)$ from a look-up table.

6. Compute a and a' using Equations (6-16) and (6-17). Loop over steps 3 through 6 until these values converge to within some preset tolerance.

7. Compute the local loads, integrate to obtain thrust and torque, and use the latter to determine shaft power.

This is the basic blade element method, but two corrections are generally applied: Prandtl's tip loss factor and Glauert's correction for high induction factor. Prandtl's tip loss factor attempts to correct for the assumption of an infinite number of blades. The correction factor, F, is defined as

$$F = \frac{2}{\pi} \cos^{-1}(e^{-f})$$
(6-18)

where

$$f = \frac{B}{2} \frac{R-r}{r \sin \phi}$$
(6-19)

The induction factors are modified as follows:

$$a = \frac{1}{\dfrac{4F \sin^2 \phi}{\sigma C_N} + 1}$$
(6-20)

and

$$a' = \frac{1}{\dfrac{4F \sin \phi \cos \phi}{\sigma C_T} - 1}$$
(6-21)

Equations (6-20) and (6-21) should be used in place of Equation (6-16) and (6-17) in step 6 of the algorithm outlined above.

The blade element method is not valid for high induction factor (typically a>0.4). Glauert's correction is a semi-empirical method to correct the BEM for high induction factor. For induction factors greater than some preset value (typically a_c=0.2), Equation (6-20) is replaced by

$$a = \frac{1}{2}\left[2 + K(1 - 2a_c) - \sqrt{(K(1 - 2a_c) + 2)^2 + 4(Ka_c^2 - 1)}\right]$$
(6-22)

where

$$K = \frac{4F \sin^2 \phi}{\sigma C_n}.$$
(6-23)

The BEM is a very fast approach that many wind turbine designers use to estimate power generation. For this to be useful, however, we must have good 2D lift and drag data. Further, for this tool to be useful in evaluating the potential benefit(s) of plasma flow control, we must be

able to incorporate the effects of flow control on the local 2D lift and drag coefficients. Since the principle of flow control is to control the viscous lift and drag forces, it's our intention to apply a commercial Reynolds averaged Navier-Stokes (RANS) code and a separate lumped element electrostatic solver to compute the plasma actuation forces.

6.2   2D Lift and Drag Computations

XFOIL

The 2D lift and drag tables used in the wind turbine performance calculations (see Step 5 of the BEM algorithm described on the previous page) can be computed using XFOIL. XFOIL is a 2D interacted boundary layer solver written by Professor Mark Drela of MIT (see, for example, (Drela, 1989)). XFOIL is a commonly used tool for airfoil design and analysis, and is available for download under the gnu free software license. However, this tool will only provide us with baseline lift and drag tables before actuation is applied. To model the effects of the plasma actuators, we need to turn to other computational tools.

FINE™ CFD

Navatek uses a computational fluid dynamics (CFD) tool sold by Numeca International, called FINE™ Marine. This tool is designed for high-fidelity computations of multiphase flows and free-surface hydrodynamics and is used by Navatek for ship design studies. Since Navatek owns a license to the tool, we decided to work with Numeca to develop a User Defined Function that would permit us to apply the tool to unbounded lifting surface flows with actuation and without a free surface. Prior to modeling the actuator, we performed a systematic study to verify that the code can produce mesh-independent results for a 2D airfoil with no free surface. The shape selected was a symmetric NACA 00 section with maximum thickness equal to 10% of the chord length. Results are shown in Figure 39 for a Reynolds number of 709,000, in which the lift coefficient predicted by FINE™ Marine is compared to that predicted by XFOIL. The consistency of the two solutions, coupled with convergence studies of the CFD solution (not shown), give us confidence that FINE™ Marine is producing accurate results.
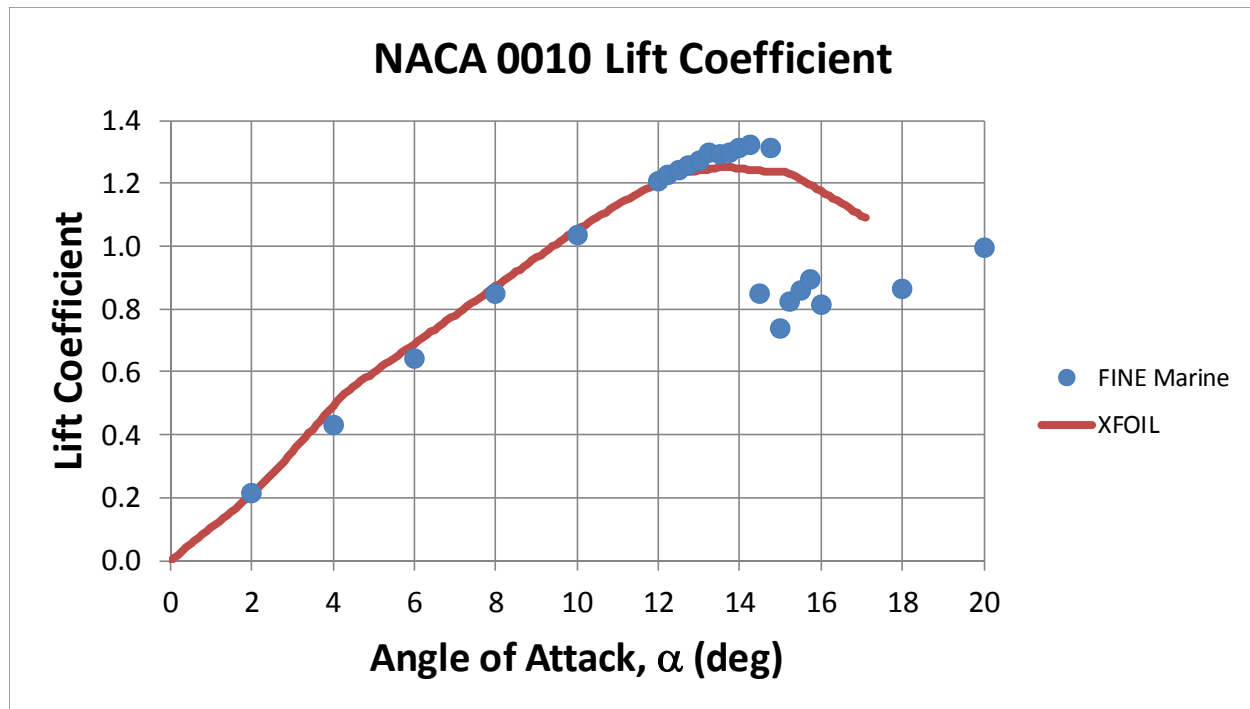
Figure 39. **Verification of the CFD tool, FINE™ Marine.** *This plot shows lift coefficient for a NACA0010 airfoil, computed with FINE™ Marine and XFOIL.*

User Defined Function

The effect of a plasma actuator on the flow can be captured by including a body force distribution on the computational cells adjacent to the fluid boundary where the actuator is mounted. In order to include a body force in FINE™ Marine, Numeca built a User Defined Function (UDF) interface. The UDF allows the user to define a body force vector at any number of nodes over a defined geometric patch. For a test case, we modeled flow in a box, with an actuator in the center of the bottom of the box. The initial condition was stationary flow throughout the volume. The actuator is then abruptly started, forming a wall jet on the bottom of the box. This was intended to simulate an experiment published in the PhD Thesis by M. Post (Post, 2004). Since numerical data was not published in the thesis, we can only make qualitative comparisons. Figure 40 shows a snapshot in time of velocity contours. The results show the starting vortex and are in qualitative agreement with the measurements of Post (Figure 41). Unfortunately, there is not enough data published in the Post thesis to make quantitative comparisons. However, the peak velocities are consistent, as are the size and motion of the starting vortex.
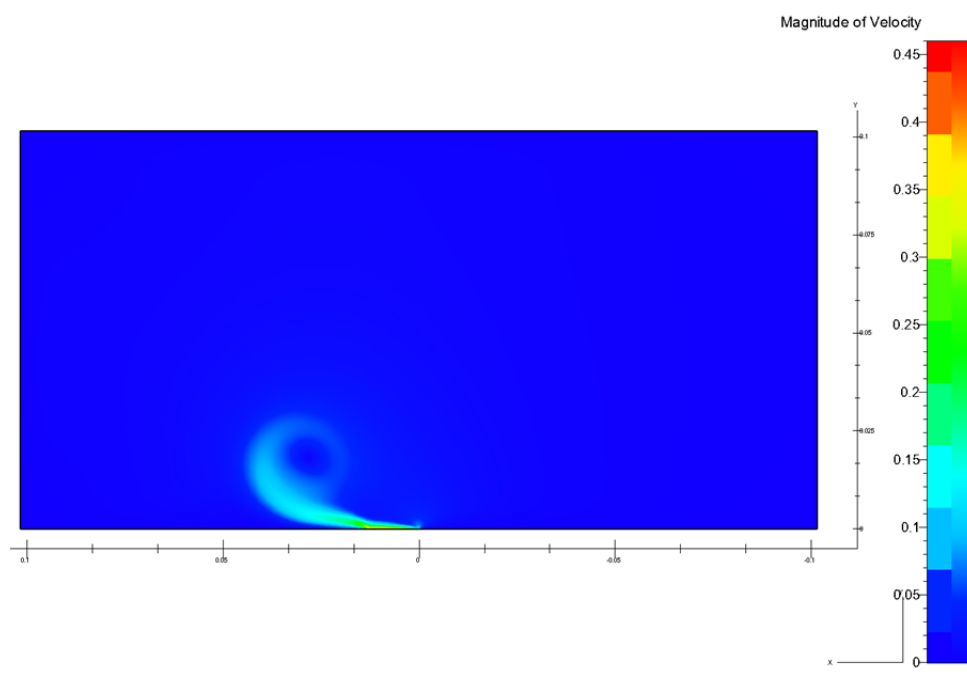
Figure 40. Verification of the UDF: computations. *This contour plot shows computed velocity for an actuator fixed to the floor of a box.*
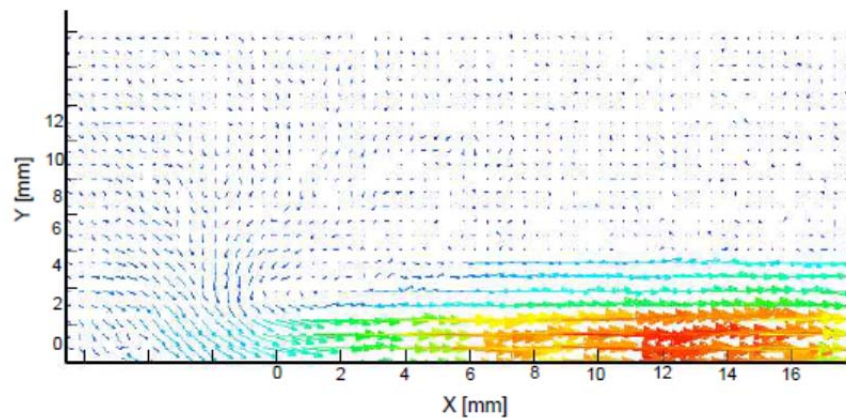
Figure 41. Verification of the UDF: measurements. *A close-up view of the measured velocity for an actuator in a box (from* **(Post, 2004)***.*

Electrostatic Actuator Model

Now that we have a UDF that will allow us to model the plasma actuator in FINE™ Marine, we need a way to compute the body force distribution. One way to do that is to implement the lumped element electrostatic model developed by Corke et. al (Corke, Enloe, & Wilkinson, 2010). To begin, we note that ions are formed in the plasma through electron-neutral collisions with a characteristic time scale on the order of 10^{-8} seconds. Meanwhile, the electric field is varying on the time scale associated with the AC frequency, or on the order of 10^{-3} seconds. The five orders of magnitude in characteristic time between these two phenomena allow us to

separate the process of ion formation from that of the action on the neutral background gas. The electrons and ions will arrange themselves to reach static equilibrium under the influence of the instantaneous electric field. Since all of the momentum gained by the background gas comes from collisions with ions, it is clear that the force can be described essentially as an electrostatic one resulting from the action of the electric field on the distribution of charged species in the plasma. Such a force is simply computed by the expression

$$\vec{F}_b = \rho_C \vec{E} \tag{6-24}$$

where ρ_C is the charge density and $\vec{E}$ is the electric field. The body force, $\vec{F}_b$, is the force per unit volume of the plasma.

Boltzmann's equation relates the local ion and electron density to the electrostatic potential, φ:

$$n_{i,e} = n_0 \exp\left[\mp \frac{e\varphi}{kT_{i,e}}\right] \tag{6-25}$$

where n_0 is the plasma density, e is the charge of an electron, k is Boltzmann's constant and T is the ion or electron temperature. Using this equation, the charge density can be written

$$\rho_C = e(n_i - n_e) \approx e n_0 \left[\frac{e\varphi}{kT_i} + \frac{e\varphi}{kT_e}\right] = \frac{e^2 n_0 \varphi}{k}\left[\frac{1}{T_i} + \frac{1}{T_e}\right] \tag{6-26}$$

Making use of the definition of the Debye length, λ_D

$$\lambda_D^2 = \frac{\varepsilon_0 k}{e^2 n_0 \left[\frac{1}{T_i} + \frac{1}{T_e}\right]} \tag{6-27}$$

the charge density can be written

$$\rho_C = -\frac{\varepsilon_0}{\lambda_D^2}\varphi \tag{6-28}$$

The Debye length is a characteristic length scale for electrostatic shielding in a plasma.

The actuator force is a direct result of the fact that there is an electric field in the plasma in regions where there is also a net charge density. The force per unit volume on the plasma can now be written

$$\vec{F}_b = \rho_C \vec{E} = -\frac{\varepsilon_0}{\lambda_D^2}\varphi\vec{E} \tag{6-29}$$

Since the electric field can be written as the gradient of the electric potential, or

$$\vec{E} = -\nabla\varphi, \tag{6-30}$$

Equation 6-29 becomes

$$F_b = -\frac{\varepsilon_0}{\lambda_D^2} \varphi \nabla \varphi \qquad (6\text{-}31)$$

Gauss's law relates the divergence of the electric field to the charge distribution:

$$\nabla \cdot \vec{E} = \frac{\rho_c}{\varepsilon_0} \qquad (6\text{-}32)$$

Inserting (6-29) and (6-30) into (6-32) then yields the governing equation for the electric potential:

$$\nabla^2 \varphi = \frac{\varphi}{\lambda_D^2} \qquad (6\text{-}33)$$

Equation (6-33) is Poisson's equation for the electric potential, and is solved numerically in the two-dimensional domain shown in Figure 42.
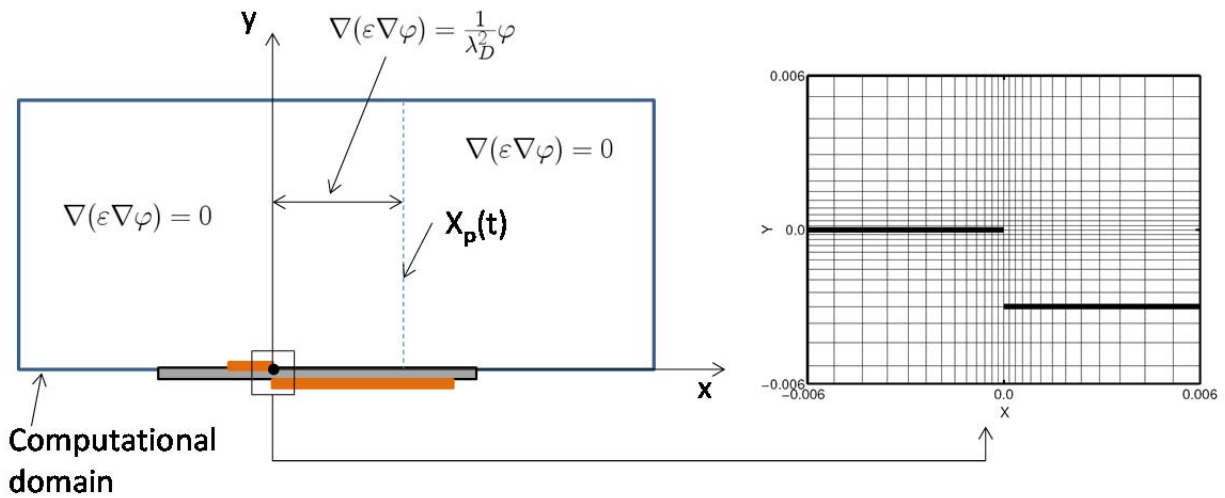
Figure 42. Computational domain for the force calculation. *The graphic on the left shows the computational domain for the force calculation, with the three distinct regions and their governing equations. The graphic on the right shows a blow up of the grid used for numerical solution. The grid is designed to cluster nodes in the plasma region.*

Note that the charge density is assumed to be zero everywhere except in the region directly above the surface where the plasma forms. Poisson's equation only applies in that region, whereas the Laplace equation applies in the remaining regions. The lateral extent of the plasma is given by x_p(t). The following boundary conditions apply:

$$\varphi = V_{app}(t) \text{ on the exposed electrode}$$
$$\varphi = V_n(t) \text{ on the dielectric where the plasma forms}$$
$$\varphi = 0 \text{ on all other boundaries}$$

The computational domain will in general be curvilinear with non-uniform spacing in the physical *x-y* coordinate system. For that reason, we write the Poisson and Laplace equations in a general $\xi-\eta$ coordinate system. The Poisson equation then becomes:

Plasma Flow Control for Wind Turbines – Final Report Navatek, Ltd.

NAVATEK TR--2013/2

$$J^2\left(a\varphi_{\xi\xi} - 2b\varphi_{\xi\eta} + c\varphi_{\eta\eta} + d\varphi_\eta + e\varphi_\xi\right) = \frac{\varphi}{\lambda_D^2} \tag{6-34}$$

where

$$J = \frac{1}{x_\xi y_\eta - x_\eta y_\xi} \tag{6-35}$$

and

$$a = x_\eta^2 + y_\eta^2 \tag{6-36}$$

$$b = x_\xi x_\eta + y_\xi y_\eta \tag{6-37}$$

$$c = x_\xi^2 + y_\xi^2 \tag{6-38}$$

$$d = J(\alpha y_\xi - \beta x_\xi) \tag{6-39}$$

$$e = J(\beta x_\eta - \alpha y_\eta) \tag{6-40}$$

and

$$\alpha = ax_{\xi\xi} - 2bx_{\xi\eta} + cx_{\eta\eta} \tag{6-41}$$

$$\beta = ay_{\xi\xi} - 2by_{\xi\eta} + cy_{\eta\eta} \tag{6-42}$$

We use the following finite difference approximations of the derivatives, which assume uniform spacing in ξ,η with Δξ=Δη=1:

$$\varphi_{\xi\xi} = \varphi_{i+1,j} - 2\varphi_{i,j} + \varphi_{i-1,j} \tag{6-43}$$

$$\varphi_{\xi\eta} = \frac{\varphi_{i+1,j+1} - \varphi_{i-1,j+1} - \varphi_{i+1,j-1} + \varphi_{i-1,j-1}}{4} \tag{6-44}$$

$$\varphi_\xi = \frac{\varphi_{i+1,j} - \varphi_{i-1,j}}{2} \tag{6-45}$$

$$\varphi_\eta = \frac{\varphi_{i,j+1} - \varphi_{i,j-1}}{2} \tag{6-46}$$

Similar expressions are used to define the derivatives of x and y with respect to ξ and η.

Inserting (6-43)-(6-46) in (6-34) and rearranging terms then yields

$$-\varphi_{i,j-1}\left[c_{ij} - \frac{d_{ij}}{2}\right] + \varphi_{i,j}\left[\frac{1}{J^2\lambda_D^2} + 2(a_{ij} + c_{ij})\right] - \varphi_{i,j+1}\left[c_{ij} + \frac{d_{ij}}{2}\right] = R_{ij} \tag{6-47}$$

where

$$R_{ij} = a_{ij}(\varphi_{i+1,j} + \varphi_{i-1,j}) - \frac{b_{ij}}{2}(\varphi_{i+1,j+1} - \varphi_{i-1,j+1} - \varphi_{i+1,j-1} + \varphi_{i-1,j-1}) + \frac{e_{ij}}{2}(\varphi_{i+1,j} - \varphi_{i-1,j})$$

(6-48)

The electric potential on the right-hand-side of equation (6-47), which is defined by (6-48), are taken to be known so that equation (6-47) forms a linear system of equations $[A][\varphi] = [R]$ where $[A]$ is a tridiagonal matrix. Equation (6-47) can be solved using, for example, the Thomas algorithm for tridiagonal matrices.

For regions where Laplace's equation governs the potential, equation (6-47) is replaced by (6-49):

$$-\varphi_{i,j-1}\left[c_{ij} - \frac{d_{ij}}{2}\right] + 2\varphi_{i,j}[a_{ij} + c_{ij}] - \varphi_{i,j+1}\left[c_{ij} + \frac{d_{ij}}{2}\right] = R_{ij} \qquad (6\text{-}49)$$

where R_{ij} is defined by equation (6-48).

Once the electric potentials are known, the electric field strength can be determined through a reverse transformation:

$$E_x = -\varphi_x = -(\xi_x\varphi_\xi + \eta_x\varphi_\eta) \qquad (6\text{-}50)$$

$$E_y = -\varphi_y = -(\xi_y\varphi_\xi + \eta_y\varphi_\eta) \qquad (6\text{-}51)$$

where

$$\xi_x = Jy_\eta \qquad (6\text{-}52)$$

$$\xi_y = -Jx_\eta \qquad (6\text{-}53)$$

$$\eta_x = -Jy_\xi \qquad (6\text{-}54)$$

$$\eta_y = Jx_\xi \qquad (6\text{-}55)$$

Inserting (6-50) and (6-51) in (6-29) yields the following expression for components of the body force:

$$F_{b_x} = \frac{\varepsilon_0 J}{\lambda_D^2}[y_\eta\varphi_\xi - y_\xi\varphi_\eta] \qquad (6\text{-}56)$$

$$F_{b_y} = \frac{\varepsilon_0 J}{\lambda_D^2}[x_\xi\varphi_\eta - x_\eta\varphi_\xi] \qquad (6\text{-}57)$$

Computation of the force distribution now is reduced to solving Poisson's equation numerically with time varying voltage on the surface of the actuator as a boundary condition. The numerical solution is found using finite difference representation of the second derivatives of the potential. The approach, which uses Gauss-Seidel iterations and successive under-relaxation by lines,

Plasma Flow Control for Wind Turbines – Final Report　　　　Navatek, Ltd.

NAVATEK TR--2013/2

requires an initial guess of the potential throughout the domain. To validate the code, we solved Laplace's equation numerically in a rectangular domain with Dirichlet boundary conditions on all four sides (see Figure Figure 43). The problem is solved analytically using separation of variables. The analytic solution for the potential, shown below, involves an infinite series summation that converges rapidly with number of terms in the series.

$$\varphi(x,y) = \frac{4}{\pi} \sum_{n\,odd}^{\infty} \frac{sinh\left[n\pi\frac{b-y}{a}\right]sin\left[n\pi\frac{x}{a}\right]}{n\,sinh\frac{n\pi b}{a}}$$

Figure 44 shows the analytic solution (summed over the first 80 terms in the series) and the numerical solution for the potential at $x=0$, $0<y<b$ for $b=1$.
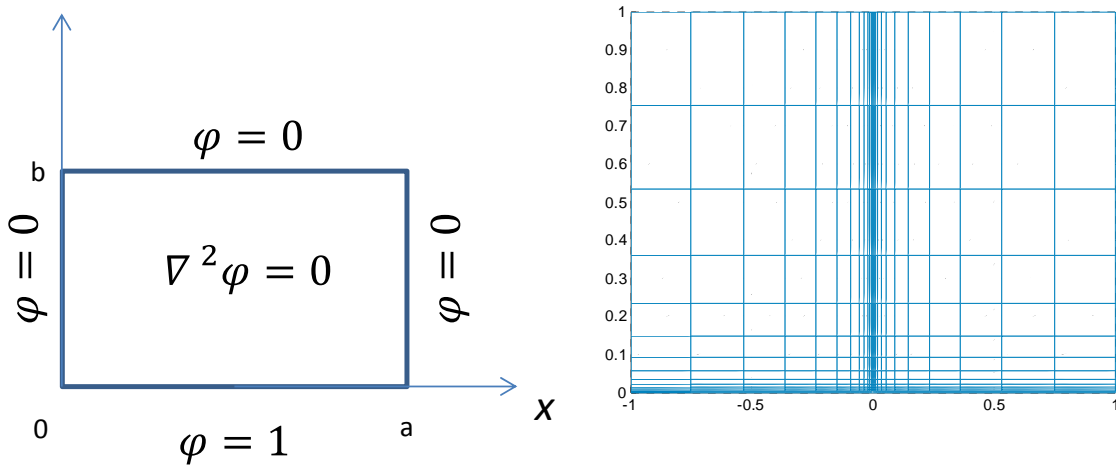
Figure 43. Verification of the force-calculation code: domain and grid. *The graphic on the left shows the domain of the test problem, which admits an analytic solution. The numerical grid is shown on the right.*
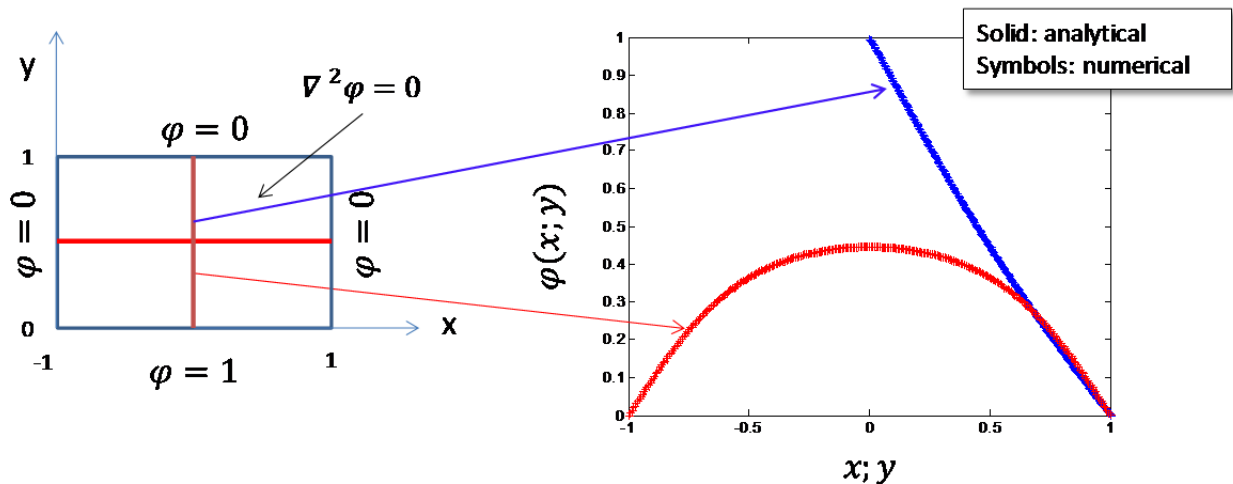
Figure 44. Verification of the force-calculation code: results. *The graphic on the left shows the vertical and horizontal traces where the results are interrogated. The plot on the right compares the numerical and analytical solutions along those traces.*

It should be noted that the numerical solution does not converge (with decreased mesh size) to the analytic solution when the initial guess is zero throughout the domain. Only when the potential was initialized with a nonzero potential did we achieve numerical convergence. This suggests that the discretized governing equation admits a trivial solution in which the potential at every node is zero, except at the boundary. This behavior is shown in Figure 45.
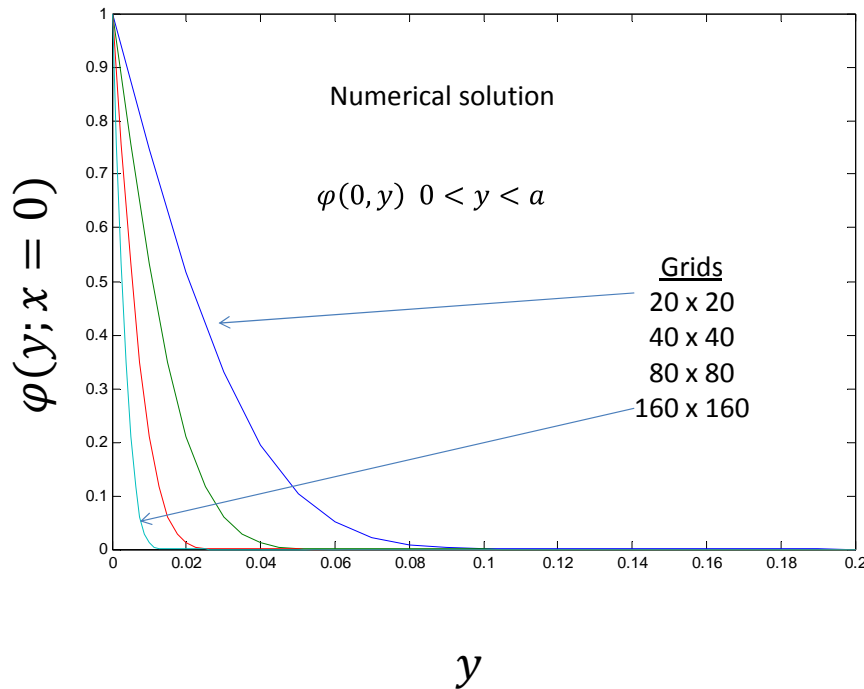
Figure 45. Demonstration of a trivial solution. *Interestingly, this convergence study demonstrates that the discretized equations admit a trivial non-physical solution.*

We turn next to computation of the time-varying surface voltage. In Corke's lumped element model, the actuator is represented by a circuit consisting of a set of parallel capacitors whose capacitance is related to the material properties of the dielectric material and the capacitance of air. An illustrative circuit diagram, taken from (Corke, Enloe, & Wilkinson, 2010), is shown in Figure 46.
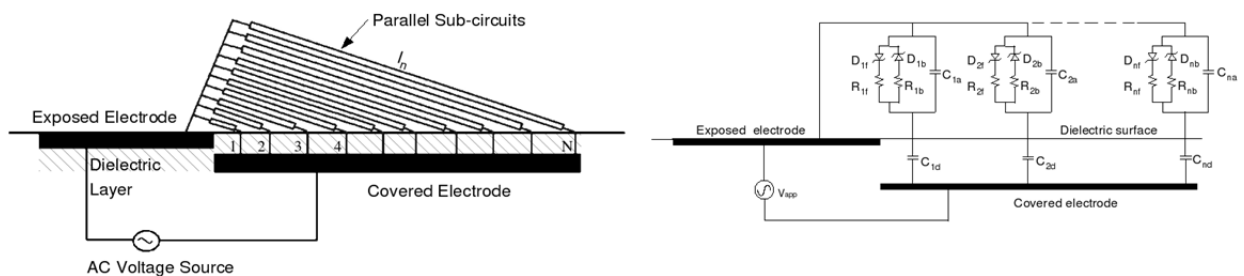
Figure 46. Lumped element model of a plasma actuator. *These graphics show schematics of the lumped element actuator model, from* (**Corke, Enloe, & Wilkinson, 2010**).

The capacitance of each air-capacitor, C_{n_a}, is given by the expression

$$C_{n_a} = \frac{\varepsilon_0 \varepsilon_a A_n}{l_n} \tag{6-58}$$

where ε_0 is the permittivity of free space ($\varepsilon_0 = 8.854 \times 10^{-12}$ amp-s^4/kg-m^3), ε_a is the dielectric coefficient of air, A_n is the cross-sectional area of the air capacitor, and l_n is the distance from the edge of the exposed electrode and the nth solution point on the dielectric surface. Similarly, each dielectric capacitance is determined as follows:

$$C_{n_d} = \frac{\varepsilon_0 \varepsilon_d A_d}{l_d} \tag{6-59}$$

where ε_d is the dielectric coefficient of the dielectric material used in the actuator, A_n is the cross-sectional area of the dielectric capacitor and l_d is the thickness of the dielectric material.

The resistance of each sub-circuit is defined by the following expression:

$$R_n = \frac{\rho_a l_n}{A_n} \tag{6-60}$$

where ρ_a is the resistivity of air. The resistivity is assumed to differ between the two half-cycles. R_{nf} is used to denote the resistance for the forward discharge, while R_{nb} is used for the backwards discharge. The Zener diodes, D_{n_f} and D_{n_b}, are configured to act as binary devices, permitting current to flow in one direction only. In this way, the circuit selects between the forward and backward discharge resistances.

The voltage-current relation for capacitors results in the following expression governing the time-varying voltage on the surface of the dielectric:

$$\frac{dV_n}{dt} = \frac{dV_{app}}{dt} \left[\frac{C_{a_n}}{C_{a_n} + C_{d_n}} \right] + k_n \frac{I_p}{C_{a_n} + C_{d_n}} \tag{6-61}$$

where $k_n = 1$ if the plasma is ignited in the circuit and zero otherwise. The plasma current, I_p, is given by

$$I_p(t) = \frac{V_{app}(t) - V_n(t)}{R_n}. \tag{6-62}$$

Equation 6-61 can solved numerically using a standard ODE solver such as a Runge-Kutta algorithm. Figure 47 shows voltage and current time traces for a sample calculation. Figure 48 shows sample force calculations normalized by their maximum values.
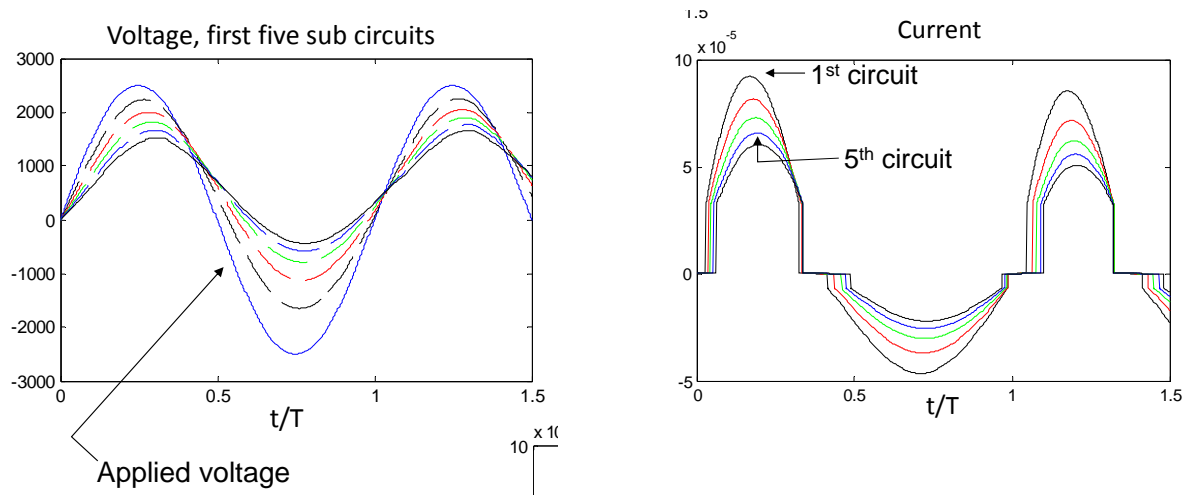
Figure 47. Sample voltage and current computed by the lumped element actuator model. *The plot on the left shows the applied voltage and the computed voltage at the first five nodes in the lumped element model actuator solution. The plot on the right shows the corresponding current computed at the first five nodes. The current shows peaks where the plasma ignites.*
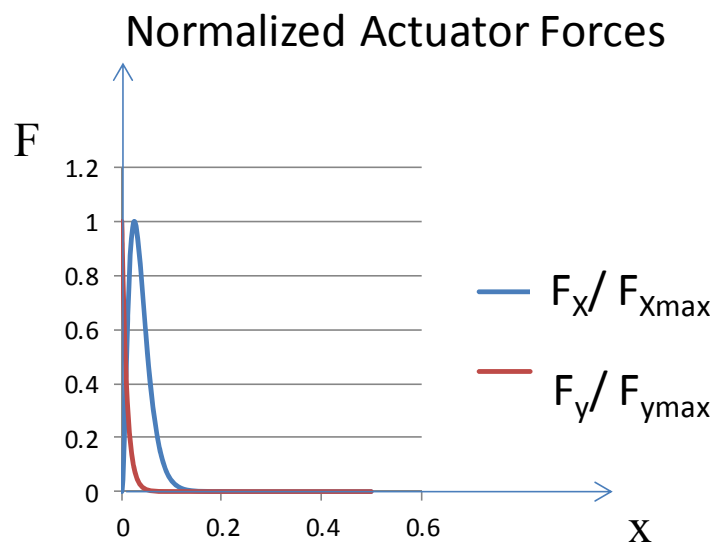
Figure 48. Sample actuator forces computed using the lumped element method. *This plot shows forces along the actuator, computed using the lumped element method. These distributed forces can be used as input to FINE™ Marine through the UDF.*

User Defined Function (Revisited)

The external body force distribution computed by the methods described above can then be used as input to the fluid flow solution via the User Defined Function. In formulating the problem, Numeca has been careful to formulate the governing equations to satisfy mass and momentum conservation with the addition of the external force.

Once we put the pieces together, we began to make predictions of airfoil lift and drag with and without actuation. However, we were unable to obtain converged solutions for the forces on the airfoil when we used the UDF (unlike the flow in a box, for which we demonstrated mesh-

independence). We spent a lot of time working with Numeca to resolve the issue, but eventually we decided to abandon the topic to focus on the field demonstration. Based on our latest information, we have concluded that the problem lies with the fact that FINE™ Marine is not ideally suited for unbounded, single-phase flows.

6.3   Conclusions

In this project, we developed and tested a low-order model for predicting the performance of wind turbines using airfoil lift and drag look-up tables. Those look-up tables could come from experiment or computation, and the computational results could be low-Reynolds number XFOIL calculations (with a semi-empirical correction to account for the actuator) or 2D RANS calculations with the actuator accounted for through the UDF. Our intention was to use the 2D RANS tool to predict the lift and drag polars with and without actuation, but we were unable to verify the RANS solution with actuation. Our recommendation for future work in this area is to switch to the FINE™ Turbo tool, which is better suited for this type of calculation. In the meantime, we will base our performance predictions on lift and drag computed by XFOIL, with semi-empirical corrections derived from the experimentally determined lift enhancements due to actuation.

7.   Estimates of Increased Power Generation for the VP20

7.1   Baseline Calculations

We begin by applying the blade element method described in Section 6.1 to evaluate the baseline performance of the Renewegy VP20 turbine. The VP20 is a three-bladed, upwind, variable pitch turbine manufactured in Appleton, Wisconsin. The nameplate power rating of the VP20 is 20 kW, the cut-in speed is 3.5 m/s and the rated wind speed is 16 m/s. The rotor diameter is 9.5 m. Renewegy provided a detailed description of the blade geometry, which we used to build tables of lift and drag coefficients for input to the blade element code. The lift and drag tables were computed using XFOIL.

Figure 49 shows sample XFOIL results for the seven-tenths radius section of the VP20 (e.g., the 2D blade section located at a radial position that is 70% of the full blade radius) at two angles of attack. The two plots in the figure show the pressure distribution from both inviscid (dashed line) and viscous (solid line) solutions at an angle of attack of 10° (left) and 14° (right). The boundary layer displacement thickness is shown superimposed on the section shape below the pressure distribution.
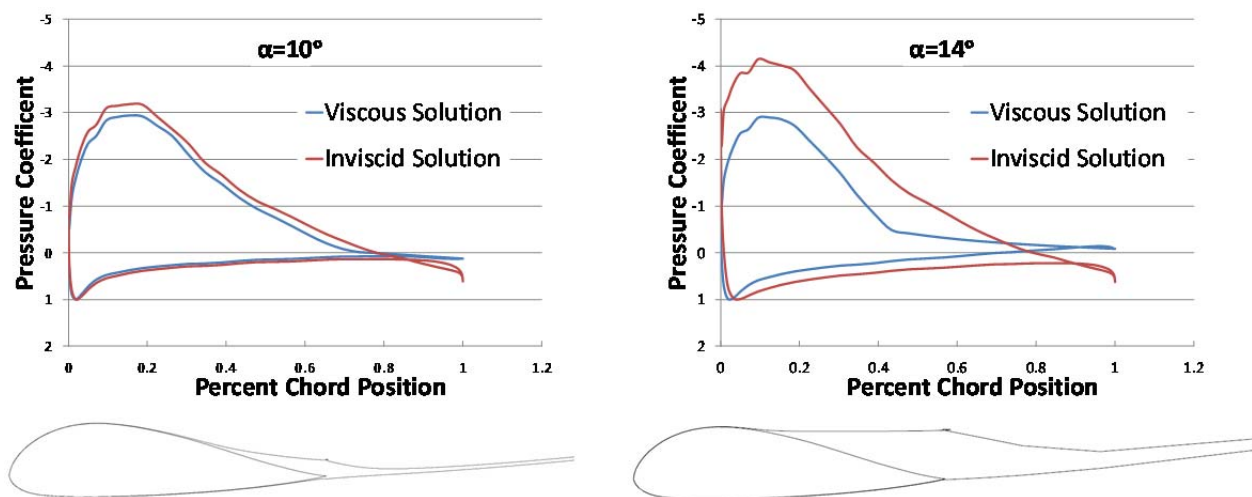
Figure 49. Sample XFOIL calculations. *These two graphics show the pressure distribution on the surface of an airfoil at two angles of attack. The airfoil is the seven-tenths radius section of the VP20.*

XFOIL computes coefficients of lift, drag and moment about the quarter-chord. Figure 50 shows plots of lift and drag coefficients as a function of angle of attack and radial position. These lift and drag coefficients are then used to compute the shaft power as a function of wind speed and blade rotation rate. The VP20 is designed to rotate at about 100 RPM near its rated wind speed.

Plasma Flow Control for Wind Turbines – Final Report   Navatek, Ltd.

NAVATEK TR--2013/2
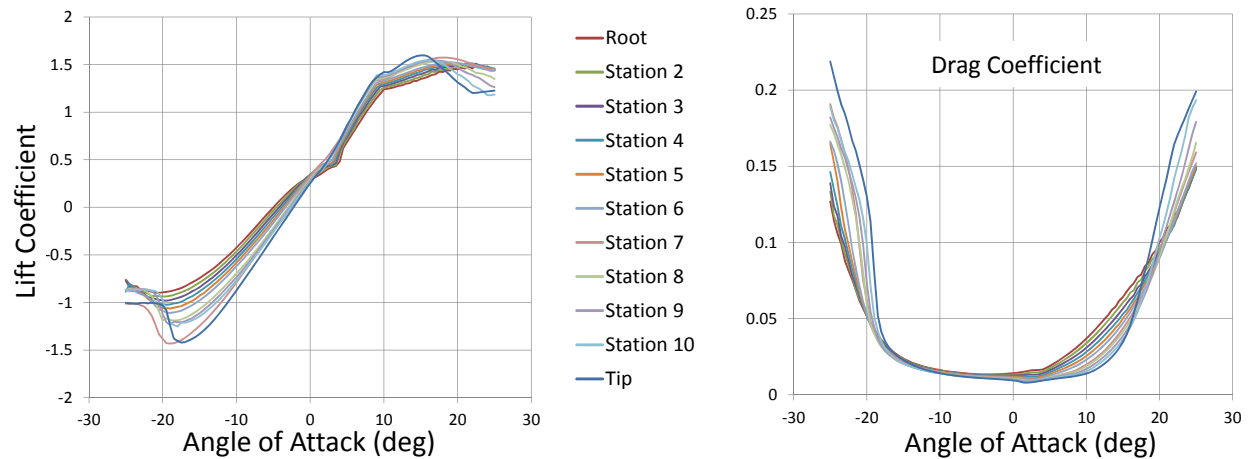
Figure 50. XFOIL lift and drag predictions for the VP20. *These plots show lift coefficient (left) and drag coefficient (right) as a function of angle of attack and radial position for the VP20.*

Figure 51 shows the power coefficient, C_P, as a function of the inverse of the tip speed ratio, λ. The power coefficient is defined as the shaft horsepower, P_S (the product of shaft torque and blade rotation rate) normalized by the idealized amount of power available in the wind:

$$C_P = \frac{P_S}{\frac{1}{2}\rho V^3 A} \tag{7-1}$$

Where ρ is the density of air, V is the wind speed and A is the swept area of the rotor. The tip speed ratio is defined as

$$\lambda = \frac{\omega R}{V} \tag{7-2}$$

Where ω is the rotation rate and R is the rotor radius. The power coefficient is often plotted as a function of the inverse of λ because that quantity increases in proportion to wind speed.
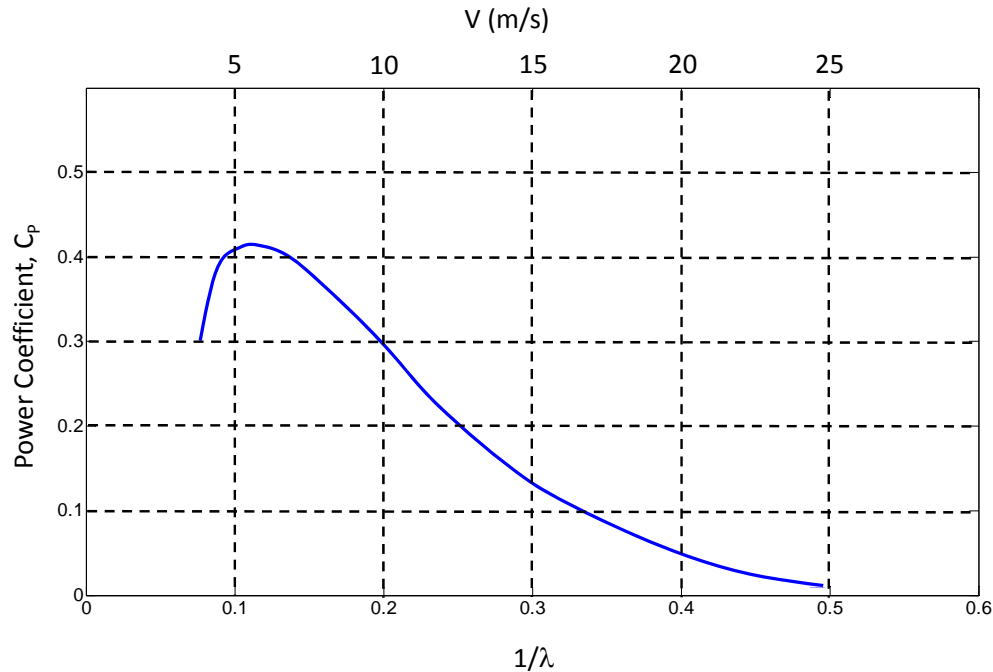
Figure 51. VP20 performance prediction: baseline. *This plot shows the baseline (e.g., without plasma flow control) VP20 power coefficient as a function of inverse tip speed ratio (or wind speed) at 100 RPM.*

7.2   Plasma-Enhanced Power Generation

We applied the lift augmentation factors displayed in Figure 26 to the 2D lift curves computed by XFOIL and used the modified lift to compute the VP20 power coefficient as a function of wind speed. In so doing, we computed the optimum turbine rotational speed and pitch angle at each wind speed using a modified Nelder-Mead optimization algorithm. The results, plotted alongside the baseline power curve, are shown in Figure 52. To get a sense of importance of the variation seen in the augmentation factors measured at the four different tunnel speeds, we computed the power coefficient using four different augmentation factors (all of them functions of sectional angle of attack). Details of the computational tools used during this program are provided in Section 6.
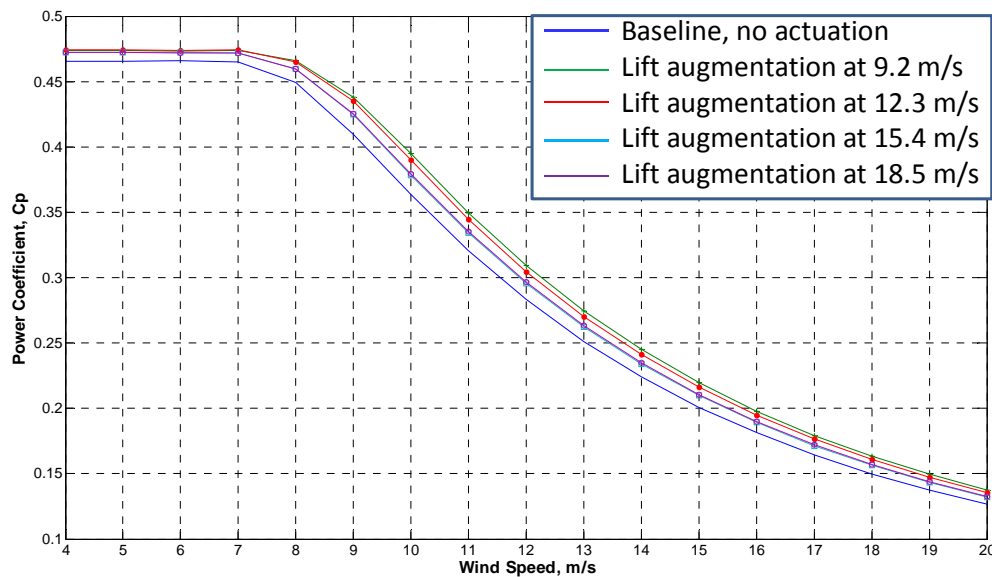
Figure 52. VP20 performance prediction: with actuation. *This plot shows turbine power coefficient for the VP20 as a function of wind speed, including the effects of lift augmentation measured in the wind tunnel at various tunnel speeds. Unlike the results shown in Figure 51, the optimum pitch angle is determined numerically at each wind speed.*

7.3   Optimization

Given approximate limitations on the lift enhancement capabilities of thin plasma actuators applied to the VP20 turbine blades derived from our wind tunnel data, it's of interest to determine the optimum performance attainable for that turbine. To that end, a tool for examining the optimal distribution of plasma actuators on a wind turbine was developed. This tool uses the blade element method described in Section 6.1 to compute the power produced by a given turbine using specified sectional lift and drag curves. It is assumed that the plasma actuator can affect the lift curve slope at high angle of attack and can affect the final stall angle of a given section. The lift is not affected at low angles of attack. The lift curve is affected by multiplying the existing slope by a multiplier similar to that seen in laboratory testing. The stall angle is increased by an amount similar to that seen in wind tunnel testing. The pitch of the blade is fixed. The multiplier on the lift curve is implemented using a B-spline. This ensures a smooth curve across the entire span of the blade. Points are interpolated along the spline and used in the blade element model.

To determine the required number of spline points, a simple check was performed. A wind turbine was "built" with linear lift (slope=2π) and a fixed stall angle. The starting point for the curve could be varied using a spline identical to the one described above. Particle swarm optimization (a nonlinear, stochastic optimization technique for NP complete problems) was used to compute the optimal solution based on maximized power coefficient. The results for the spline using seven points and nine points are shown as Figure 53. There are slight differences in the spline (shown as CL_0) but the overall power coefficient is within 1%.
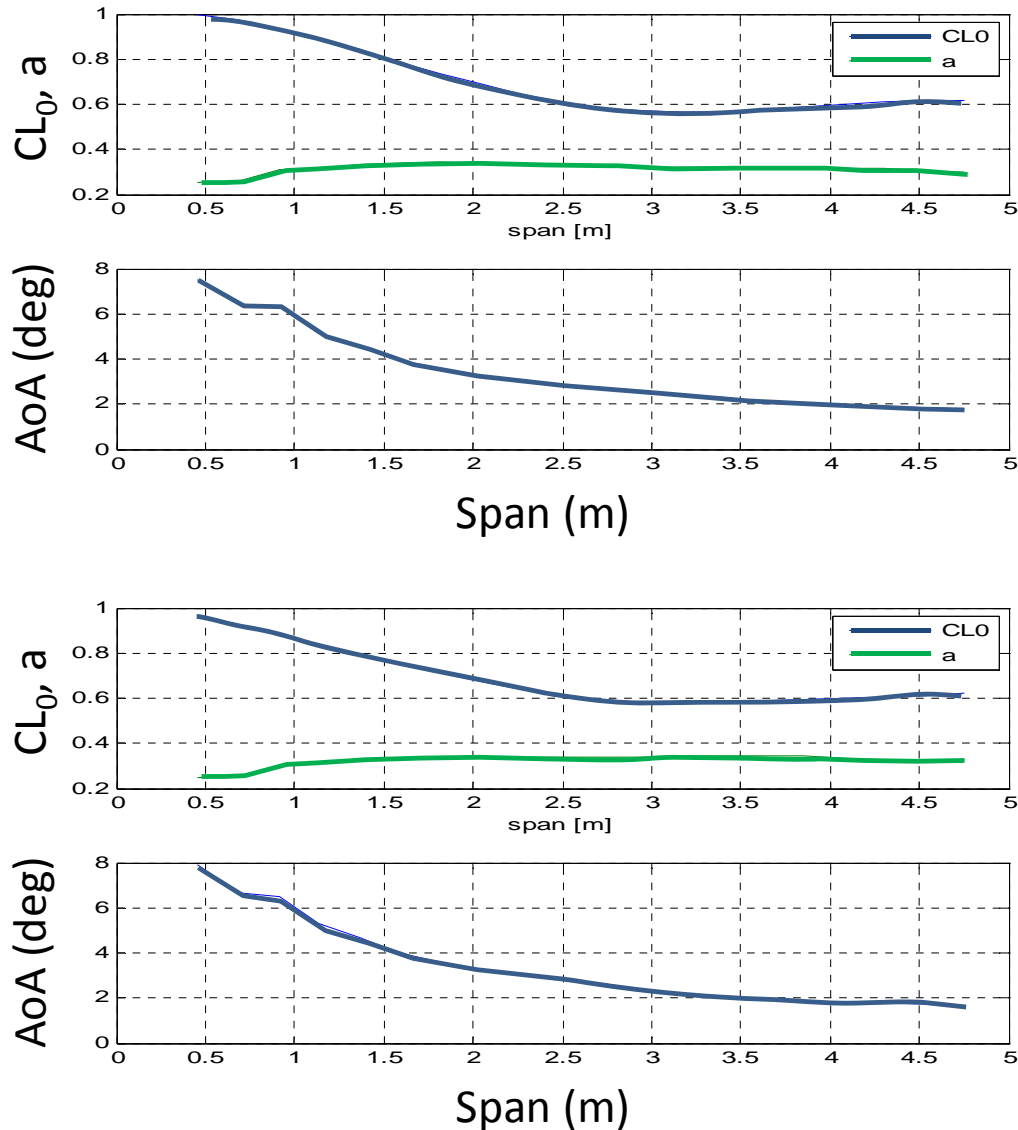
Figure 53. Optimization: effect of number of spline points. *These plots show the results of a simplified optimization with seven spline points (bottom) and nine spline points (top).*

A series of optimizations were performed at four, six, eight, and ten meter per second wind speeds using the simplified turbine. The simplified turbine is the same model used for the convergence check shown in Figure 53. In this model, the lift is assumed to be linear to stall with a slope of 2π. The lift at zero angle of attack (CL_0) can be varied across the span of the blade. The results are shown as Figure 54. As the wind speed increases, the starting point for the lift curve increases towards the tip of the blade. The induction coefficient (denoted by the letter *a*) tends towards a flat curve over the entire span of the blade. The angle of attack of the blade goes up at higher wind speeds until stall occurs. These trends are expected. At high speeds, the blade can have high loading from root to tip without risk of stall. The induction factor is going to the Betz limit of 1/3 at the high wind speeds. Even at low wind speeds, the optimization is driving the induction factor to that optimal level. This indicates that the optimization is working.
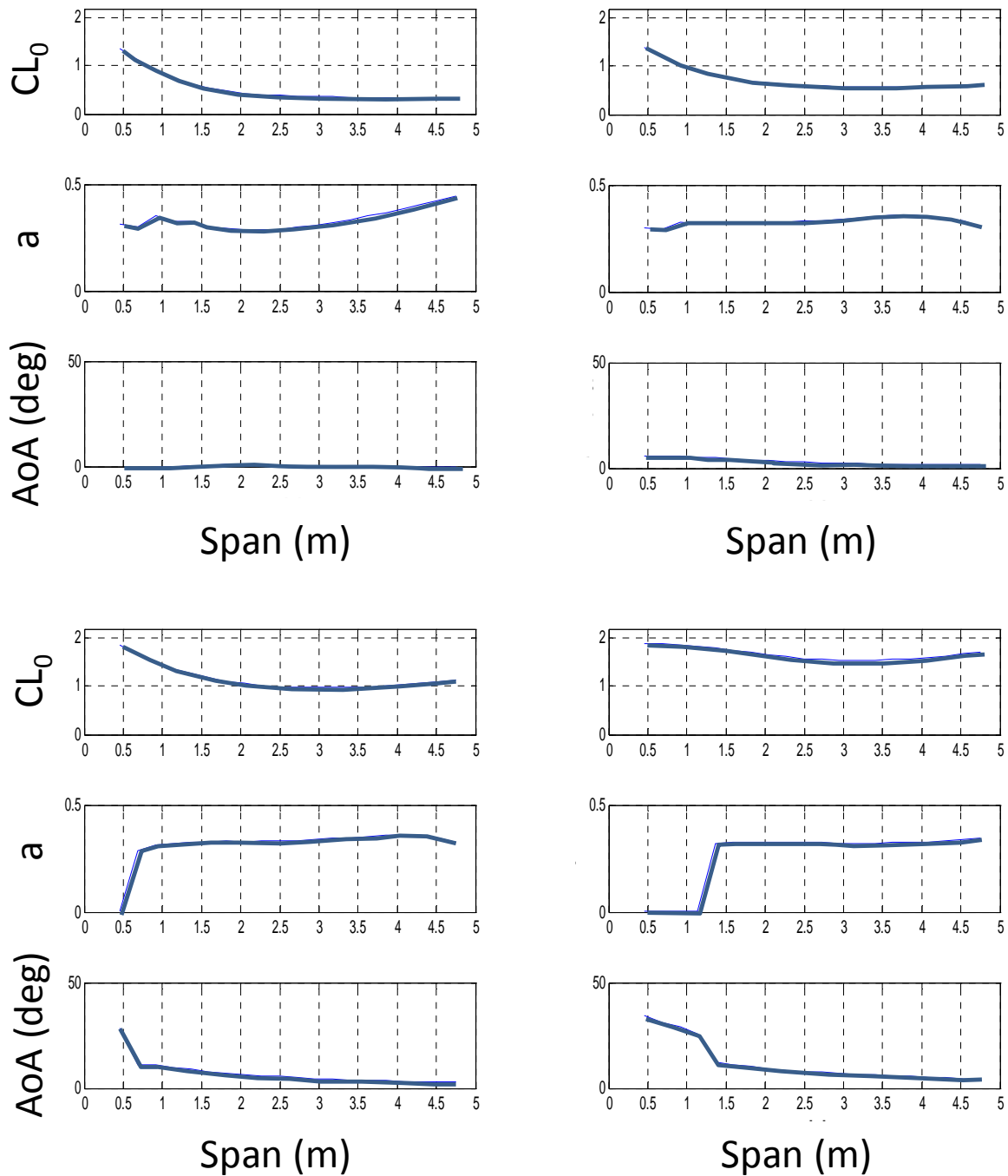
Figure 54. Optimization: preliminary verification. *These plots show a series of optimizations for a simplified wind turbine (using linear lift slope) at varying wind speeds (right to left, top to bottom: 4, 6, 8, 10 m/s).*

With the process verified, it can now be used to look at more realistic blade characterizations. In the case of the Renewegy VP20 (the test platform for the plasma actuator), the lift and drag curves are as shown in Figure 55. Eleven stations along the span are shown. An assumed stall of 20 degrees was used. The curves were computed using XFOIL.
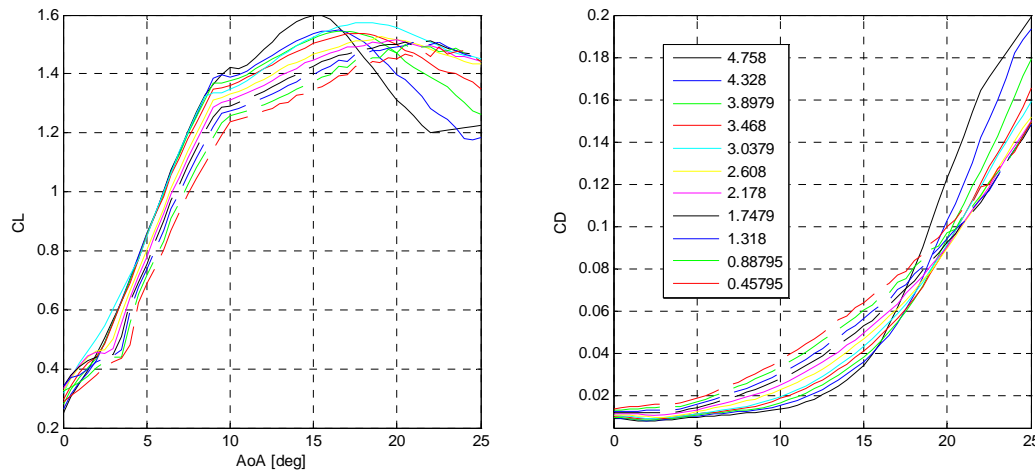
Figure 55. XFOIL computed lift and drag. *These plots show lift (left) and drag (right) coefficients as a function of angle of attack and radial position for the VP20 section, computed by XFOIL.*

A plot of a sample test using plasma actuation in Navatek's wind tunnel is shown as Figure 56. A similar shape to the curves shown in Figure 55 is seen. It is clear that plasma actuation, in this test, only affects the lift curve above the point where the slope is no longer linear. Therefore, for the realistic optimizations, it will be assumed that the lift curves will be affected from 10 degrees until stall and will only be able to increase the lift slope above 10 degrees by 1.5 times the original slope. As with the simplified process, a spline is used to model the multiplier on lift curve above 10 degrees.
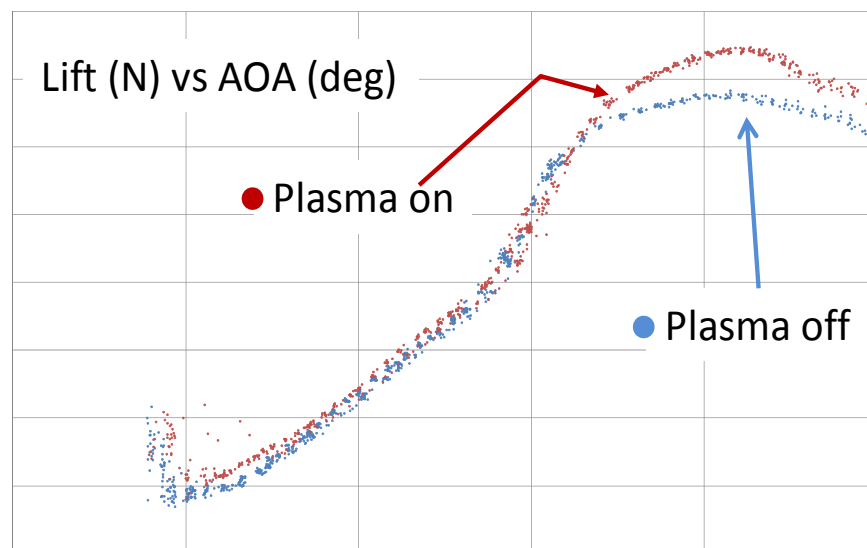
Figure 56. Measured lift with and without plasma. *This plot shows the qualitative nature of the plasma-enhanced lift, as measured in a wind tunnel testing of the VP20 section with and without plasma actuation.*

Preliminary results for an optimization are shown as Figure 57. These results are shown for a 10 m/s wind speed. On the left the turbine without any plasma actuation is shown. The stall angle was assumed to be 25 degrees. The RPM is set using the VP20 generator profile. The

pitch of the blades is set using the VP20 control algorithm. As can be seen, from a span of 2.2 meters to the root, the blade stalls. This leads to a power coefficient of 0.31. When plasma is turned on, the stall point is moved to 1.1 meters from the root. Also, the lift curve over most of the span is increased to allow for more wind capture. The stall point is assumed to be five degrees higher when plasma actuation is used. The blade pitch is an input variable for the optimization and the resulting pitch is much lower than the design pitch from the manufacturer at 3.8 degrees versus 6.9 degrees. The resulting RPM of the generator is also higher at 108 RPM versus 107 RPM. The maximum RPM for the generator is 110 RPM. The optimization shows that the blade should have lower lift slope at the tip. It is not clear why this is occurring as there is no risk of stall at the tip of the blade; the angle of attack is 10 degrees at the tip. This approach will be further investigated in the subsequent phase of the development program.

CP0=0.31, CP=0.38
Pitch = 6.9 deg
RPM = 106.8

CP0=0.31, CP=0.38
Pitch = 3.8 deg
RPM = 108.4
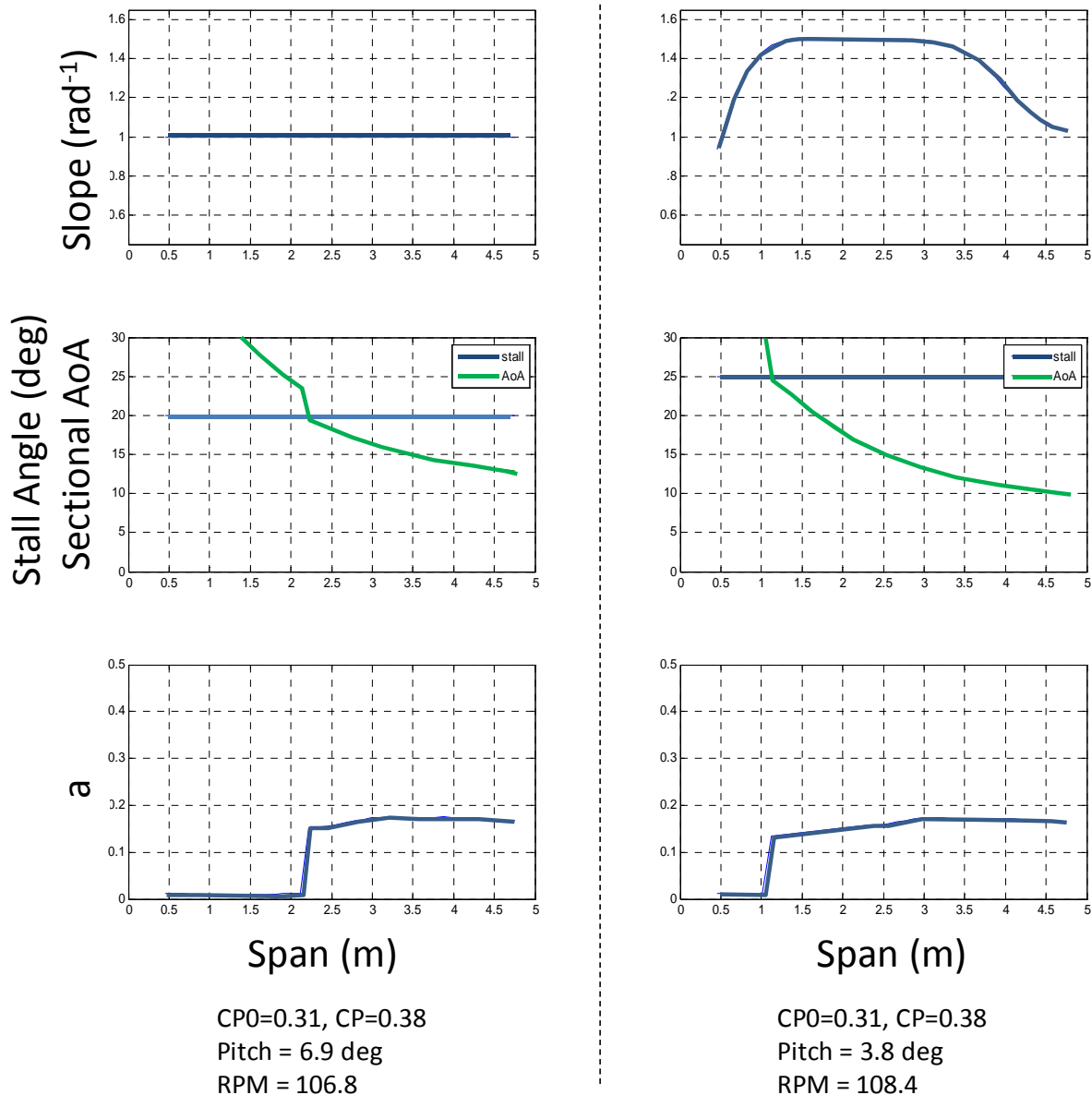
Figure 57. Preliminary optimization for VP20 turbine. *These plots show results of optimization with plasma actuation. On the left are results without plasma-enhancement of the lift, and on the right are results with plasma-enhancement of the lift.*

7.4   Conclusions

Using the lift and drag measurements presented here, we conclude that actuators constructed of 20-mil thick Cirlex operated at 6.5 kV could increase the power generated by the VP20 by four to ten percent, depending on wind speed. Increasing the power generated by a wind turbine through plasma flow control appears to be limited by the maximum voltage that can be applied to the actuator. While thicker actuators produce more thrust (since they can achieve higher peak voltages), they can degrade the aerodynamic performance of the wing by inducing separation at the actuator leading edge. Even if the downstream actuation causes the flow to re-attach, in such situations the overall blade performance is likely to be at best unimproved relative to the baseline bare blade. For that reason, we believe that the 20 mil Cirlex may be close to optimum for this blade. On the other hand, if thicker actuators could be embedded in the surface of the blade, so that they are mounted flush to the original blade surface, then significant improvements could be made to the power generation.

In future work, the optimization process will be further explored by performing a design of experiments at varying wind speeds to determine the overall trends of the design space. This will lead to a detailed design process that will result in an optimal spanwise distribution of plasma actuators and a pitch profile to replace the current algorithm.

8.   Ozone and NO_x Measurements

8.1   Motivation

This section describes the results of a set of experiments in which we measured the rate at which ozone and NO_x gases are produced by a plasma actuator. Atmospheric plasma is known to generate ozone (O_3), nitric oxide (NO), nitrogen dioxide (NO_2) and nitrous oxide (N_2O). Ozone is a precursor to smog and is toxic to humans. NO_X (a collective term encompassing NO and NO_2) are precursors to acid rain, and nitrous oxide is a greenhouse gas. If the plasma actuators that are to be used for flow control on wind turbines produce these gases in sufficient quantity, the benefits of improved wind turbine performance and increased electrical power generation might be offset by the negative environmental impacts of these gaseous byproducts. It is therefore important to quantify the rate at which these gases can be expected to be generated in a full scale installation.

8.2   Objective

Our first objective was to quantify the rate at which a plasma actuator of a given length generates ozone (O_3), nitric oxide (NO) and nitrogen dioxide (NO_2). This "source rate," for example, might be expressed in terms of grams of gas produced per-second-per-meter of actuator. Time and budget limitations prohibited measurement of nitrous oxide (N_2O), which would require more complicated and expensive tools then we currently have access to. The second objective was to scale the data to the size of a typical wind turbine implementation, and evaluate the levels with respect to environmental regulations. The third objective was to examine the effects of several variations on plasma actuator design, including serration of the exposed electrodes, varying dielectric thickness and adding a thin layer of catalyst to the surface of the actuator.

8.3   Description of the Experiment

In this experiment, we used two gas analyzers, one for detecting ozone and another for detecting NOx, to quantify the rate at which a plasma actuator of a given length generates the gaseous byproducts. Both devices were rented from American Ecotech, a local RI firm specializing in the design and operation of air pollution monitoring equipment. The company's EC9481B Oxides of Nitrogen Analyzer uses chemiluminescence detection to measure NO, NO_2 and NO_x in the ranges of 0-50 ppb and 0-20 ppm with a published lower detection limit of 0.5 ppb. This analyzer measures the NO_2 concentration, then chemically converts the NO molecules in the sample to NO_2 and then re-measures NO_2 concentration. This latter measurement provides a combined NO_x concentration. The NO concentration is then determined as the difference between the NO_x and NO_2 concentrations. The NO and NO_x measurements are inherently less accurate than the NO_2 measurements, because the conversion of NO to NO_2 is not 100% efficient. The Serinus 10 Ozone analyzer uses non-dispersive ultraviolet (UV) absorption technology to measure O_3 in the range 0-20ppm with a lower detection limit of 0.5 ppb.

Not knowing in advance the concentration of the gaseous byproducts that would be produced by the plasma actuators, we designed a system that would allow us to vary the flow rate past the analyzer probes so that the concentration could be "dialed" up or down over some range. The system consisted of a Plexiglas container (roughly a cube, 17 inches on a side – shown in Figure

58), with a circular inlet (four inches in diameter) and a circular outlet (also four inches in diameter). The plasma actuators were placed inside the container, which also housed electrical terminals connected to the high voltage power supply. The outlet led to a PVC duct, which was connected to an inline centrifugal duct fan (Soler and Palau, model PV-100x) rated at 150 CFM at 0 in wg pressure head.
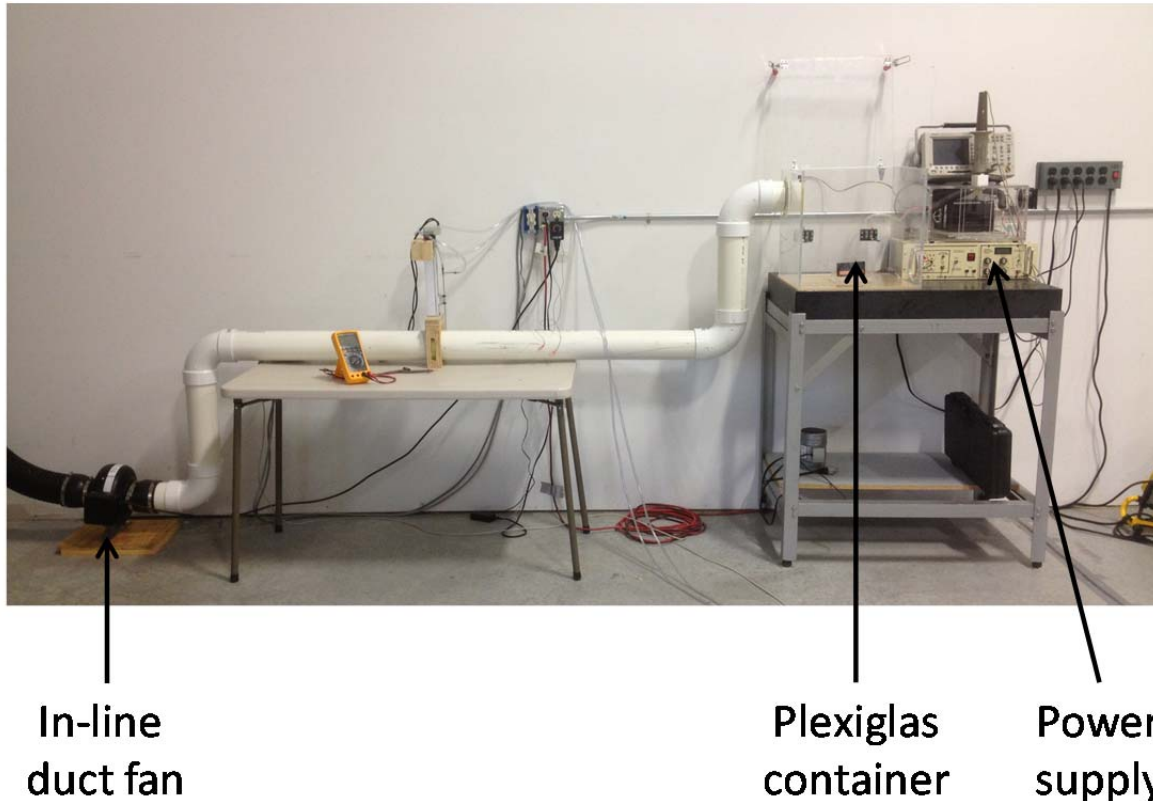
Figure 58. Gas byproduct measurement: apparatus. *This picture shows the apparatus that was built to delivering gaseous byproducts of a plasma actuator past a pair of gas analyzers.*

To measure the flow rate in the PVC duct, we set up a small pitot tube on a linear actuator (Dyadic model SCLL5-010-200AB-NA) to measure axial velocity at points across two diameters (one vertical and one horizontal). The Pitot tube is connected to the same differential pressure transducer (Omega PX653-02D5V) used to measure velocity in the wind tunnel. We repeated the measurements at two axial locations (separated by 12 inches in the axial direction). The apparatus, along with sample velocity profiles, is shown in Figure 59. Numerically integrating the profiles yields a flow rate of 116 CFM. The flow rate measured at the two axial locations agreed to within 0.25%.

Probes from the two analyzers extracted their samples from the airstream in the duct. The two analyzers used a small pump to draw their samples through the machines. Each would draw in a sample of known volume, measure the O_3 or NO_x concentration, and display the result to the screen in units of parts-per-billion by volume (ppb). Each machine was capable of recording the one-minute average of the gas concentration.

Plasma Flow Control for Wind Turbines – Final Report   Navatek, Ltd.

NAVATEK TR--2013/2
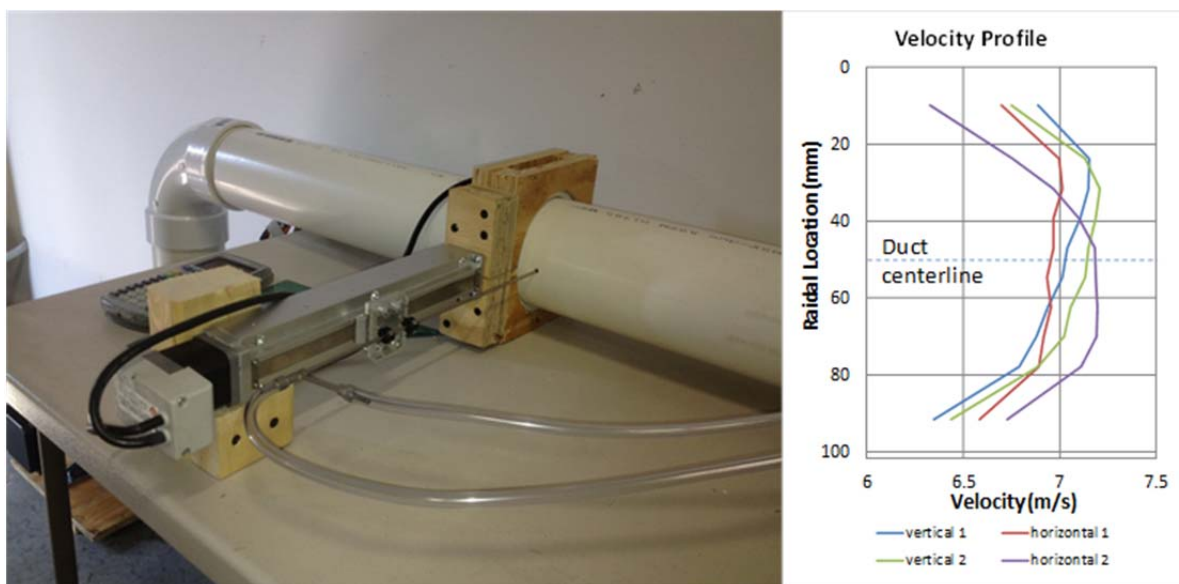
Figure 59. Gas byproduct measurement: close-up view. *This picture shows a close-up view of the Pitot tube and linear actuator apparatus (left) and measured velocity profiles in the duct (right). The velocity profiles are used to accurately determine the flow rate in the duct.*

8.4 Test Actuators

We recorded O_3 and NO_x concentrations for five plasma actuators for varying applied voltage, and one with varying frequency. The first actuator used a 40 mil thick Cirlex dielectric with a "straight" exposed electrode. The second used the same dielectric material, but made use of a serrated exposed electrode (Figure 60). The third actuator used 125 mil thick PTFE, for which we varied both voltage (at a single fixed frequency) and frequency (at a single fixed voltage). The fourth actuator used an alumina ceramic dielectric (25 mils thick), and the fifth was identical to the fourth, but with a thin layer of titania applied to the surface of the dielectric just downstream of the exposed electrode.

Figure 60. Serrated actuator. *This 40-mil thick Cirlex actuator was constructed with a serrated electrode. The serrated electrode provides regions of increased electric field strength, resulting in a measureable increase in thrust. We are interested to know if that increase in thrust comes with a similar increase in gaseous byproducts.*

8.5   Ambient Background Levels

We began by measuring the background levels of O_3 and NO_x to get a sense of the ambient levels and how they varied throughout the day. Figure 61 and Figure 62 show data collected during a two-day period. On the first day (Monday, shown in Figure 61), we were becoming acclimated with the devices and did not annotate the data. The peaks seen in the data are likely due to other activities in the lab, including running the wind tunnel with plasma actuators and opening the bay door. This activity was noted during the second day, and the plot has been annotated with notes describing the activity.

One noteworthy aspect of the data shown in Figure 61 is the fact that the NO concentrations were small and, largely, negative. Since concentrations cannot be negative in this context, this clearly is an indication of the inaccuracy in the measurement of NO and NO_x. As noted above, the device measures NO_2 and derives the concentration of NO by attempting to chemically convert all of the NO molecules in the airstream to NO_2. An estimate of the concentration of NO can then be found by subtracting the (relatively accurate) baseline measurement of NO_2 from the (somewhat less accurately) measured NO_x. The fact that the device generates small (but almost entirely negative) NO concentrations has two possible explanations. First, the manufacturer may be overcorrecting for the less than 100% efficient conversion of NO to NO_2. Second, the conversion process may itself generate additional NO_2 through reactions with the diatomic nitrogen present in the background gas.

For the purpose of this experiment, we note that the magnitude of the NO concentration is always one or two orders of magnitude lower than the NO_2 concentration. For that reason, we will ignore the NO measurement and present only NO_2 (along with ozone) concentrations.

Figure 62 shows the ozone and NO_2 concentrations measured during the second day. These were background ambient measurements, as opposed to experiments aimed at quantifying the gaseous byproduct concentrations, but plasma-related activities were on-going in the lab during that time. A peak in ozone – reaching just over 30 ppb – is visible beginning at roughly 9am and lasting about 2 hours. It was noted that the overhead door was open during that time, indicating that the outside ambient ozone level was likely higher than that inside (with the door closed). A similar peak on Monday (Figure 61, starting at about noon), might have the same explanation, although we weren't taking detailed notes that day. The other peaks show marked increases in ozone and NO_2 when the wind tunnel was being operated (with plasma actuators in use on the test wing).
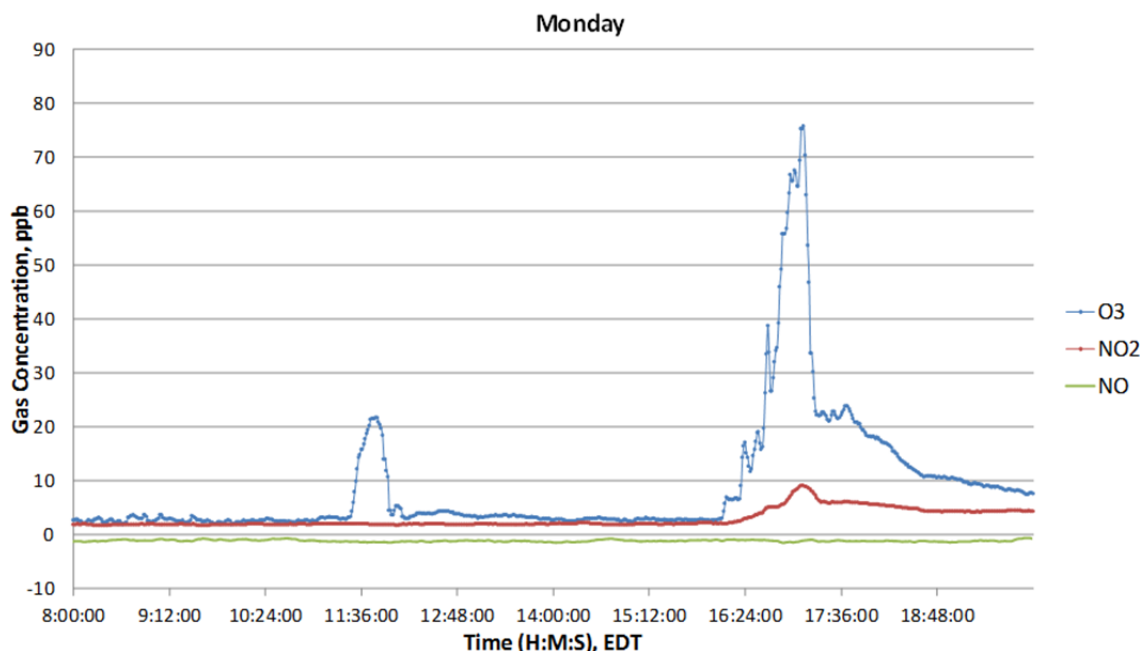
Figure 61. Gaseous byproducts: day one background measurements. *This plot shows ozone, NO and NO₂ concentration measured over an 11 hour period on the first day of measurements.*
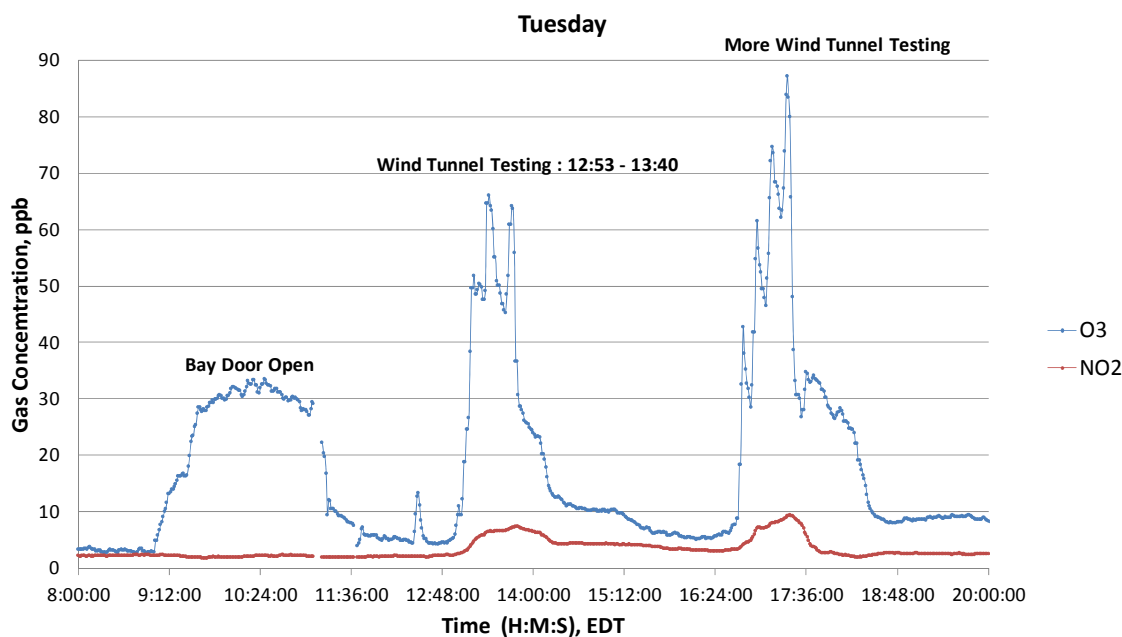
Figure 62. Gaseous byproducts: day two background measurements. *This plot shows ozone and NO₂ concentration measured over a 12 hour period on the second day of measurements.*

8.6   The Gaseous Byproducts of Plasma Actuators

In this section, we describe the experiments aimed at quantifying the amount of ozone and NO₂ produced by plasma actuators. For each actuator, we began by recording a twenty-minute average of the ambient background levels. We then incrementally changed the voltage (or frequency) and recorded one-minute averages for ten consecutive minutes. When we completed

the set of voltages or frequencies we'd intended to measure, we returned the voltage to zero (extinguishing the plasma) and re-measured the 20-minute average of ambient background. For the purpose of calculating the portion of gas concentration that was in excess of background, we treated the background level as the average of that measured in the 20-minute interval just before the experiment began and that measured just after the experiment was completed. All measurements were made with at the maximum flow rate (about 116 cfm). We assume that the rate at which a plasma actuator generates any gaseous byproduct is independent of the flow rate, at least not for the small flow rates characteristic of our experiments. The question of whether or not the rate changes when the actuator is exposed to higher velocities is left for further study.

The first experiment used the 40-mil Cirlex dielectric. For this test we varied the voltage from 0 to 12 kVrms, in 1 kV increments. All experiments were conducted at an A/C frequency of 2 kHz. The test was repeated in three separate trials, separated by one or more days. The raw data for one such trial is plotted in Figure 63. Note that the red curve represents NO_2 only – the concentration of NO was consistently lower by two orders of magnitude (as discussed above). The gas concentrations derived from this data are shown in Table 2. This experiment was repeated in two additional trials.
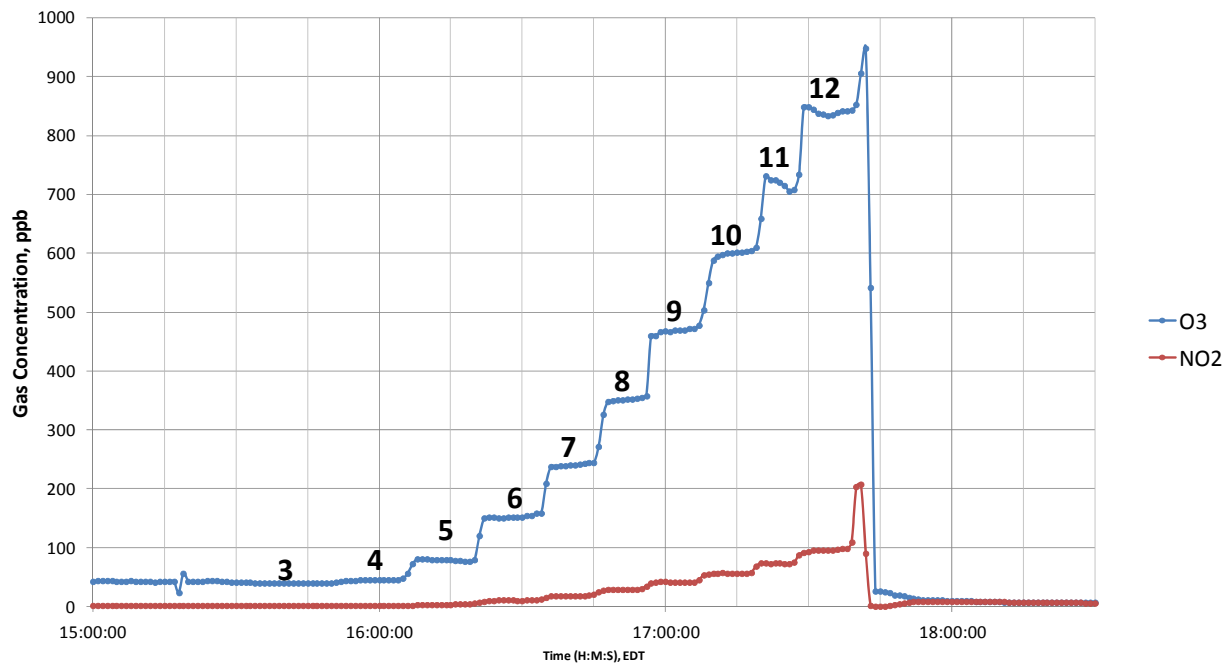
Figure 63. Gaseous byproducts: detailed actuator measurements. *This plot shows ozone and NO_2 concentrations produced by a 40 mil Cirlex actuator. The integers 3 through 12 represent the voltage across the actuator (in kVrms).*

Table 2. O_3 and NO_2 concentration as a function of voltage for a 40 mil Cirlex actuator.

Voltage (kV)	Start time	End time	Avg O_3	Avg $NO2$	Avg O_3 less ambient avg	Avg NO2 less ambient avg
ambient 1	15:00	15:30	42.45	1.32		
3	15:34	15:46	39.91	1.08	10.71	-2.36
4	15:52	16:02	44.33	1.31	15.14	-2.14
5	16:09	16:17	79.06	3.19	49.86	-0.26
6	16:23	16:32	151.83	10.28	122.63	6.83
7	16:36	16:42	239.11	17.82	209.91	14.38
8	16:48	16:53	350.35	28.74	321.15	25.30
9	16:58	17:04	467.08	41.41	437.88	37.97
10	17:11	17:16	599.27	56.25	570.08	52.80
11	17:21	17:25	723.38	72.91	694.18	69.47
12	17:30	17:37	839.84	95.38	810.65	91.94
ambient 2	17:44	18:00	15.94	5.57		

The ideal gas law asserts that

$$PV = nRT \tag{8-1}$$

Where P is the gas pressure (in atm, for example), V is the volume (m^3), n is the number of molecules (moles), R is the gas constant (8.25e-5 atm m^3/mol °K), and T is the gas temperature (°K). If we define the source rate, $\dot{N}$, as the rate (in g/s) at which a gaseous byproduct (e.g., either O_3 or NO_2) is produced in a flow, then Equation (8-1) can be used to show that the concentration, C (in ppb), of gas is related to $\dot{N}$ as follows:

$$C = 10^9 \frac{\dot{N}RT}{MPQ} \tag{8-2}$$

where M is the molecular weight of the gas in question and Q is the flow rate.

Further, if we define a new rate quantity, $\tilde{\dot{N}}$, as the gas generation rate (in g/s) per unit length of actuator, the Equation (8-2) becomes

$$C = 10^9 \frac{\tilde{\dot{N}}RTL}{MPQ} \tag{8-3}$$

where L is the length of the actuator.

Applying Equation (8-3), and using the data collected in the three trials for the 40 mil Cirlex, we plot the ozone source strength (in μg/s/m) as a function of voltage in Figure 64. The pressure, P, is taken to be atmospheric pressure (e.g., 1 atm) and the measured temperature was 24 deg C (300 K). The molecular weight of ozone, represented by M in Equation (8-3), is 48 g/mol. The plotted ozone data (the blue curve) represents the average over three trials and the superposed

error bars show the high and low value at each voltage. The red curve shows measured ozone for a 40 mil Cirlex actuator with a serrated exposed electrode (as pictured in Figure 60). Only a single trial was recorded for the serrated electrode.

Figure 65 and Figure 66 show the ozone and NO_2 source strength, respectively, as a function of applied voltage for four different plasma actuators. In general, for a given voltage, the thinner dielectrics produce more gaseous byproducts. This is consistent with the fact that the plasma volumes are greater for thinner dielectrics at a given voltage and the resulting thrust is greater. However, thicker dielectrics permit higher voltages in general, so that for a given thrust, we find that the actuators produce about the same amount of gaseous by product (see Figure 67). When the serrated exposed electrode is used, we measure an increase in both the thrust generated and the amount of gaseous byproduct. An increase in thrust was expected, as similar results have appeared in several prominent publications.

Interestingly, when we apply a thin layer of titania on the exposed surface of the dielectric (the part of the dielectric on which plasma forms), we see the opposite effect. In other words, while we measure a marked (20-120%) increase in thrust, we also measure a 10-30% decrease in the amount of ozone and NO_2 produced. This is evident in Figure 65 and Figure 66. In earlier work, reported in (Fine & Brickner, Plasma Catalysis for Enhanced-Thrust Single Dielectric Barrier Discharge Plasma Actuators, 2010), we hypothesized that the increase in thrust which resulted from the application of the titania catalyst may result from an increase in the production of certain ions of oxygen, which would lead to more ion-neutral collisions and, hence, additional thrust. A simultaneous decrease in the amount of ozone and N_2O may be a consequence of the same chemistry that produces more oxygen ions. In other words, when the catalyst is used, a greater number of oxygen molecules could go into the production of oxygen ions that would otherwise have contributed to the production of the neutral O_3 and NO_2 molecules. This data may be interpreted as being supportive of the proposed explanation for the increased thrust, although it is by no means conclusive. Further systematic measurements might yield more conclusive evidence and, importantly, insights into how to further optimize the plasma actuator with applied catalysts.

Finally, we examined the variation in ozone and NO_2 concentration as a function of frequency for the 140 mil PTFE actuator, with voltage held fixed at 6 kV. For this experiment, we varied the frequency from 500 Hz to 4 kHz in 500 Hz increments and from 4 kHz to 7 kHz in 1 kHz increments. The showed less variation than with voltage, and showed monotonic increase with frequency. The results are shown in Figure 68.

Plasma Flow Control for Wind Turbines – Final Report　　　　Navatek, Ltd.

NAVATEK TR--2013/2
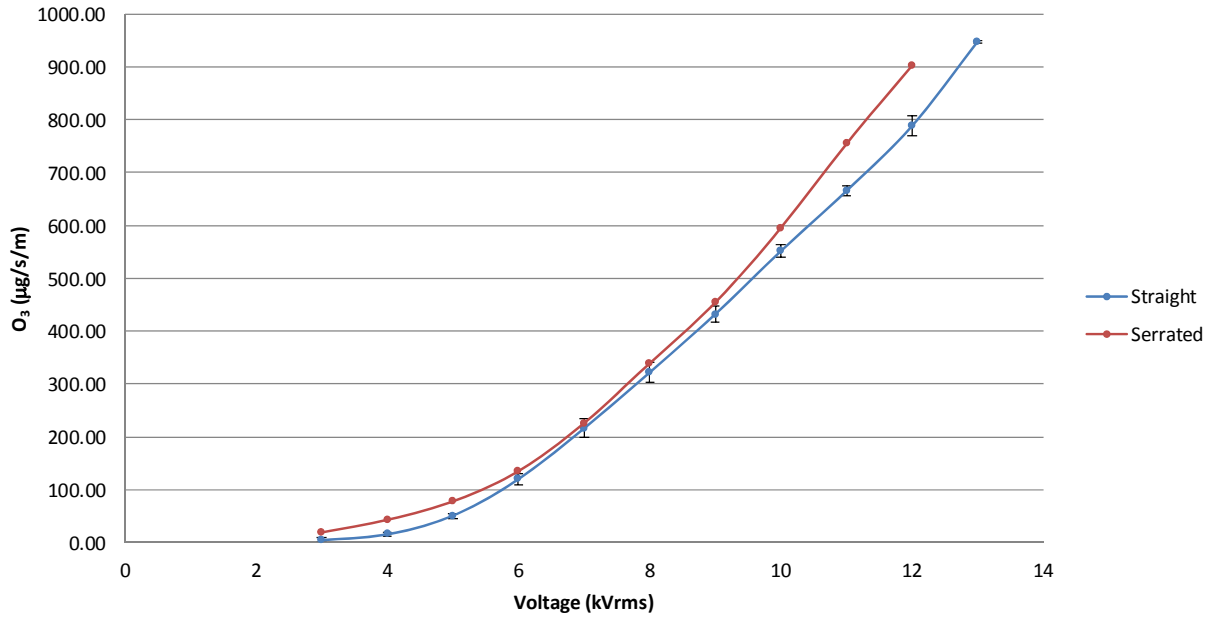
Figure 64. Ozone source strength: straight vs. serrated actuator. *This plot shows ozone source strength derived from raw data measured for the 40 mil Cirlex actuator (straight and serrated exposed electrode).*
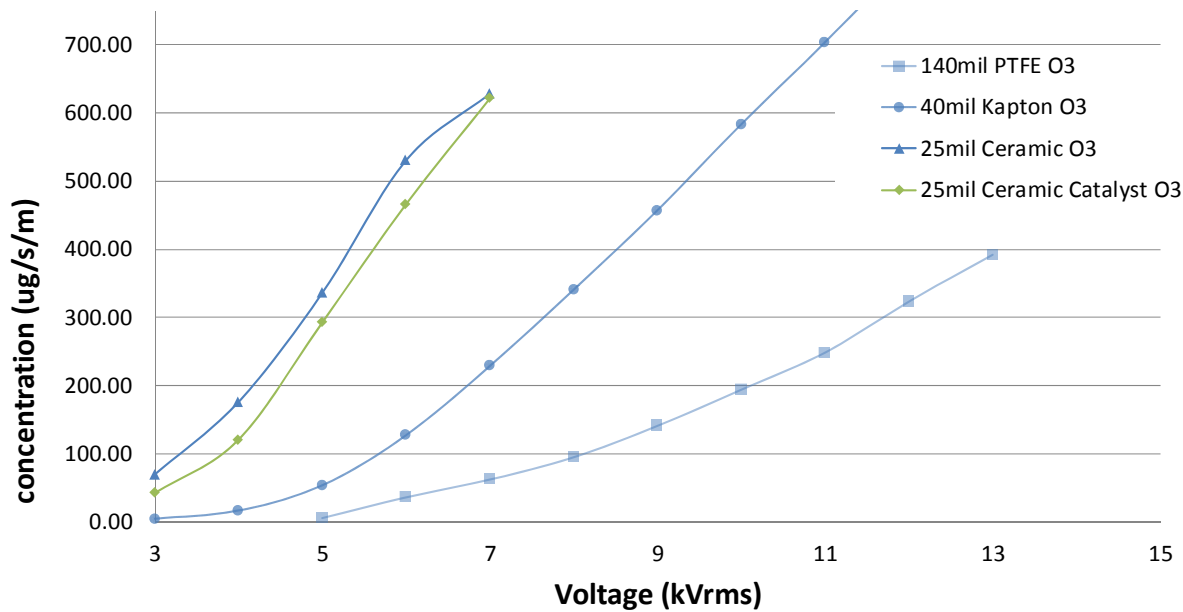
Figure 65. Ozone source strength: actuator material and thickness comparison. *This plot shows ozone source strength as a function of applied voltage for four plasma actuators.*
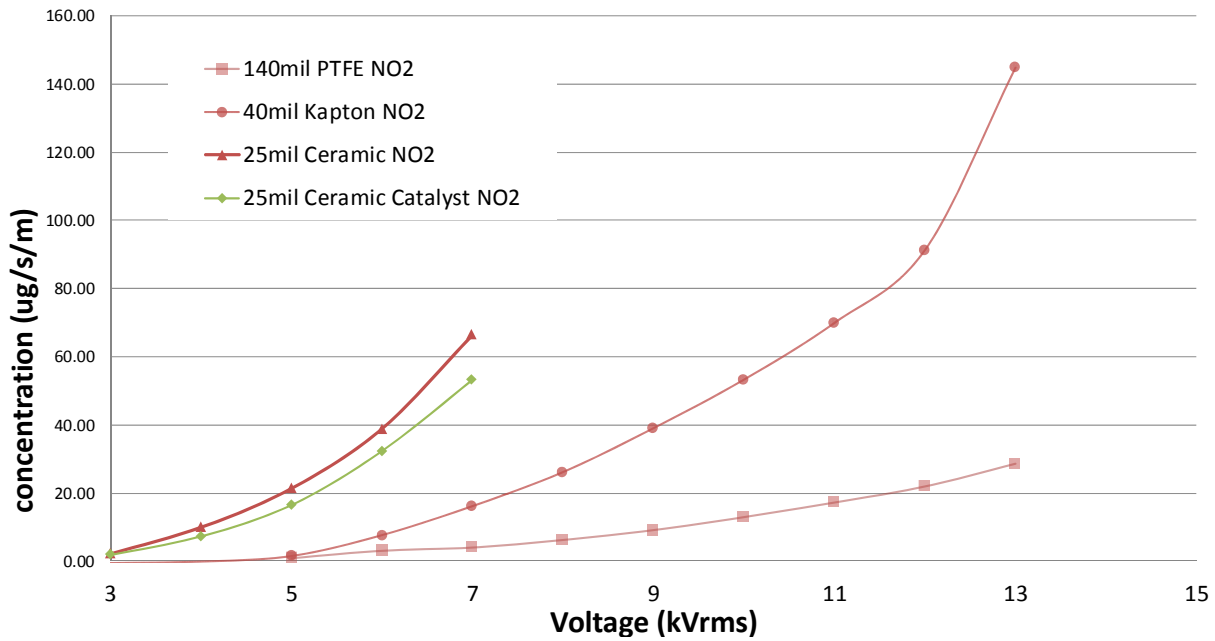
Figure 66. Ozone source strength: actuator material and thickness comparison. *This plot shows NO₂ source strength as a function of applied voltage for four plasma actuators.*
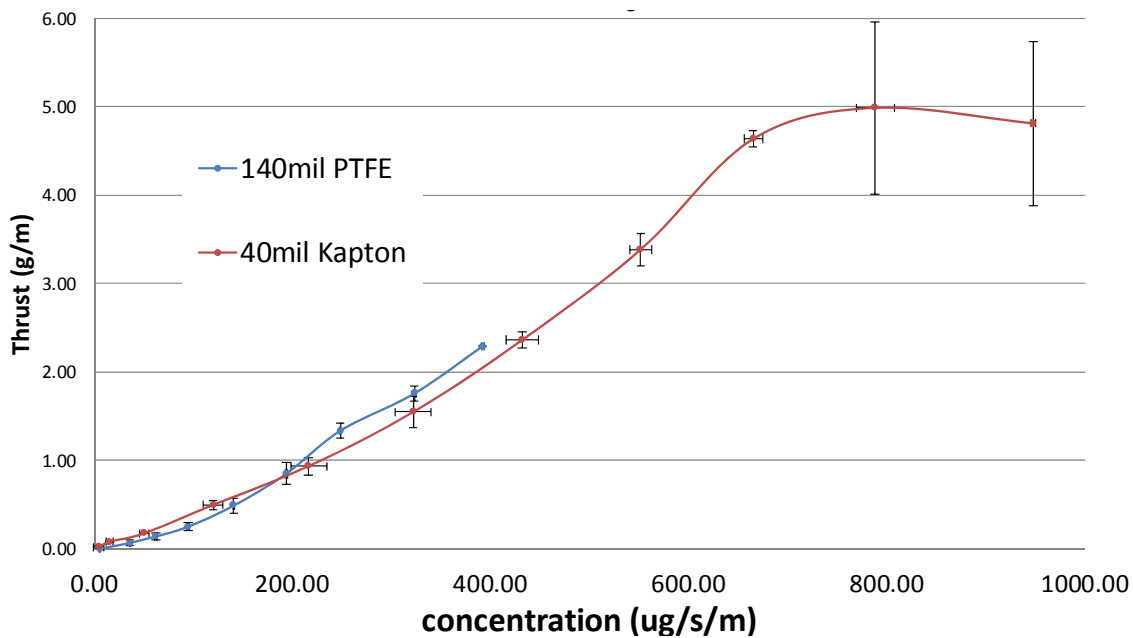
Figure 67. Relationship between actuator thrust and Ozone source strength. *Thrust vs. ozone source strength for two plasma actuators.*
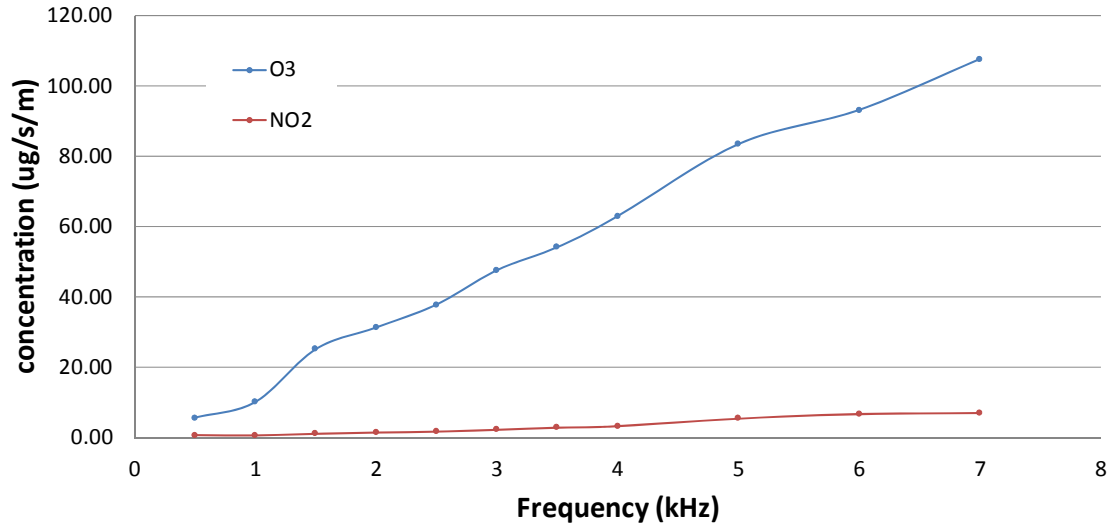
Figure 68. Effect of A/C frequency on ozone and NO2 production. *This plot shows the variation in ozone and NO_2 source strength as a function of a/c frequency for the 140 mil PTFE actuator.*

8.7   Implications for Full Scale

In this section, we will use the data collected in these experiments to estimate the concentration of ozone and NO_2 downstream of a wind turbine, when plasma actuators are used for active flow control. We will assume that all of the gaseous byproducts remain within the stream tube downstream of the wind turbine (see Figure 69). We know, of course, that the gradient in concentration will drive the dispersion beyond the stream tube, but this assumption will give us an upper bound on the concentration of the byproducts. We will also assume that the plasma actuators are on continuously, when in practice a 10% duty cycle is likely to be employed.
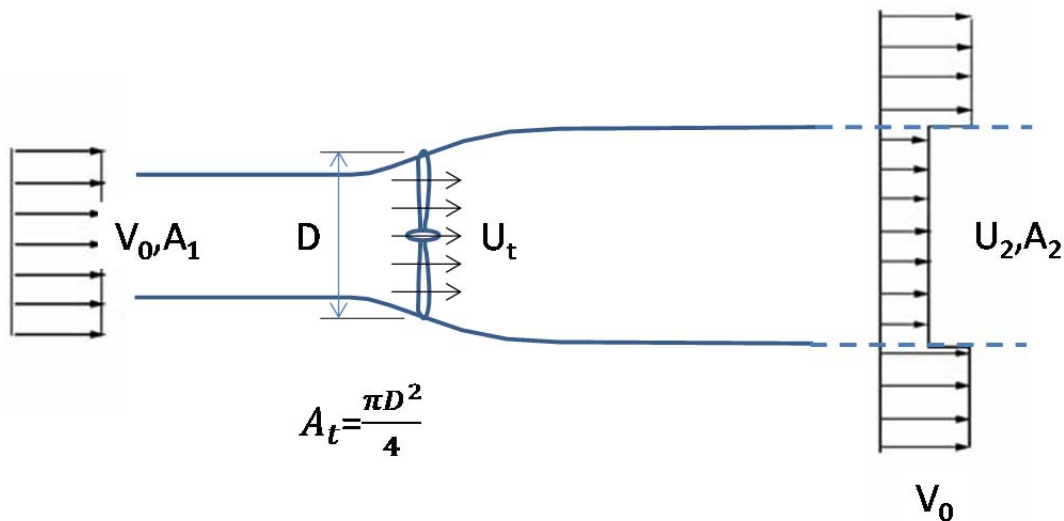
Figure 69. Wind turbine control volume analysis. *This schematic provides a one-dimensional description of the flow past a wind turbine, defining terms for the control volume analysis of Section 8.6..*

The flow rate within the stream tubes can be found from the average axial velocity through the plane of the turbine (U_t in Figure 69) and the diameter of the turbine:

$$Q = \frac{\pi D^2}{4} U_t \tag{8-4}$$

Inserting (8-4) in (8-3) then yields:

$$C = 10^9 \frac{\tilde{N} RTL}{\frac{\pi}{4} D^2 MP U_t} \tag{8-5}$$

To compute the concentration downstream of a real turbine then requires that we derive an expression for the mean velocity at the rotor plane.

Following the logic of classical one-dimensional momentum theory, we can write Bernoulli's equation for a streamline between an upstream point where the velocity is V_0 (that is, the ambient wind speed) and just upstream of the turbine plane, where the pressure is P^+ and the velocity is U_t:

$$P_\infty + \frac{1}{2}\rho V_0^2 = P^+ + \frac{1}{2}\rho U_t^2. \tag{8-6}$$

Similarly, for the streamline that begins just downstream of the wind turbine, we can write:

$$P_\infty + \frac{1}{2}\rho U_2^2 = P^- + \frac{1}{2}\rho U_t^2 \tag{8-7}$$

Taking the difference (8-6) – (8-7) yields

$$\Delta P = \frac{1}{2}\rho(V_0^2 - U_2^2) \tag{8-8}$$

where ΔP is the pressure jump across the turbine plane. From momentum conservation, we also know that the axial force exerted on the turbine must be balanced by the difference in momentum from upstream to downstream. We can use this to derive an alternative expression for the pressure jump across the turbine plane:

$$\Delta P = \frac{\rho A_1 V_0^2 - \rho A_2 U_2^2}{A_t} \tag{8-9}$$

Mass conservation requires that $U_2 = \frac{A_1}{A_2} V_0$, so (8-9) can be written:

$$\Delta P = \frac{\rho A_1 V_0 (V_0 - U_2)}{A_t} \tag{8-10}$$

Equations (8-8) and (8-10) are two expressions defining the pressure jump across the turbine plane. Their right hand sides can therefore be equated to yield:

$$\frac{\rho A_1 V_0 (V_0 - U_2)}{A_t} = \frac{1}{2}\rho(V_0^2 - U_2^2) \tag{8-11}$$

which can be simplified to:

$$\frac{A_1 V_0}{A_t} = \frac{1}{2}(V_0 + U_2). \tag{8-12}$$

Again applying mass conservation, which requires that $U_t = \frac{A_1}{A_t}V_0$, Equation (8-12) implies that

$$U_t = \frac{1}{2}(V_0 + U_2) \tag{8-13}$$

Now, following the logic of Betz, we define the parameter $a = \frac{U_2}{V_0}$, so that (8-13) becomes

$$U_t = \frac{1}{2}V_0(1 + a) \tag{8-14}$$

If we continued to follow Betz' logic, we could derive an expression for the optimum power coefficient associated with the optimal choice of the parameter a. Doing that we would find, first, that the optimal power coefficient is $C_P = \frac{16}{27} \approx 0.593$, corresponding to $a = \frac{1}{3}$. This is the well-known Betz limit. Further, for points away from the optimum (e.g., for C_P less than 0.5) corresponding to positive values of the downstream velocity, the value of a is always greater than 1/3. Therefore, the most conservative analysis for the downstream concentration defined by Equation (8-5) corresponds to the Betz limit. Therefore, we can assume that

$$U_t = \frac{2}{3}V_0 \tag{8-15}$$

Equation (8-5) now becomes

$$C = 10^9 \frac{\dot{\tilde{N}}RTL}{\frac{\pi}{6}D^2 MPV_0} \tag{8-16}$$

One thing to note from this expression is that the concentration will drop in proportion to the turbine diameter. This results from the fact that the actuator length, L, is proportional to turbine diameter, D, cancelling out one factor of D appearing in the denominator of (8-16).

Taking the Renewegy VP20 as an example, for which D=9.2m, and assuming that each blade will have three strips of actuator each 4 meters in length, and each consisting of a 40 mil thick Cirlex dielectric operating at 10 kV, and assuming a wind speed of 10 m/s, we calculate the downstream concentration of ozone to be

$$C = 10^9 \frac{\left(551x10^{-6}\frac{g}{m \cdot s}\right)\left(8.25x10^{-5}\frac{atm \cdot m^3}{mol \cdot K}\right)(300K)(36m)}{\frac{\pi}{6}(9.2m)^2(48\frac{g}{mol})(1atm)(10\frac{m}{s})} = 23 \text{ ppb.}$$

According to data from the International Ozone Association, typical ozone concentrations found in the natural atmosphere fall between 1 and 125 ppb. These levels of concentration vary with altitude, atmospheric conditions and locale (Rasplicka, 2008).

A similar calculation yields an estimate of the NO_2 concentration of about 2.3 ppb. ASHRAE and the U.S. EPA National Ambient Air Quality Standards list 53 ppb as the average 24-hour limit for NO_2 in outdoor air (EPA, 2013)

8.8   Conclusions

In this section, we describe experiments in which the concentration of certain gaseous byproducts (namely, ozone and nitrogen dioxide) of plasma actuators was measured in the lab. Using this data, we derived a conservative estimate of the concentration levels downstream of a VP20 wind turbine operating at the Betz limit in 10 m/s winds. The ozone level for that situation was estimated to be 23 ppb, while the nitrogen dioxide concentration was estimated to be one tenth of that. Not only do those levels fall within the range of natural environmental values, but they are about 4 orders of magnitudes lower than standard emission limits for gas turbines, which are among the cleanest of the fossil fuel energy sources which wind energy will supplant.

We note again that the estimated concentrations for full-scale wind turbine installations presented here are conservatively high, because they assume that all of the byproduct gases will be constrained to the stream tube downstream of the turbine, and because the turbine is assumed to operate at the Betz limit. Also, we assumed that the actuators would operate in steady mode, when in reality they will likely be operated in a pulsed mode at a low duty cycle. Finally, we note that larger turbines will lead to lower concentrations in inverse proportion to their increased diameter.

Finally, we note the interesting result found when a thin layer of titania was fixed to the surface of the dielectric exposed to the plasma. This is the only case where a measured increase in thrust was accompanied by a decrease in gaseous byproduct for a fixed voltage – the opposite was generally the case, as with the use of a serrated electrode or a thinner dielectric. The result may be construed as support for a hypothesized increase in the generation of certain oxide ions resulting from catalytic activity of the titania (Fine & Brickner, Plasma Catalysis for Enhanced-Thrust Single Dielectric Barrier Discharge Plasma Actuators, 2010). Further experiments are needed to shed more light on the phenomenon.

9.   Wind Turbine Installation and Testing

9.1   Actuators

Based on wind tunnel testing, 20mil Cirlex was chosen as the optimal dielectric material for use on the Renewegy VP20 wind turbine blades (see Section 4.6). It strikes the best balance between the thicknesses necessary for good actuator control authority while still being thin enough to not have a large negative effect on the baseline aerodynamic performance.

During testing, it was noticed that Cirlex actuators would fail at seemingly random times. The mode of failure was an electrical arc through the dielectric material between the electrodes. This creates a permanent pathway of low resistance such that all current passes through it at voltages lower than that necessary for the ignition of plasma. An actuator that has failed in this way is, as far as we can tell, irreparable. After extended operation, an etching of the dielectric material in the plasma region was also noted. Before installation on the turbine, actuator longevity needed to be tested and addressed.

One mil thick Kapton CR with a silicone adhesive on one side was purchased to help with this issue. Kapton CR is a polyimide film "developed specifically to withstand the damaging effects of partial discharge, which can cause ionization and eventual breakdown of an insulation material." Test actuators were constructed in different layering configurations using Teflon (PTFE), Cirlex (Cir) and the Kapton CR (CR). Test actuators were run continuously at 6kV, 3 kHz until failure occurred. The results of this test are plotted in Figure 70. The laminate schedule of each actuator is shown next to its data point in the plot. The number preceding the material abbreviation is the thickness of that layer in mils. Time to failure is plotted against theoretical breakdown voltage calculated as the sum of the product of the dielectric strengths and thicknesses for each layer (excluding adhesives). In practice, the actual breakdown voltage is much lower than the theoretical due to impurities, cavities, and other material imperfections.
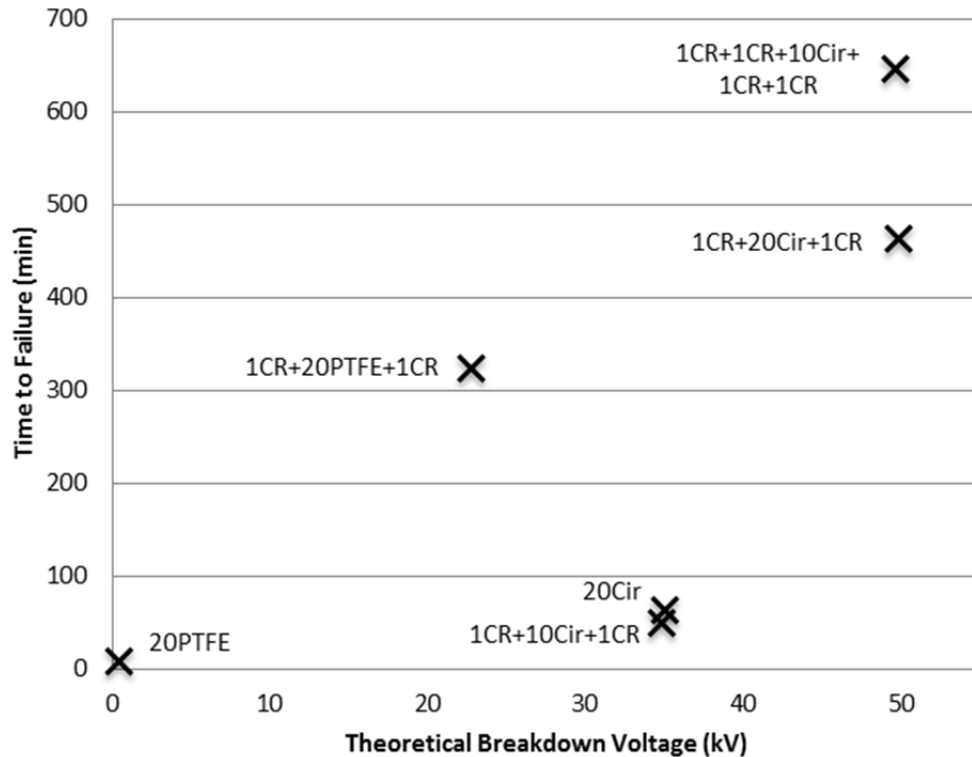
Figure 70. Actuator longevity. *This plot shows results of actuator longevity tests (6 kV, 3 kHz).*

The 20 mil Cirlex lasted 63 minutes before failure. The best configuration tested was the 10 mil Cirlex with 2 layers of Kapton CR on each side. It lasted nearly 11 hours and (including adhesives) also has a thickness of 20 mils. It is this configuration that was chosen for construction of actuators for full scale testing. Actuators were made in 23.5" long sections for ease of construction, installation, and replacement if necessary. Figure 71 shows a diagram of final the construction geometry. Dimensions are in inches and the drawing is not to scale.
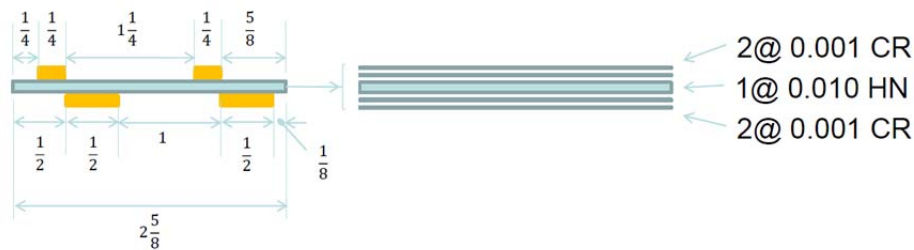
Figure 71. Actuator construction geometry. *This schematic shows the arrangement the electrodes on the Cirlex and instructions for layering the Kapton sheets. CR refers to Dupont's Kapton-CR polyimide film, and HN refers to the Kapton-HN polyimide variant.*

In addition, multiple layers of Kapton tape were used to suppress plasma discharge on the bottom side of the actuator and in other undesired places.

Six actuators were used per blade. They were spaced from the tip of the blade to roughly two feet from the first airfoil profile leaving about a 1/8" gap between actuators. The trailing edge of the

actuator was aligned with the trailing edge of the blade throughout its span. Actuators were wired together using 30 AWG magnet wire. The actuators were glued and vacuum bagged to the blade using 3M 5200. In addition, all edges were taped using 1mil Kapton tape.

Figure 72. Actuators installed on a VP20 blade. *This picture shows the six actuators affixed to one of the three VP20 turbine blades.*

9.2   Full Scale Power Supply Implementation

Powering actuators on rotating turbine blades poses many challenges not present in the lab. One large challenge was transferring electrical power to the rotating hub which requires a slip ring. Space on the nacelle of the VP20 for the installation of a slip ring was limited. Both the size and cost of a slip ring to transfer the high voltages required for the actuators was prohibitive. This led to the decision to mount the step-up transformers on the hub of the turbine, reducing the slip ring voltage requirements to a more reasonable value of about 200 volts. A custom slip ring solution was designed and manufactured with Rotary System, Inc. The rotor of the slip ring is set screw fastened to a small machined round surface on the rotating pitch hub just forward of the brake disk. The stator is held in place by an L-bracket that bolts to the gear case behind the brake disk and extends forward past the disk to an anti-rotation pin extending radially from the slip ring. The slip ring has three channels rated for 400 volts and 5 amps. Installation of the slip ring was done at Renewegy's facility as it is manufactured as one piece and must be installed during assembly of the turbine. Figure 73 shows the slip ring after installation on the turbine. The anti-rotation pin can be seen extending up past the brake disc at the top of the ring.
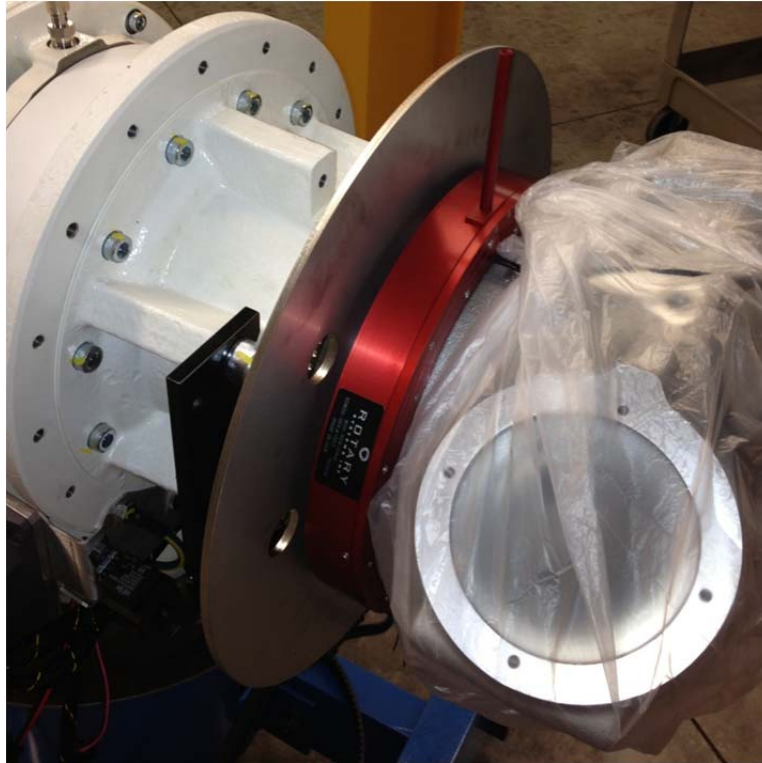
Figure 73. Slip ring installation. *This picture shows the custom-made slip ring just after installation on the turbine drivetrain.*

The VP20 turbine also shipped with the addition of a second trunk cable and harness running through the tower and into the nacelle to support the plasma system. The extra cable contained four 14 AWG conductors.

Figure 74 shows a high level electrical schematic for the full scale test.
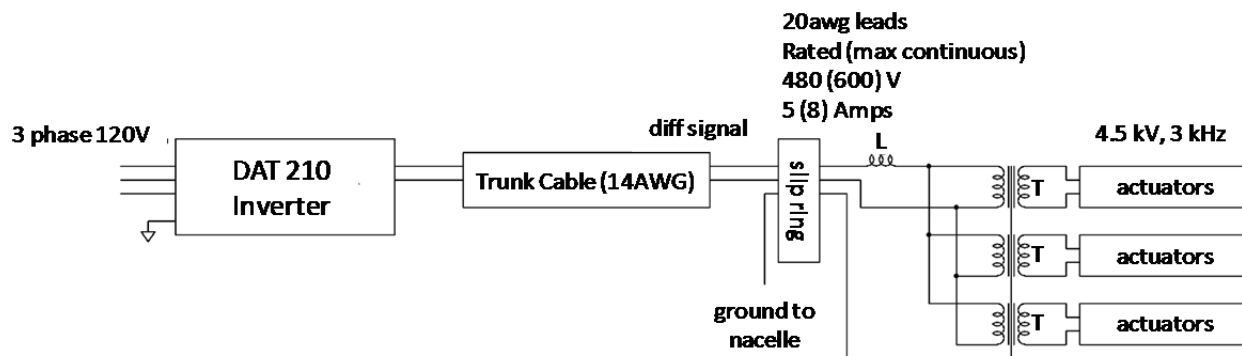
Figure 74. Electrical schematic for full scale test. *This circuit diagram shows the connectivity between the DAT210 inverter (left) through the slip ring (center) and to the transformers, inductor and actuators (right).*

A resonant power supply consisting of an inverter, three transformers and a matched inductor were sourced from Plasma Technics, Inc. Plasma Technics specializes in high voltage systems for corona discharge ozone generation and other applications similar to plasma actuators. The inverter is a DAT210 which is designed to be highly efficient and self-optimizing. It can automatically tune the operating frequency in response to changing load conditions to maintain a

Plasma Flow Control for Wind Turbines – Final Report   Navatek, Ltd.

NAVATEK TR--2013/2

consistent output and minimize losses. Three step-up transformers were used, one for each blade. This configuration was chosen over one large transformer due to space limitation and balancing considerations on the hub of the turbine. The transformers were a dry type model SP326 capable of a secondary voltage of 10kV and rated at 1000VA. The transformers were paired with a SP252-2 inductor wired for 5mH inductance. During testing, the system was found to reliably supply 4.5kV at 3 kHz to the actuators.

It was not necessary to mount the inverter on the turbine. In fact, it was preferable to have it somewhere accessible to allow for monitoring and adjusting the system. It was housed in an acrylic case on a shelf at the base of the turbine inside the dry dock wing wall seen in Figure 75.
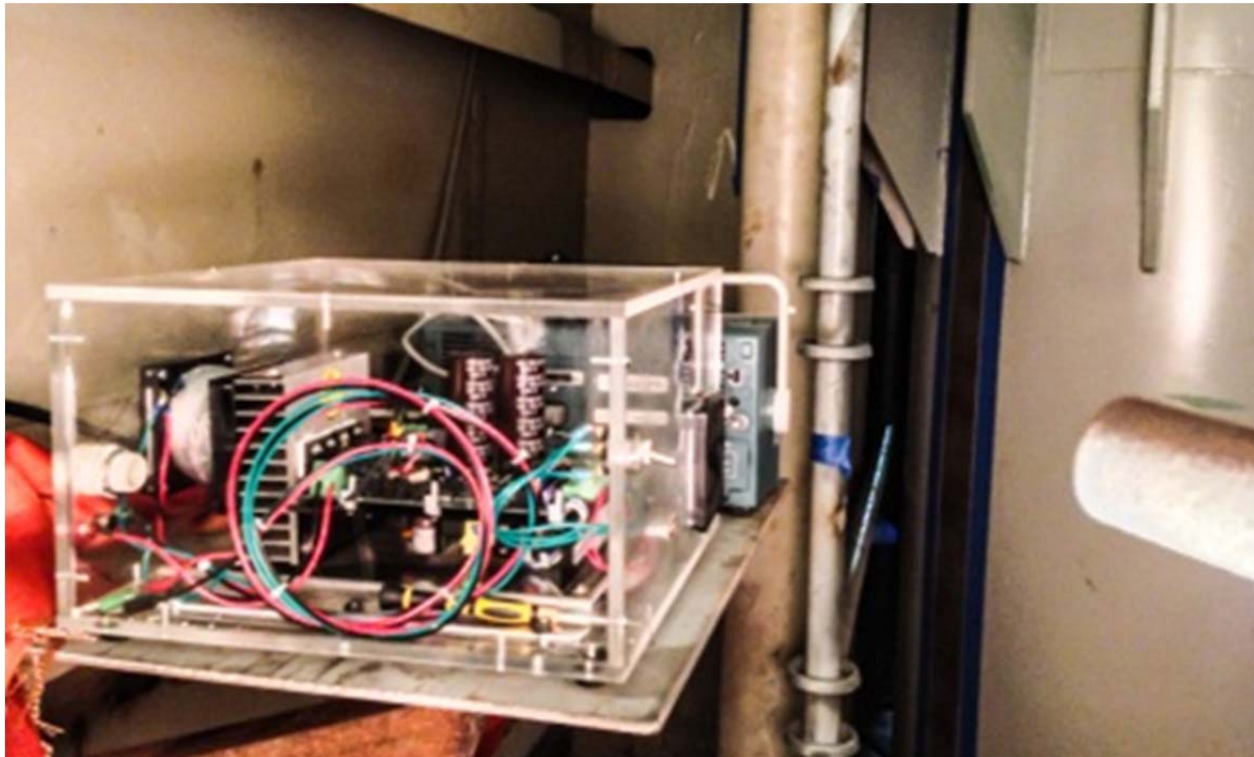
Figure 75. Installed inverter. *This picture shows the DAT210 inverter housed inside the dry dock wing wall at the base of the turbine.*

Space inside the nosecone was limited. A bracket for the components was designed that attaches to the pitch hub using the existing bolt holes for the nose cone. The transformers were attached to the bracket as seen in Figure 76 to maintain rotational symmetry. The inductor was located at the forward center area in the nose cone. It was mounted on a bracket that allowed translation along all three axes to facilitate balancing if necessary. Figure 76 shows a CAD model of the hub with the added components and a photo of the components mounted on the hub without the nose cone.
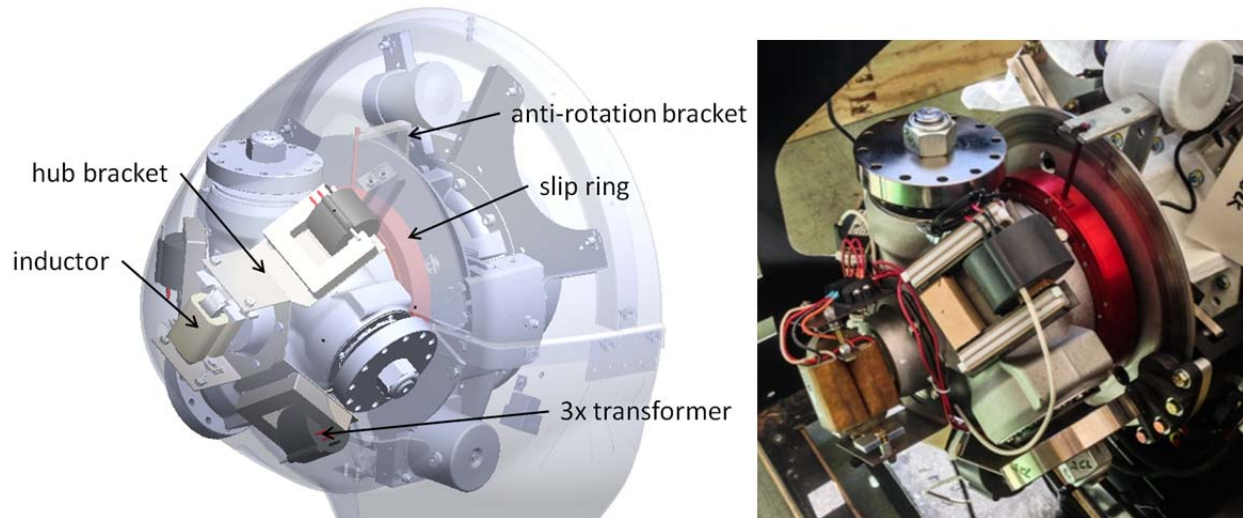
Figure 76. Turbine hub arrangements. *This picture shows the plasma system components on the hub of the turbine. The detailed 3D model (left) was used to design the mounting bracket which holds the transformers and inductor in the rotating hub.*

The high voltage output wire from the transformers was additionally insulated with PVC tubing to prevent any corona discharge or arcing to the metal flanges at the root of the blades. During final installation, the high voltage wire was fastened to the blade at the root with cable ties leaving enough slack to allow the blades to rotate through their full range of pitch angles. Connection was made to the actuators using 14 AWG wires taped securely to the surface of the blade. Actuators were grounded to a bolt securing the blade to the hub. The hub was grounded through the slip ring. Figure 77 shows an actuator ignited at the root of a blade and the lead wires taped back to the hub after completion of the installation.

Figure 77. Glowing actuators on the VP20. *This picture shows the plasma actuators ignited against the night sky on the blades after final installation.*

9.3   Turbine Testing

The Renewegy turbines are equipped with detailed data logging capabilities. Instantaneous wind speed, instantaneous power, pitch and yaw angles, generator speed, and other calculated quantities can be recorded at a 1 Hz rate.

There was not an obvious difference in power generation between the turbine without the plasma system and the turbine with the plasma system and the actuators turned off. This indicates that the addition of actuators on the surface on the blade do not have a significant aerodynamic impact. This is consistent with our observations in the wind tunnel (see Section 4.6). While the turbines are identical models and located close together, there will still inevitably be variations in the power they produce. For this reason, testing will focus only on the turbine with the plasma system and compare its performance with the actuators off versus on.

Data was recorded over many hours encompassing a wide range of wind conditions. The plasma system was switched on and off at regular intervals. The best way to visualize the data was found to be plotting the instantaneous power versus wind speed. This data is shown below in Figure 78. Red points represent data recorded with the plasma actuators on, and blue points are with the plasma off. Data was parsed into 0.05 m/s wind speed bins. The median values of each bin are represented by the red and blue lines for plasma on and off respectively. The black line is the ratio of the median values of plasma on to plasma off. It is multiplied by 10 for clarity.
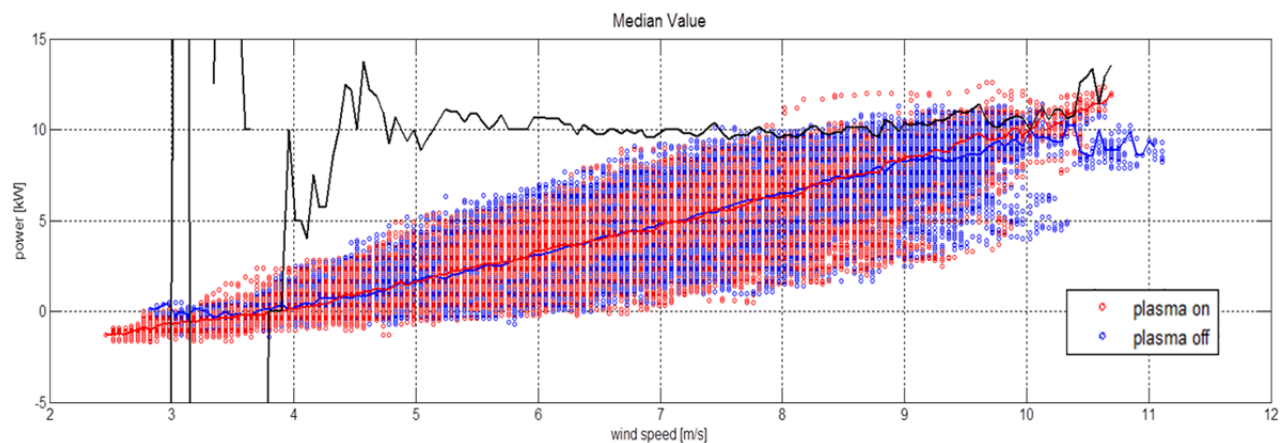
Figure 78. Turbine power measurements. *This plot shows instantaneous power generation versus wind speed with the plasma system on (red) and off (blue).*

The data presented in Figure 78 is further processed by computing the ratio of the median "plasma-on" power to the median "plasma off" power in 1 m/s bins. The results are shown in Figure 79.
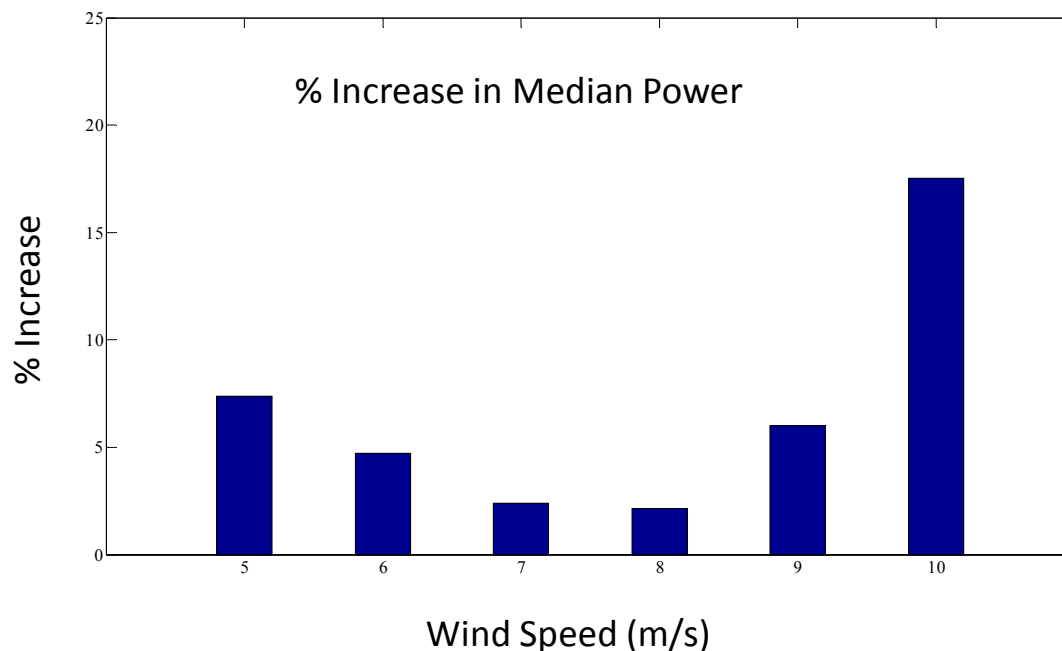
Figure 79. Increase in median power due to the plasma flow control system. *This bar chart shows the gain in median power due to plasma actuation, averaged over wind speeds in 1-m/s bins. For example, the first bar in the chart represents the median power increase with the plasma on averaged over all data points with wind speeds in the 5-6 m/s range.*

It is somewhat disconcerting that there is a wide range of instantaneous powers for each wind speed, as can be seen in Figure 78. According to the manufacturer, this spread largely results from latency between the wind speed measurement and the power measurement. Because of that latency, it is difficult to assign error bars to the measurements shown in Figure 78 and the derived data shown in Figure 79. Ongoing work will investigate this further. Until then, the results shown in these figures are suspect and may change with further data collection and analysis.

Also interesting to note is starting after 8 m/s, the maximum power for a given speed occurs with the plasma on and is significantly higher than the bulk of the data. This could indicate that plasma is especially beneficial at high wind speeds when the other turbine variables are optimized. At speeds higher than 9 m/s, a significant and consistent increase in power generation is seen with plasma on, while below 9 m/s it is more comparable to plasma off. This increase around 9 m/s is consistent with our model (Figure 52). Also interesting is the lower cut-in speed that is evident with the plasma on. Although not unexpected, the benefits of the lower cut-in speed have been shown to be negligible because of the small amount of power generated at low wind speeds.

10.   Cost of Energy Modeling

10.1   Model Description and Assumptions

Consider a "baseline" offshore wind farm consisting of 100 pitch-regulated, variable speed turbines, each rated at 5 MW. To estimate the potential CoE reduction through implementation of active flow control, we assume that this baseline wind farm will be replaced with a proposed wind farm consisting of "next generation" turbines incorporating smart blade technology using plasma flow control. Specifically, the plasma flow control system will mitigate unsteady blade loading and increase the low-wind speed power coefficient. Reducing the cyclic loading and aeroelastic response to gusts and turbulence will enable the future turbine designer to use larger diameter, more flexible rotors with lower solidity.   The turbines will use a downwind configuration to allow blade flexure, with integrated flow control on the cylindrical tower to reduce the wake defect and to introduce a small pre-swirl velocity component. The downwind configuration will eliminate the need for tilt and forward-coning of the blades to ensure adequate tip clearance (as required for a flexible upwind rotor), which studies have shown can sacrifice more than 4% of the captured energy (Energy, 2006). The combination of reduced blade weight and fatigue loads will permit the use of a lighter gearbox, drive train, tower and foundation relative to the baseline system, while extending the life of these and other components. Plasma actuators near the leading edge will reduce blade soiling losses. The use of advanced control algorithms will improve low-wind speed capture while reducing pitch activity. At the inboard stations, the addition of active flow control will permit the use of thicker blade sections with shorter chord lengths, enabling more structurally efficient designs and a shift in material outboard to enlarge the diameter (Ashwill, 2005).

The levelized cost of energy in constant dollars ($ per kW-hr) is calculated for a wind farm with an expected operating life of 20 years using the following expression:

$$CoE = \frac{ICCx(DR+IWF)+LRC+O\&M}{AEP_{net}}$$
(10-1)

where *ICC* represents the initial capital costs ($), *DR* is the discount rate (per year), *IWF* is a rate that covers insurance, warrantee and other fees (per year), LRC represents the levelized replacement/overhaul costs ($ per year), O&M represents the operations and maintenance costs ($ per year), and AEPnet is the net annual energy production (kW-hr per year).

Table 3 describes the baseline and proposed system configurations. A CoE analysis was performed on both systems, following the procedure published in IEC Standard 61400-12-1 (IEC, 2005). The model was implemented in an Excel workbook.

Table 3. Baseline and proposed system configurations.

Description	Baseline	Proposed
Wind Plant Rating (MW)	500	700
Number of Turbines	100	100
System Design Life (years)	20	20
Turbine Rating (kW)	5000	7000
Rotor Diameter (m)	126	151
Hub Height (m)	95	95
Distance to Shore (km), depth (m)	25, 30	25, 30
Wind Speed @ Hub Height (m/s)	10	10
Weibull K Factor, base wind shear	2, 0.1	2, 0.1
Air Density (kg/m^3)	1.225	1.225
Max Rotor Cp	0.474	0.533
$V_{cut\text{-}in}$ (m/s)	3	3
$V_{cut\text{-}out}$ (m/s)	25	25
Losses (computed)	19%	17%
Availability (computed)	95%	97%

10.2   Initial Capital Costs

Table 4 summarizes the initial capital costs for both the baseline and proposed wind farm. Detailed cost data for the baseline system was taken from a 2010 report by BVG Associates (Associates, 2010). These data are specific to potential offshore wind farm installations in European coastal waters, and may not be accurate for U.S. installations. However, they should suffice for the purpose of estimating potential CoE reductions.

All rotor component costs are assumed to increase in proportion to the increase in diameter (or the square root of the increase in power, e.g., $\sqrt{7000\ kW/5000\ kW} = 1.18$. The material costs for the blades may, in fact, not increase in proportion to span because active flow control is expected to permit some of the inboard material to be moved to the tip . Also, the use of softer blades with less internal structure can be expected to result in material savings. These potential savings are not included in this analysis, leading to a conservative estimate of improvement. The initial capital costs for the proposed system incorporate a cost increase for the active flow control system ($200K per turbine). The cost of the tower and foundation are assumed to increase in proportion to the additional height of the tower, or about 18%. The cost of the drivetrain is assumed to increase in proportion to the increase in power, along with the balance of plant and installation costs.

Plasma Flow Control for Wind Turbines – Final Report   Navatek, Ltd.

NAVATEK TR--2013/2

Table 4. Baseline and proposed initial capital costs.

		Baseline($K)	Proposed ($K)
Turbine Capital Costs	**Rotor**		
	Blades	1710	2023
	Hub Casting	130	154
	Blade Bearings	80	95
	Pitch system	245	290
	Spinner	40	47
	Rotor Auxiliary	15	18
	Fabricated Steel Components	35	41
	Rotor Total:	**2255**	**2668**
	Drive train, nacelle		
	Nacelle bedplate	195	273
	Main Bearing	130	182
	Main Shaft	165	231
	Gearbox	1625	2275
	Generator	405	567
	Power Take-off	650	910
	Control System	115	161
	Yaw System	165	231
	Yaw Bearing	80	112
	Nacelle Auxiliary Systems	25	35
	Nacelle Cover	145	203
	Small Engineering Components	10	14
	Condition Monitoring System	35	49
	Drive Train, Nacelle Total:	**3745**	**5243**
	Tower	**1625**	**1920.0**
	Foundation	**4880**	**5770.0**
Balance of Plant Costs	**Cables**	**130144**	**182200**
	Offshore Substation	**81340**	**113880**
	Onshore Substation	**406700**	**569380**
Installation and Commissioning Costs	**Export Cable Laying**	**130144**	**182200**
	Foundation Installation	**162680**	**227800**
	Array Cable Laying	**97608**	**136700**
	Construction Port	**16268**	**22800**
	Offshore Substation Installation	**16268**	**22800**
	Turbine Installation & Commissioning	**227752**	**318900**
	Total ($K)	**1281409**	**1812261**

10.3   Discount Rate and Insurance, Warranty and other Fees

The discount rate (DR) reflects finance charges, debt or equity repayment, construction financing, and the cost of capital. Computing DR requires assumptions regarding inflation rates and tax protection benefits, among other factors. To simplify, a "composite" discount rate is used for the purposes of these cost comparisons. At the recommendation of the DOE (George & Schweitzer, 2006), DR is fixed at 7% for a 20 year project life.

In addition to the discount rate, there are additional finance charges due to insurance, warranty and other fees (*IWF*) over the life of the project. For the purposes of these cost comparisons, *IWF* is set at 1%.

10.4　Levelized Replacement Costs

Levelized Replacement/Overhaul Costs (LRC) account for the cost of major replacements (such as gearboxes, blades and other high cost components) and overhauls, distributed over the life of the wind turbine. Downtime during replacements and overhauls is also included in the determination of overall turbine availability when calculating annual energy production. In the pro forma cash flow model, one "saves" for replacements and overhauls with deposits to a reserve fund in the years preceding the maintenance event. The repair is then depreciated linearly. Consequently, both of these items – the major maintenance reserve fund and the repair depreciation – are incorporated into the calculation of LRC.

The present value of each stream of reserve fund deposits incurred for the nth discrete replacement and overhaul event, *PV(n)*, is computed as follows:

$$PV(n) = PVF(n_{mp}) x RC_{2012} x 1.03^n \qquad (10\text{-}2)$$

where *RC* is the replacement or overhaul cost (in 2012 dollars), *PVF(nmp)* is the present value factor for the mid-point year of the reserve fund payment stream, and the inflation rate is assumed to be 3% annually. PVF is computed from the nominal discount rate, *i*:

$$PVF(nmp) = (1 + i)^{-n_{mp}} \qquad (10\text{-}3)$$

For this analysis, we assume a nominal discount rate of *i*=9.25%.

The LRC is calculated – in constant dollars – by multiplying the sum of present values of the reserve fund payment streams by the Capital Recovery Factor (CRF):

$$LRC = 0.8 x CRF x \sum_n PV(n) \qquad (10\text{-}4)$$

where

$$CRF = \frac{i_{const}}{1-(1+i_{const})^{-30}} \qquad (10\text{-}5)$$

and where i_{const} is the constant dollar discount rate, taken here to be 6.07%. Note that the factor 0.80 in Equation (10-4) accounts for depreciation of each replacement (this factor was derived from a utility-scale finance model by the DOE (George & Schweitzer, 2006)).

For this analysis, we computed LRC for the control system, yaw system, rotor blades, gearbox, generator and drivetrain components and estimated a reduction in LRC for the proposed system. The reduction in cyclic fatigue loading will extend the meantime between failures for the blades, the generator and the drive train. Navatek recognizes that a key challenge and objective of the research is to develop and demonstrate a robust active flow control system that does not increase LRC or reduce system availability. For the purpose of this analysis, we assume that any active flow control system maintenance will coincide with the upkeep of other control system components with no additional downtime and negligible replacement costs. Table 5 shows the baseline and proposed system LRC computed using Equations (10-2) - (10-5).

Table 5. Baseline and proposed levelized replacement costs.

	Representative Categories	Failure rate (per year)	Number of years per failure	Downtime per failure (days)	Downtime lifetime (days)	RC (2012) $K	PV ($K)
Levelized Replacement Cost							
BASELINE	Control	0.42	2	2	20	115	695
	Yaw System	0.18	6	20	67	165	332
	Rotor	0.17	6	41	137	1710	3438
	Gearbox	0.1	10	41	82	1625	2182
	Generator	0.1	10	32	64	405	544
	Drivetrain	0.06	17	32	38	490	382
					Total Baseline LRC = $442K per year		
PROPOSED	Control	0.42	2	2	20	161	974
	Yaw System	0.18	6	20	67	231	464
	Rotor	0.1	10	41	82	2023	2716
	Gearbox	0.05	20	41	41	2275	1696
	Generator	0.05	20	32	32	567	423
	Drivetrain	0.048	21	32	30	686	0.00
					Total Proposed LRC = $366K per year		

10.5   Operations and Maintenance

Operations and Maintenance Cost (O&M) is a significant component of annual operating expenses for offshore systems. Because O&M is tax deductible, the final O&M costs are reduced by 40% (an estimated combined federal-state tax rate). Operations and Maintenance costs were also provided in the BVG report, estimated to total $65 per kW per year for the baseline system. Total O&M costs per kW are assumed to be equivalent for the baseline and proposed wind farms.

10.6   Annual Energy Production

Annual Energy Production (AEP) is calculated using the methodology described in the International Electrotechnical Commission (IEC) Standard 61400-12-1. The wind speed range is divided into 0.5 m/s bins from 0 to 30 m/s. Since we don't have actual wind survey data, we used the following generic formula:

$$AEP_{tot} = N_h \sum_{i=1}^{N} \left\{ (F(V_i) - F(V_{i-1})) \frac{P_i + P_{i-1}}{2} \right\}$$
(10-6)

where N_h is the number of hours in a year (N_h=8760), N is the number of wind speed bins, V_i is the wind speed in the ith bin (in m/s), P_i is the power output in the ith bin (in kW) and $F(V)$ is the Rayleigh cumulative probability distribution function for wind speed, defined as follows:

$$F = 1 - e^{-\frac{\pi}{4}\left(\frac{V}{V_h}\right)^2} \qquad (10\text{-}7)$$

where V_h is the wind speed at the turbine hub height.

The baseline system is assumed to reach 80% of the Betz limit between cut-in and rated wind speeds, and we assume that the advanced control algorithms will permit C_P to reach 90% of the Betz limit in that region of the power curve for the proposed system. Also, because the hub is higher for the proposed system, the velocity at the hub is assumed to increase by about 5% from 10 m/s to 10.5 m/s. The resulting power curves are shown in Figure 80.

The net annual energy production, accounting for availability and energy losses, is then computed from

$$AEP_{net} = AEP_{tot}(1 - EL) * Availability \qquad (10\text{-}8)$$

where *EL* is the product of individual losses, L_i:

$$EL = 1 - \prod_i (1 - L_i) . \qquad (10\text{-}9)$$

The availability is the fraction of the total number of hours (8760) for which the system is operational. The Table 6 shows the individual losses and availability for the baseline and proposed wind farms.

AEPnet is further reduced for the proposed system by the power absorbed by the flow control system. We estimate that the power consumption is 20 W per meter of actuator. Each blade is assumed to have four actuators spanning the entire blade and each actuator is on for 75% of the time the turbine is operational. With these assumptions, the plasma flow control system consumes about 0.4% of the net energy produced per year.

Plasma Flow Control for Wind Turbines – Final Report   Navatek, Ltd.

NAVATEK TR--2013/2
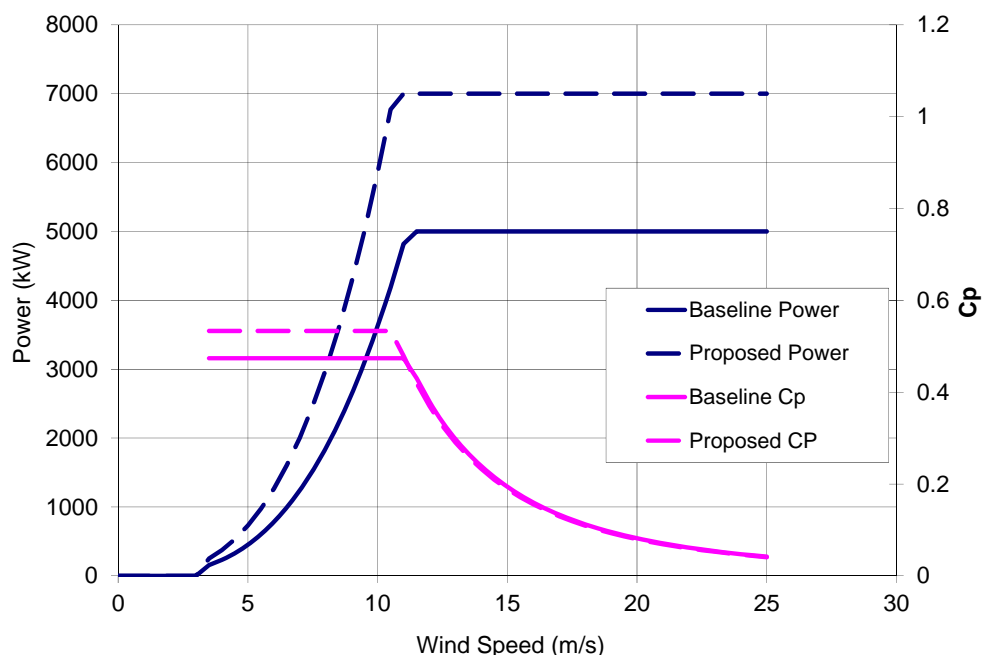
Figure 80. Baseline and proposed power and Cp curves. *This plot shows power (left axis) and CP (right axis) for the baseline system and the proposed system. The increase in in power and CP results for an assumed increase in capture efficiency and an increase in turbine radius.*

Table 6. Baseline and proposed energy losses and availability.

Energy Losses and Availability			
	Baseline	**Proposed**	**Description**
$L_{soiling}=$	0.010	0.005	Blade soiling losses
$L_{control}=$	0.010	0.010	Controls and miscellaneous losses
$L_{DT}=$	0.015	0.010	Drivetrain Mechanical Losses
$L_{PE}=$	0.020	0.010	Drivetrain Electrical System Losses
$L_{collect}=$	0.015	0.015	Collection system losses from the turbines to the substation
$L_{trans}=$	0.015	0.015	Collection system losses from substation to grid
$L_{wake}=$	0.100	0.100	Wake losses
$L_{other}=$	0.020	0.020	Other losses specifically defined
Availability=	0.95	0.97	Annual hours system is capable of operating / 8760 hours
EL=	0.190	0.174	See Equation (10-9)
AEPnet=	19138391	30315130	kWhr/yr/turbine (Equation 10-8)

10.7   COE Model Results

The results of the analysis show a total projected CoE reduction of 18% relative to the baseline system. Table 7 summarizes the results, and Figure 81 shows a breakdown of the projected COE reduction. Most of the projected COE reduction is associated with the increase in rotor diameter, which we assume will be enabled by the mitigation of cyclic loading and the more efficient structural design afforded by the active flow control system.

Table 7. Summary of baseline vs. proposed wind farms.

Representative Categories	Baseline System	Proposed System
Total Installed Capacity (MW)	500	700
AEP_{TOT} (GWh/y)	2,488	3,797
EL (total losses %)	0.19	0.17
Availability (%)	0.95	0.97
AEP_{NET} (GWh/y)	1,914	3,032
Capacity Factor[2]:	0.44	0.49
Cost of Energy ($/kWhr)	0.074	0.061
COE REDUCTION =18.0%		

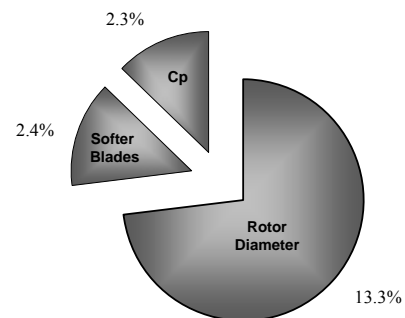| Contributing Change	COE Reduction
Larger Rotor diameter & hub height, offset by increased ICC	13.3
Increased low-wind C_P	2.3
Softer blades, (lower LRC, increased availability and reduced losses)	2.4

Figure 81. Breakdown of COE reduction. *The data on the left, which is plotted in pie-chart form on the right, shows the breakdown of COE reduction by the three contributing factors.*

---

[2] Capacity Factor $= AEP_{NET}/$(Rated Power *8760 hours)

11.   Conclusions and Recommendations

In this project, we began the three-phase development of a plasma flow control system for wind turbines. We developed laboratory facilities for component development and testing, simulation tools to aid in design and performance predictions, and a wind turbine test bed for field demonstrations. We quantified the production of unwanted gaseous byproducts produced by plasma actuators, and we developed a financial model to study levelized cost of wind energy. The project culminated with a field demonstration of a manually controlled plasma flow control system on a 20 kW wind turbine in Honolulu, HI. The most important accomplishments of this Phase I project centered on the establishment of tools – both computational and experimental – that will allow us to systematically develop and demonstrate the plasma flow control technology.

Although we made great progress toward our goal of demonstrating a plasma flow control system for wind turbines during this twelve-month effort, much remains to be done in advancing the technology.   We recommend that the next Phase of development be focused on the demonstration of a plasma flow control system with feedback control. We also recommend that future systems incorporate a pulsed power supply to reduce power consumption. The power consumption should also be quantified accurately so that the net gain in power generation can be determined.

The simulation toolset should be expanded to include FINE™ Turbo and that tool should be used to study the physics of flows with actuation. The ability of plasma flow control to perform circulation control and to react to unsteady gusts should be evaluated numerically and through systematic wind tunnel experiments.

12.　　Contract Cost Summary

Per Contract Amendment P0002, this project was operated under a cost-sharing contract. A top-level breakdown of the final Government-funded costs, by major cost category, are provided in Table 8.

Table 8. Final contract cost breakdown by major cost category.

Cost Category	Amount
Labor	$ 529,032.17
Subcontract	$ 50,715.84
Materials	$ 73,029.04
Travel	$ 15,950.05
Other Direct Costs	$ 46,978.90
Total Costs	**$ 715,706.00**

Acknowledgements

Plasma Flow Control for Wind Turbines – Final Report   Navatek, Ltd.

NAVATEK TR--2013/2

References

Ashwill, T. D. (2005). *Developments in Large Blades for Low Cost Wind Turbines.* Sandia.

Associates, B. (2010). *A Guide to an Offshore Wind Farm.* The Crown Estate.

Corke, T. C., Enloe, C. L., & Wilkinson, S. P. (2010). Dielectric Barrier Discharge Plasma Actuators for Flow Control. *Annual Review of Fluid Mechanics*, 505-529.

Drela, M. (1989). XFOIL: An Analysis and Design System for Low Reynolds Number Airfoils. In *Low Reynolds Number Aerodynamics.* Springer Verlag.

Energy, G. W. (2006). *Advanced Wind Turbine Program Next Generation Turbine Development Project.* NREL.

Enloe, C. L., McLaughlin, T. E., VanDyken, R. D., Kachner, K. D., Jumper, E. J., Corke, T. C., et al. (2004). Mechanisms and Responses of a Single Dielectric Barrier Plasma Actuator: Plasma Morphology. *AIAA Journal, 42*(3), 589-594.

Enloe, C., McLaughlin, T. E., VanDyken, R. D., Kachner, K. D., Jumper, E. J., Corke, T. C., et al. (2004). Mechanisms and Responses of a Single Dielectric Barrier Plasma Actuator: Geometric Effects. *AIAA Journal, 42*(3), 595-604.

EPA. (2013). *Air and Radiation*. Retrieved May 30, 2013, from US Environmental Protection Agency: http://www.epa.gov/air/criteria.html

Fine, N. E. (2010). Plasma Catalysis for Enhanced-Thrust Single Dielectric Barrier Discharge Plasma Actuators. *AIAA Journal, 48*(12), 2979-2982.

Fine, N. E., & Brickner, S. J. (2010). Plasma Catalysis for Enhanced-Thrust Single Dielectric Barrier Discharge Plasma Actuators. *AIAA Journal, 48*(12), 2979-2982.

G. Johl, M. P. (2004). Design methodology and performance of an indraft wind tunnel. *The Aeronautical Journal*, 465-473.

George, K., & Schweitzer, T. (2006). *Primer: The DOE Wind Energy Program's Approach to Calculating Cost of Energy.* NREL.

Glauert, H. (1935). Airplane Propellers. In F. Durand, *Aerodynamic Theory* (pp. 169-360). Berlin: Springer.

IEC. (2005). *Wind Turbines, Part 12-1: Power Performance Measurements of Electricity Producing Wind Turbines.*

Mehta, R. a. (1979). Technical Notes Design rules for small low speed wind tunnels. *The Aeronautical Journal of the Royal Aeronautical Society*, 443-449.

Post, M. (2004). *Plasma Actuators for Separation Control on Stationary and Oscillating Airfoils.* Notre Dame University Ph.D Thesis.

Rasplicka, D. (2008). *Ozone Levels and Their Effects*. Retrieved 12 2008, from Ozone Lab:
    http://www.ozonelab.com/articles/007.htm

Appendix A: Wind Tunnel Development

This appendix describes the design and construction of the low-speed wind tunnel built to test
plasma actuator components and control software.

A.1   Design Overview

The testbed facility consists of an open circuit wind tunnel powered by a centrifugal blower at
the inlet side. It is located in Navatek's 2500 square foot warehouse at 376 Dry Bridge Road in
North Kingstown, RI. Design of this wind tunnel followed the guidelines detailed in *Design
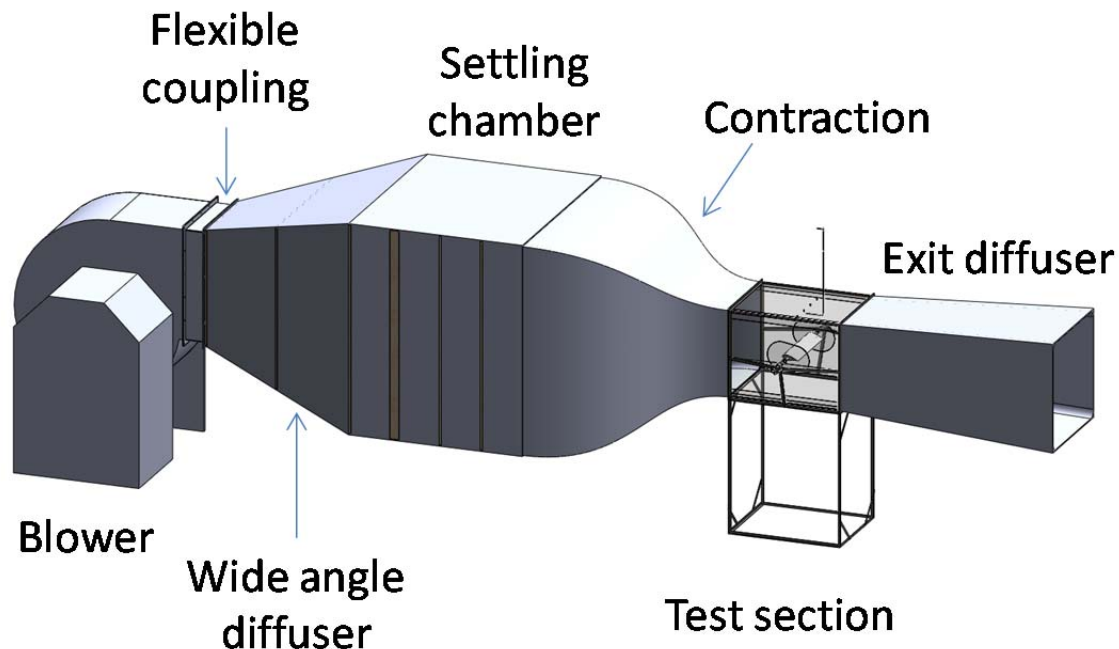rules for small low speed wind tunnels* (Mehta, 1979). A 3D model of the tunnel is shown in
Figure 82.

Figure 82. 3D model of Navatek's open circuit wind tunnel.
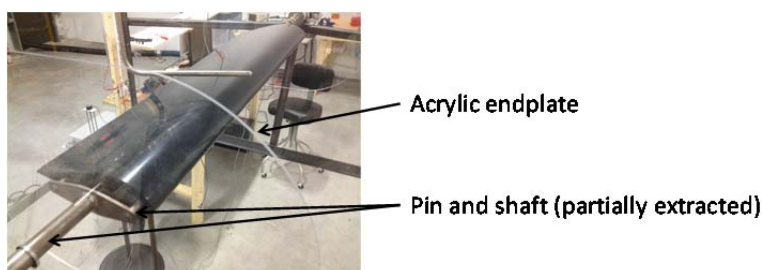
A.2   Test Section

The target test-section speed for this wind tunnel is 50 ft/s (15.2 m/s). The cross sectional area of
the test section, along with the design speed, drives the design of the wind tunnel. The most
important constraint for this tunnel is the length of the laboratory (roughly 57 ft) which will limit
the cross sectional area of the test section for a given contraction ratio and for expansion angles
of the wide angle and exit diffusers that fit within the guidelines. Using a spreadsheet model and
iterating to stay within recommended design guidelines, a 9 ft^2 cross section was chosen. While a

circular cross section is optimal for flow, rectangular cross sections are very common in wind tunnels due of their lower cost of construction. For that reason, a square cross section 3 ft x 3 ft was chosen. Fillets were added in the corners to mitigate the risk of flow separation in these areas. The fillets are made of foam and painted with a Dura coat finish. The test section is four feet in length, steel framed with acrylic roof and floor and sides made of scratch-resistant Lexan (Figure 83). The floor is mounted on hinges to give access to the test section for mounting of test wings or other models.
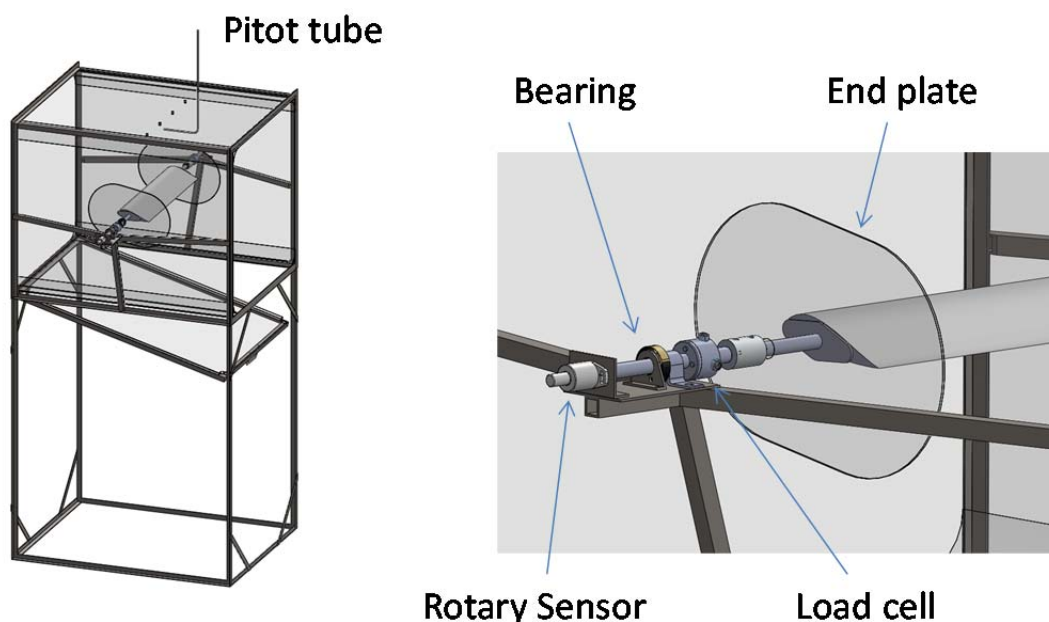

Figure 83. 3D model of the tunnel test section. *This graphic shows the tunnel test section (left) with an expanded view of the right side shelf housing the shaft bearing, load cell and rotary sensor for measuring the angle of attack (right).*

Models are mounted on a steel shaft, oriented horizontally between the left and right sides of the test section. The steel shaft, shown in Figure 84, is welded to an endplate with a pair of pins. The pins, which are 0.375 inches in diameter with a length of 0.875 inches, fit into holes drilled into the side of the wing. Lift and drag are measured using a pair of strain gauges (Futek MBA400 Bi-Axial Load Arm: 50lb capacity) mounted on the shaft that holds the model. The angle of attack is measured with the help of a Positek P500-30-AJ rotary sensor. The shaft pieces were built by a local machinist (The Droitcour Company in Warwick, RI).

Figure 84. Test wing mounted in the test section. *This picture shows the test wing with shaft and pins partially extracted. The acrylic endplate and the steel shaft endplate mount flush to the edge of the wing when the pins are fully inserted.*

The roof of the test section has five equally-spaced holes to fit a Pitot tube (Dweyer 160-36: Stainless steel Pitot tube, 5/16" dia., 36-5/8" insertion length) and differential pressure transducer (Omega PX653-02D5V) for measuring velocity. The Pitot tube can be mounted on a linear actuator (also used for our hot-wire foam cutter) for performing vertical velocity sweeps (see Figure 85).
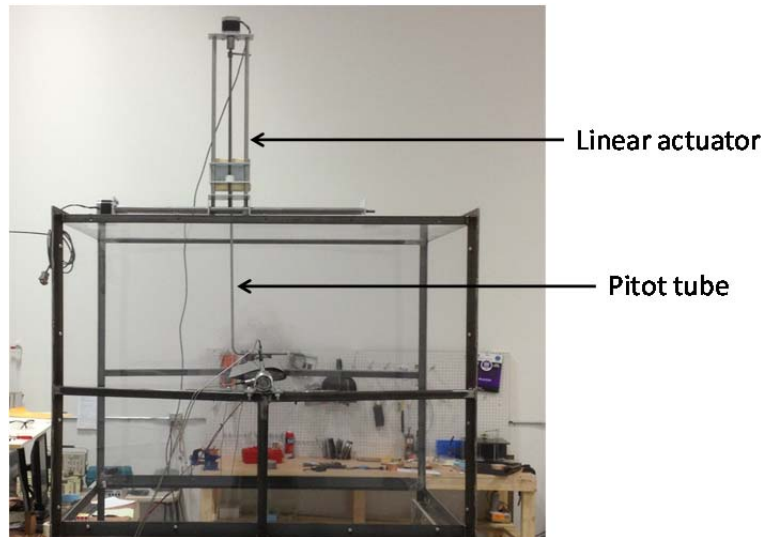
Figure 85. Pitot tube and mounting apparatus. *This picture shows the Pitot tube mounted on a linear actuator for performing vertical velocity sweeps.*

A.3 Exit Diffuser

The exit diffuser is fitted directly downstream of the test section and serves to reduce unsteady flow and decrease pressure losses at the exit. Its expansion should not exceed 5° for best flow steadiness even though the best pressure recovery occurs at higher angles. The outlet-to-inlet area ratio should not exceed about 2.5.

A very efficient exit diffuser would be prohibitively long for our constrained space. For that reason, a less-than-optimal 6° expansion was selected, with an area ratio of 1.6. With these parameters, the length of the exit diffuser is 7.6 ft.

A.4 Contraction

The contraction just upstream of the test section serves to increase the mean velocity and reduce the boundary layer thickness at the walls, while allowing the flow conditioning screens and honeycomb to be placed in a low speed region where there will be less pressure loss. It also reduces the velocity variations to a smaller percentage of the average. The two important parameters are contraction ratio and length.

Contraction ratios between 6 and 9 are typical of small tunnels. A small ratio of 6 was chosen to minimize the noise and likelihood of separation near the ends and also to reduce the size and cost of the settling chamber. This comes at the expense of greater pressure losses in the settling chamber, which can be overcome with a more powerful blower.

The contraction wall shape must be smooth, especially at the ends, but its exact shape is often 'designed by eye'. In general, the radius of curvature is lower at the exit. A cubic spline tangent at both ends to the settling chamber and test section walls was chosen. This satisfies the rule of thumb that at least the second derivative of the curve should be zero at the ends. The inflection point was placed at a longitudinal position beyond the section's midpoint at a distance from its inlet equal to 60% of the length of the section. The length of the contraction section is about 6.5 feet (see Figure 86).
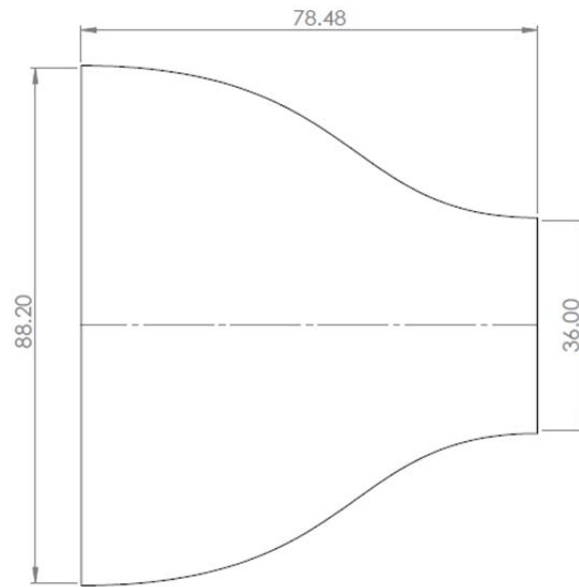
Figure 86. Contraction section shape design.

A.5   Settling Chamber

The settling chamber, shown in Figure 87, is used to house a honeycomb and screens for flow conditioning before the contraction. Its cross sectional area is determined by the contraction ratio and its length by the spacing necessary between screens for them to perform successfully. This tunnel uses a typical arrangement consisting of a screen at the inlet, a honeycomb, and two more screens downstream of the honeycomb. The recommended distance between screens and after the last screen of 0.2 diameters was applied. With a 4" honeycomb, the settling chamber length was chosen to be about 6.5 ft.

Screens and honeycomb are removable to allow for cleaning as dust can easily accumulate and disrupt the flow. The screens and honeycomb are mounted on wooden frames that slide into slots open on one side of the settling chamber.
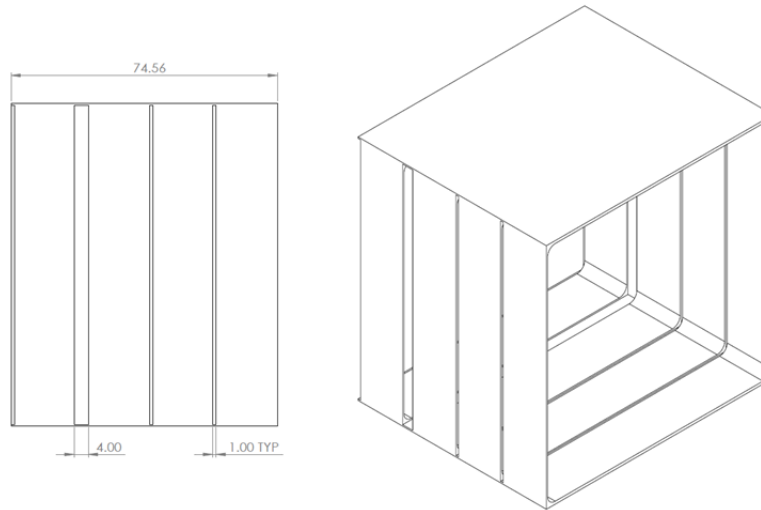
Figure 87. Settling chamber design.

A.6   Honeycomb

A honeycomb is necessary to remove swirl, lateral turbulence, and lateral mean velocity variations in the flow. While paper honeycombs can be adequate for small tunnels, aluminum was chosen for this design. The design guidelines state that the cell diameter should be such that there are 150 cells per settling chamber diameter (or about 25,000 cells total) and such that the width of the honeycomb is 6 – 8 times the cell diameter.

Standard honeycomb cell sizes considered were ½" and ¾". For this tunnel, that works out to be about 31,100 or 13,800 total cells respectively. The ½" size was chosen as being closer to the recommendations. The blower is sized to account for the larger pressure drop. The length was chosen to be 8 times the cell diameter or 4 inches. The honeycomb was purchased from Plascore Inc.
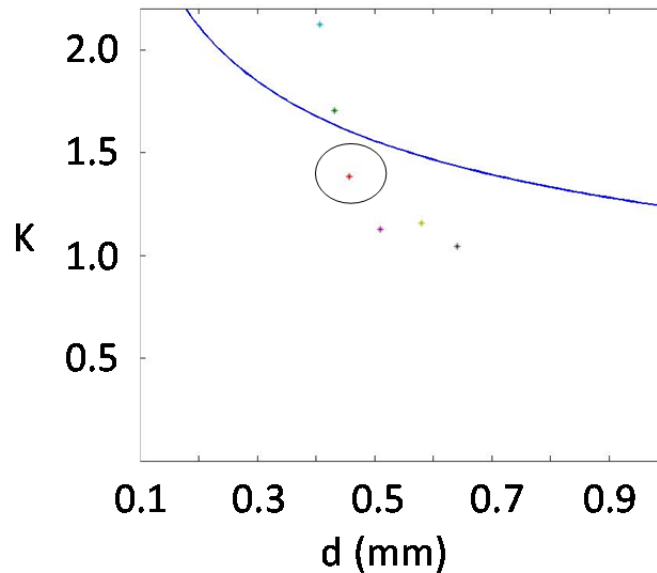
A.7   Screens

Screens impose a static pressure drop proportional to the square of the velocity, chopping up the turbulence and making the velocity profile more uniform. The important parameters are the open area ratio β and the pressure drop coefficient K, where K is approximated by

$$K = 6.5Re^{-1/3}(1-\beta)/\beta^2 \qquad\qquad (A-1)$$

where $= \frac{Ud}{\beta v}$, d being the wire diameter. K does not need to be more than 2 to perform well. In fact, multiple screens with smaller values of K are more effective than a single screen with a higher K. β should be small to give a sufficient K but must larger than 0.57 to avoid instabilities. For a given β, a smaller mesh is better for reducing pre-existing turbulence.

Wire diameters are plotted as a function of K in Figure 88 for the best standard woven wire cloths. The blue line represents β=0.58. A good screen material should be close to but below the β=0.58 line. Smaller wire diameters (towards the left) are also preferable.

Plasma Flow Control for Wind Turbines – Final Report   Navatek, Ltd.

NAVATEK TR--2013/2

Figure 88. Tunnel screen selection plot. *The solid line in this plot is the approximation given by Equation (A-1), and the symbols represent some commercially available wire cloths. The red symbol (circled) represents the wire cloth we selected.*

After researching wire cloths available on the market, we chose a 12-mesh 0.0180" wire diameter woven wire cloth (represented by the red symbol in Figure 88). It has an open area ratio of 0.615 which gives a pressure drop coefficient of 1.33.

A.8   Wide Angle Diffuser

A wide angle diffuser is necessary to expand the cross sectional area from the outlet of the blower to that of the settling chamber. Because the area increases rapidly, screens are required to avoid separation. Design boundaries were established and are shown in Figure 89 and Figure 90.
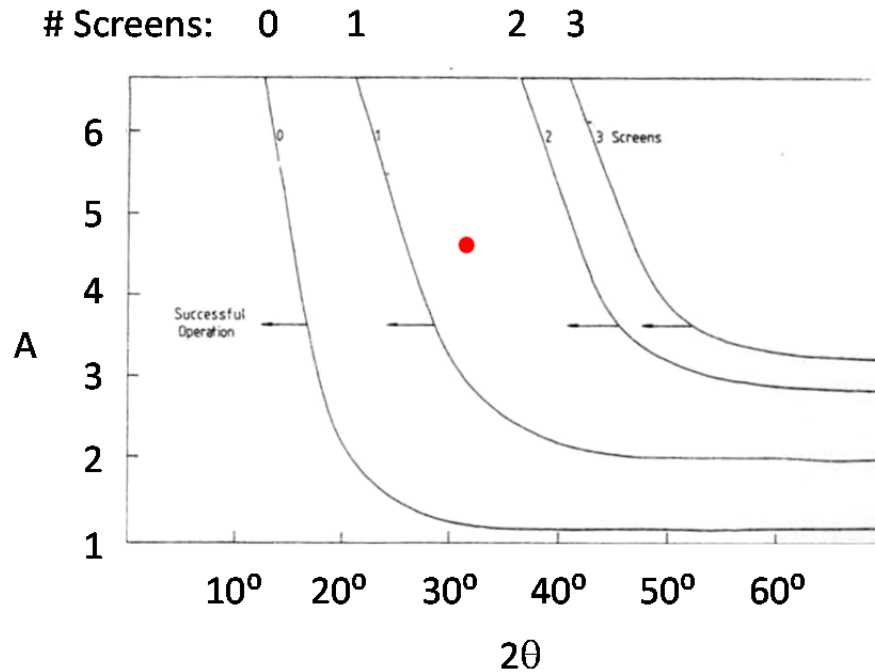
Figure 89. Design boundaries for diffusers with screens: angle. *This plot is used to determine the geometry (angle, length) of the wide angle diffuser, taken from* (**Mehta, 1979**)*.*
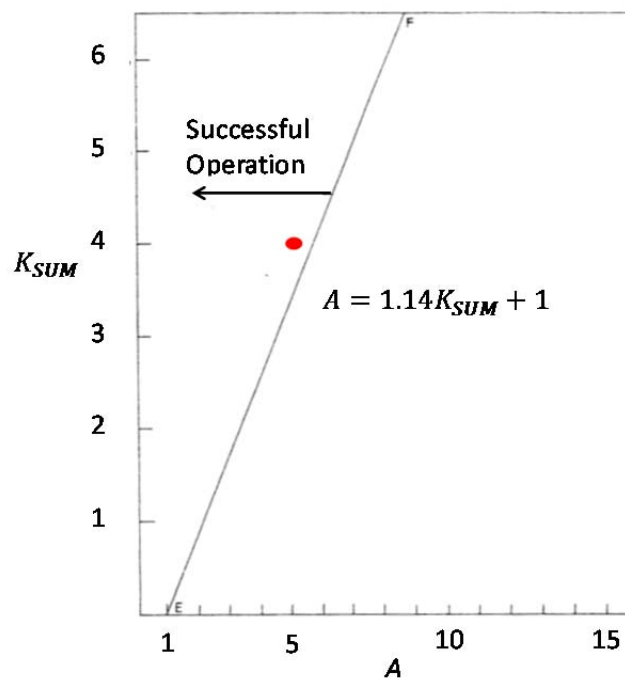
Figure 90. Design boundaries for diffusers with screens: pressure drop. *This plot shows overall pressure drop coefficient requirements for a diffuser with screens, taken from* (**Mehta, 1979**)*.*

The area ratio of the diffuser with the chosen blower is 4.68. An initial estimate of a 6' length and 3 screens (including the one at the inlet to the settling chamber) was chosen. The red dots in the figures above represent this initial estimate. It can be seen in Figure 89 that the pressure drop coefficient for the screen is just high enough for a successful operation.

Screens were placed at the inlet and outlet as the sudden changes in wall angles there makes these locations the most likely for separation. The third screen was placed equidistant between the first two in the middle of the diffuser. Screens are mounted on wooden frames that fit into slots much like the design for the settling chamber.

The diffuser was designed with planar walls for ease of construction and cost considerations, even though curved walls would be more efficient. The inlet has a rectangular cross section and a flange to mate with the outlet of the blower. The cross section transitions to square at the outlet. The interior edges have a variable radius fillet that starts at 0 to match the bower outlet and increases to a 3" at the diffuser outlet.
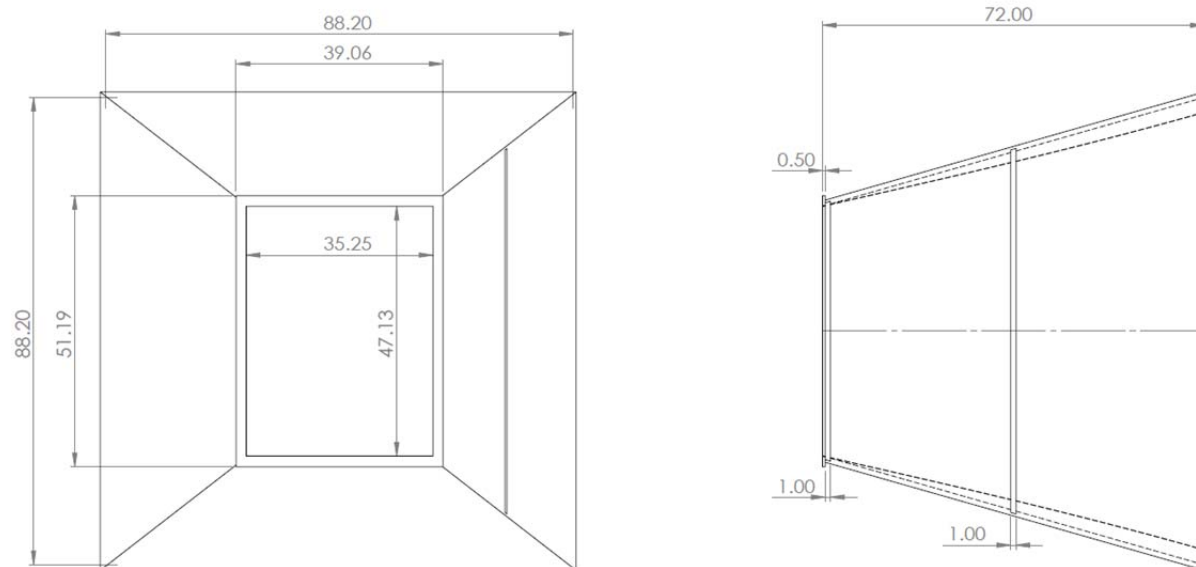

Figure 91. Wide angle diffuser design.

A.9   Blower

Centrifugal blowers (as opposed to axial fans) were considered for this tunnel as they are quieter and more efficient over a wide range of loads (e.g., pressure drops). Inlet blowers are commonly used for open circuit wind tunnels. The main parameters for fan selection are flow rate and static pressure. Blowers were considered that could handle a flow rate of 26,000 ft^3/min at an over-estimated static pressure drop of 3 in wg. Other considerations were cost, efficiency, noise, and outlet area. A larger outlet area will reduce the wide angle diffuser's area ratio and included angle making it easier to meet the design boundaries discussed above. It also reduces the significant pressure drop across the first screen.

Quotes were obtained for five blowers of various sizes. Larger blowers are advantageous for a few reasons. They are more efficient, requiring lower-powered electric motors and thus lower operating costs. They are available with larger outlet flanges and spin at slower speeds which generally equates to less noise. On the other hand, smaller fans have a lower initial cost and take up less space.

A Greenheck model SWB-344-200 fan was chosen. Its operating power is 18.2 hp and is paired with a 20hp motor. It operates at 716 RPM and has 80 dBA sound power at the outlet. Compared to the second best option, this unit cost about 6% more and is 26% larger, but it uses 30% less power, has a 59% larger outlet area, and is significantly quieter.


Figure 92. Greenheck series 200 centrifugal fan.

The height of the outlet on the blower determines the height of the centerline for the tunnel. With this blower, the center of the test section is 6.25 ft off the ground. A coarse-mesh wire screen (sold as a fencing material) was placed over the inlet to prevent accidental ingestion of loose items (see Figure 93). The blower is controlled using a variable frequency drive (VFD, Danfoss FC-102P15T2), shown in Figure 94.

Plasma Flow Control for Wind Turbines – Final Report   Navatek, Ltd.

NAVATEK TR--2013/2

Figure 93. **Blower inlet**. *This picture shows the addition of fencing to prevent ingestion of loose items.*
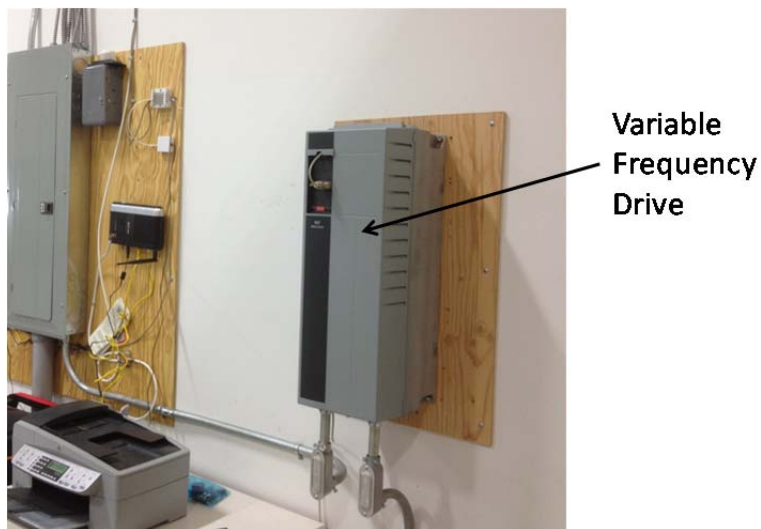
Figure 94. Variable frequency drive. *This picture shows the variable frequency drive which controls the wind tunnel velocity.*

A.10   Room Positioning

The warehouse is 57 feet in length and 32 feet wide (see Figure 95). The longitudinal centerline of the tunnel is aligned with the centerline of the room, which is offset from the centerline of the overhead door by about 2 feet. Although slightly higher speeds can be obtained with the overhead door open, we will run the tunnel with the door closed to eliminate the variable pressure loss at the exit from outside wind conditions.
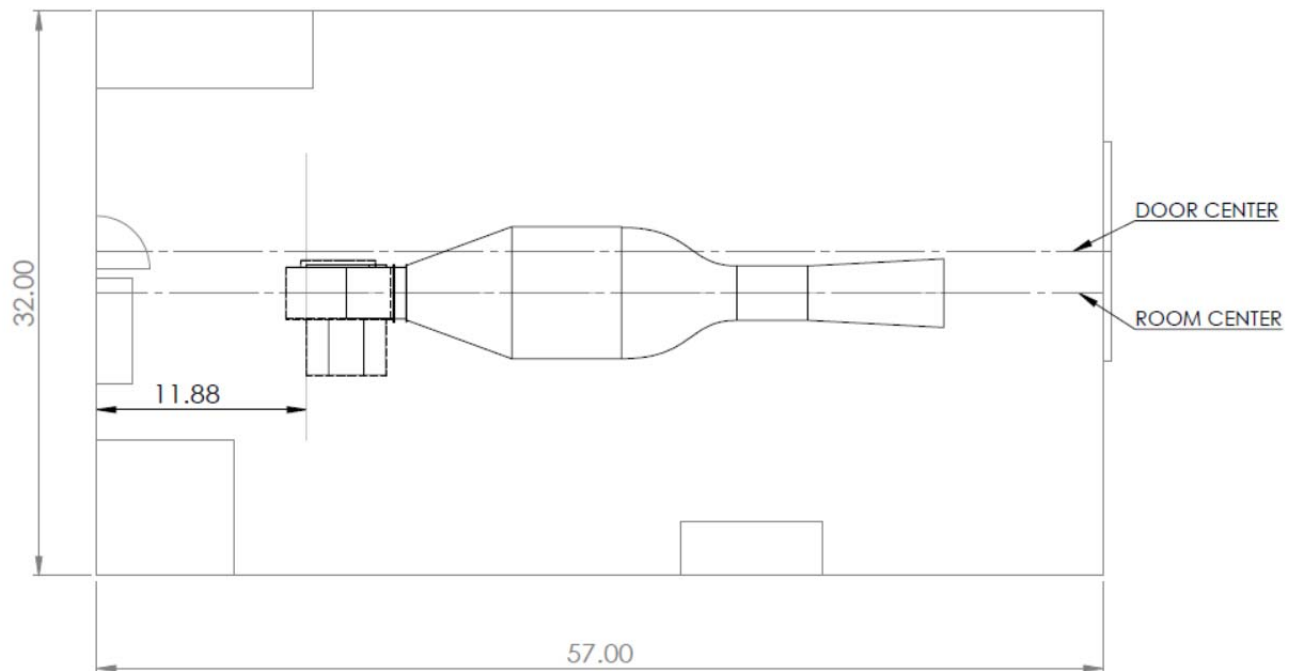
Figure 95. Warehouse layout, with the wind tunnel.

A.11   Materials and Finish

Construction materials considered for the bulk of the wind tunnel (everything except the test section) include fiberglass and plywood. Wood is the less expensive option as the majority of the tunnel consists of straight panels. The main difficulty with using wood is making the curved walls of the contraction. Even for the contraction, forming plywood was found to be one third the cost of fiberglass for a similarly sized tunnel (G. Johl, 2004). We requested construction bids from three local vendors: two high-end carpentry businesses (Carpentry Works, Unlimited in Exeter, RI, and Zuerner Design in North Kingstown, RI) and one boat builder (New England Boatworks in Portsmouth, RI). New England Boatworks (NEB) was the only builder that would meet our schedule and cost constraints. NEB built the tunnel using light composite panels called Decolite, which has a foam core and a thin balsa skin. The interior joints are taped and all interior surfaces are sanded to 200 grit and covered with an enamel coating. The exterior is glassed, sanded and painted with Duracoat paint. The wide angle diffuser, settling chamber and contraction were joined and delivered on a permanent cradle as a single piece, flanged at either end to mate with the flexible coupling at the blower side and the test section at the other end. The exit diffuser was built as a separate piece with its own cradle, flanged on the inlet side to meet with the downstream end of the test section.

The test section consists of a welded steel frame with acrylic roof and floor and scratch resistant Lexan sides. Most of the steel framing consists of 1-inch right-angle pieces with 0.25 in thickness. The acrylic and Lexan pieces are all 0.5 in thick. A local welder (Champlain Welding in Narragansett, RI) built the frame and a local plastics supplier (Sabic Polymershapes, North Kingstown, RI) provided the acrylic and Lexan.

A.12   Data Acquisition

All data acquisition is accomplished using National Instruments control and DAQ cards and chassis (NI 9237 4-Channel, ±25 mV/V, 24-Bit Simultaneous Bridge Module for force balances, NI 9215 4-Channel, 100 kS/s/ch, 16-bit, ±10 V Analog Input Module for pressure and rotary position transducers). The company purchased an additional license to LabView, and a desktop computer to run all instrument control and data acquisition software. All data acquisition equipment is housed on a 5-foot console located adjacent to the test section, as shown in the bottom of Figure 97.

A.13   Tunnel Installation

NEB delivered the wind tunnel in two pieces on May 30, 2012. The wide angle diffuser, settling chamber and contraction were constructed as a single unit, with a flange between the settling chamber and the contraction, and flanges at the inlet and outlet. The second piece was the exit diffuser. Figure 96 shows the tunnel as it arrived at our facility from NEB.

Both sections have built-in cradles made of plywood with 2x4 and 2x6 wood stiffeners. Reinforced slots are built in at the base of the cradles to facilitate lifting with fork-lifts. The total weight of the two sections is just over 1000 lbs.

Soon after delivery, we noticed that the wide angle diffuser, settling chamber, and contraction were improperly seated on the cradle. The rectangular inlet, which needs to have its long axis aligned vertically in order to mate with the blower outlet, was rotated 90-degrees with its long axis aligned horizontally. Also, the slots for the screens and honeycomb were on the top of the tunnel, rather than the side. To fix the problem, NEB sent four skilled laborers on June 4, 2012, to rotate the tunnel on its cradle. The tunnel was lifted using cleats attached to the inlet and outlet and chain falls attached to two structural I-beams on the ceiling of the lab. After detaching the cradle, the tunnel was rotated 90 degrees and re-attached to the cradle. The entire operation took about four hours. Figure 97 shows the tunnel following final installation.

Figure 96. Tunnel as it arrives from NEB at our RI facility.

Figure 97. Pictures of the tunnel following final installation.

This page intentionally left blank.